

論文 / 著書情報
Article / Book Information

題目(和文)	非相反移相効果を用いた導波路型光アイソレータに関する研究
Title(English)	Study of waveguide magneto-optical isolator employing nonreciprocal phase shift
著者(和文)	庄司雄哉
Author(English)	Yuya Shoji
出典(和文)	学位:博士(工学), 学位授与機関:東京工業大学, 報告番号:甲第7194号, 授与年月日:2008年3月26日, 学位の種別:課程博士, 審査員:水本 哲弥
Citation(English)	Degree:Doctor of Engineering, Conferring organization: Tokyo Institute of Technology, Report number:甲第7194号, Conferred date:2008/3/26, Degree Type:Course doctor, Examiner:
学位種別(和文)	博士論文
Type(English)	Doctoral Thesis

Study of Waveguide Magneto-Optical Isolator Employing Nonreciprocal Phase Shift

by

YUYA SHOJI

Department of Electrical and Electronic Engineering
Graduate School of Science and Engineering
Tokyo Institute of Technology

Doctorial Dissertation

Supervisor : Professor Tetsuya Mizumoto

February 2008

Tokyo Institute of Technology
2-12-1-S3-11 Ookayama, Meguro-ku, Tokyo 152-8550, JAPAN

Contents

Chapter 1:

Introduction

1.1	Introduction	1
1.2	Optical isolator	2
1.3	Waveguide isolators	5
1.3.1	Faraday rotation type	5
1.3.2	Nonreciprocal phase shift type	7
1.3.3	Nonreciprocal loss shift type	9
1.4	Integration technology	10
1.5	Objective of study and organization of dissertation	13
1.5.1	Objective	13
1.5.2	Organization of the dissertation	15
	References	17

Chapter 2:

Nonreciprocal phase shift for magneto-optical isolator

2.1	Introduction	21
2.2	Theoretical analysis of nonreciprocal phase shift	21
2.2.1	Solving eigenvalue equation with 1-D waveguide model	23
2.2.2	Perturbation theory with 2-D waveguide model	28
2.2.3	Calculation results and comparison	30
2.3	Principle of isolator operation	39
2.4	Summary	41
	References	42

Chapter 3:

Magneto-optical isolator with silicon waveguides fabricated by direct bonding technique

3.1	Introduction	43
3.2	Device structure and design	44
3.3	Fabrication of Si waveguide	51
3.4	Direct bonding between Si and Ce:YIG	58
3.4.1	Surface activated bonding with oxygen plasma treatment	58
3.4.2	Experiment	59

3.5	Characterization	64
3.5.1	Isolator operation	64
3.5.2	Insertion loss	70
3.5.3	Temperature dependence	70
3.6	Discussion	72
3.7	Summary	76
	References	77

Chapter 4:

Wideband operation of a magneto-optical isolator using phase adjustment in Mach-Zehnder interferometer

4.1	Introduction	79
4.2	Principle of wideband operation	80
4.3	Calculation results	83
4.3.1	Wideband design of three types of isolator	83
4.3.2	Fabrication tolerance	93
4.3.3	Ultra-wideband design	97
4.4	Fabrication of a wideband isolator	100
4.5	Characterization	104
4.6	Discussion	109
4.7	Summary	110
	References	111

Chapter 5:

Polarization-independent magneto-optical isolator using TM-mode nonreciprocal phase shift

5.1	Introduction	113
5.2	Principle of polarization-independent operation	114
5.3	Device structure	116
5.4	Design of nonreciprocal phase shifter	118
5.5	Design of polarization converter	126
5.5.1	Principle of waveguide polarization converter	126
5.5.2	Calculation results	128
5.6	Discussion	136
5.7	Summary	137
	References	138

Chapter 6: Conclusions	140
Acknowledgement	143
Publication list	145

Chapter 1:

Introduction

1.1 Introduction

The spread of the Internet has led an explosive demand for communication-network systems. New multimedia services such as database queries and updates, music distribution, video streaming, and real-time voice telephone increase the data traffic. Several internet service companies in Japan provide broadband access technologies with digital subscriber lines (DSL), cable television (CATV), and fiber to the home (FTTH). The number of the subscriber is more than 23 million, and especially that of the FTTH is more than 5 million which is increasing rapidly [1]. The optical fiber communication is promising technology for high-capacity network and international backbone systems.

The first breakthrough of optical fiber communication is the invention of the laser in 1960 [2]. Lightwaves from the coherent source can carry enormously large amounts of information compared with radiowaves and microwaves. Also the transmission channel, namely the optical fiber has been the dramatic improvement of low-loss transmission in 1970 by Corning Glass Works in the United States [3]. Now typical loss of optical fibers is in the range of 0.2 dB/km at a wavelength of 1550 nm that is almost the lowest loss predicted theoretically in a silica fiber [4]. The transmission capacity upto 10 Gbit/s are widely installed and 40 Gbit/s systems are ready to be installed in Japan. In the mid-1990s, a use of erbium-doped fiber amplifier (EDFA) and wavelength-division multiplexing (WDM) offers a further boost in fiber transmission capacity to higher levels and to increase the transmission distance. The basis of WDM is to use multiple sources operating at slightly different wavelengths to transmit several independent data streams over the same fiber. This system has high flexibility to provide new network architectures as well as high capacity [5].

Recently, the optical communication systems are attracted to not only a long-haul

transmission but short distance transmissions such as rack-to-rack, board-to-board, and chip-to-chip due to its high capacity. In such systems, integrated optics, which usually denotes an optical waveguide device on transparent substrate such as glass, lithium niobate, or semiconductor, is desired to reduce the cost and size by integrating them high-densely on a single chip. The advance of the integrated optics pioneers a new field of optoelectronics that integrate optical and electronic devices on the same semiconductor platform monolithically.

1.2 Optical isolators

When light travels through a fiber link, some optical power gets reflected at refractive-index discontinuities such as in splices, couplers, and filters, or at air-glass interfaces in connectors. The reflected signals can degrade both transmitter and receiver performance. In high-speed systems, this reflected power causes optical feedback which can induce laser instabilities caused by enhanced effect of carrier vibration [6], mode hopping phenomena among external cavity modes [7], transition to a chaotic state [8], and effect of coherence collapse [9]. These instabilities appear as either intensity noise (output power fluctuations), jitter (pulse distortion), or phase noise in the laser, that can change its wavelength, linewidth, and threshold current. Since they reduce the signal-to-noise ratio, these effects cause power penalties in receiver sensitivities. Multiple reflection points set up an interferometric cavity that feeds power back into the laser cavity, thereby converting phase noise into intensity noise. And the multiple optical paths occurs the appearance of spurious signals arriving at the receiver with variable delays. Unfortunately, these problems are signal-dependent, so that increasing the transmitted or received optical power does not improve the bit-error-rate performance. To eliminate reflections, optical isolators are essentially needed.

Figure 1.1 shows a schematic configuration of an optical transmission system. A distributed-feedback laser diode (DFB-LD), capable of single-mode operation in high-speed modulation owing to its high coherence, must be protected by an optical isolator within the transmitter module [10]. In addition, optical amplifiers such as EDFA enables system designers to remove the bottleneck in electronics in regenerated subsystems, where optical isolators are connected the both sides of the EDF to prevent amplifying noise signals.

Consequently, optical isolators are indispensable to construct high-performance optical fiber link systems.

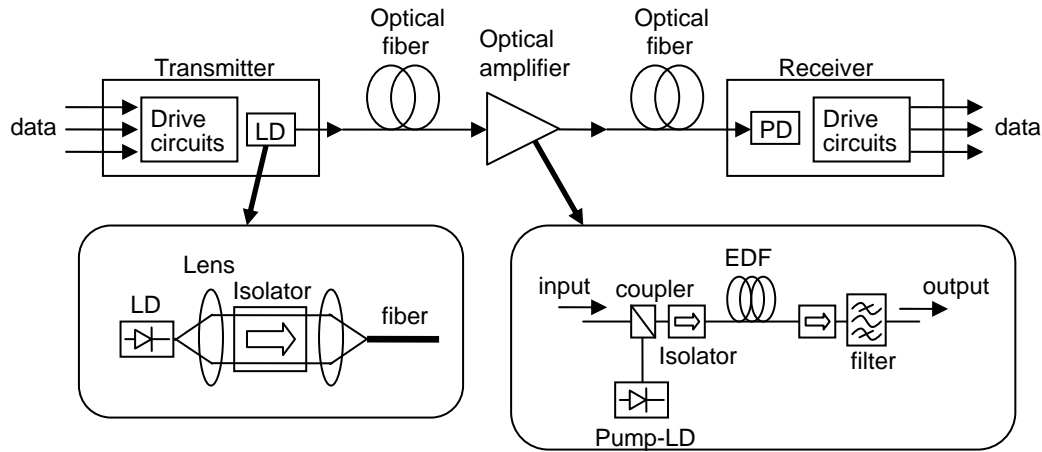


Fig. 1.1 Schematic configuration of optical transmission system.

An optical isolator using magneto-optic effect is so-called magneto-optical isolator. It is typically composed of a magneto-optic garnet such as yttrium iron garnet (YIG) which has magneto-optic effect with small optical absorption in the near-infrared region where optical fiber communication is developed.

Figure 1.2 shows a schematic drawing of a bulk isolator. It is based on the Faraday rotation in a magneto-optic material. A Faraday rotator is set between two polarizers whose transmission polarization planes are angled by 45° to each other. The polarization plane of forward traveling wave passing through the left-hand polarizer is rotated by 45° in the Faraday rotator and pass through the right-hand polarizer. Backward traveling wave which has 45° rotated polarization are selected by the right-hand polarizer. Since the Faraday rotator rotated the polarization by 45° nonreciprocally, backward traveling wave is eliminated by the left-hand polarizer.

Calcite crystals or birefringent materials are used as the polarizer. The Faraday rotation angle is proportional to the Faraday rotation coefficient of the material that determines the total device size. Since a bulk YIG crystal has small Faraday rotation coefficient (~ 200 deg/cm) and requires large external magnetic field, miniaturization of magneto-optical

isolators has been an issue to be solved. Recently, a bismuth-substituted gadolinium iron garnet film such as $(\text{GdBi})_3(\text{FeGaAl})_5\text{O}_{12}$ which is grown by liquid phase epitaxy (LPE) and has large Faraday rotation coefficient (~ 1500 deg/cm) is usually used for bulk isolators [11].

Figure 1.3 shows a configuration of bulk isolator for polarization-independent operation. Birefringent materials are used as polarization splitters, which combine the different polarization waves into the output fiber in the forward direction, while distract them from the input fiber in the backward direction.

These bulk isolators are realized with an extinction ratio between the forward and backward direction, so-called an isolation ratio, more than 35 dB and an insertion loss less than 0.8 dB. In a high-speed transmission system, two isolators are typically cascaded to achieve a high isolation ratio more than 55 dB [12].

At present, commercially available isolators are only bulk types. Unfortunately, the bulk isolators are not suitable for integration because of assembling process of the magneto-optic garnet, polarizers, and lens for focusing the light. The absence of waveguide isolator is a bottleneck for reducing the cost of light source modules and realizing integrated optical circuits. A waveguide isolator is highly desired.

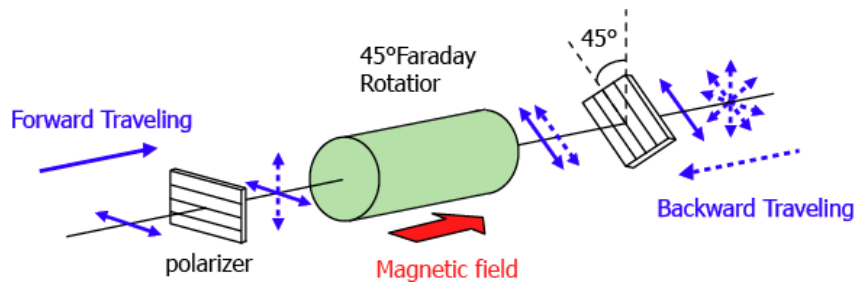


Fig. 1.2 Bulk isolator.

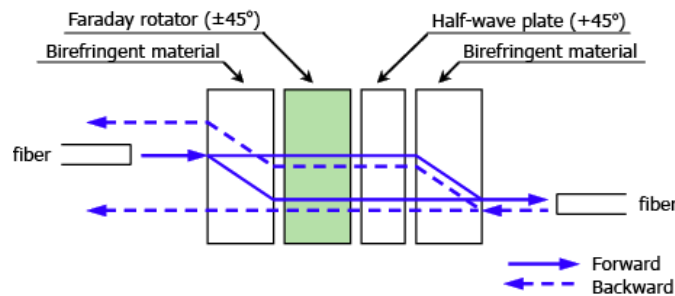


Fig. 1.3 Polarization-independent bulk isolator.

1.3 Waveguide isolators

In this section, several kinds of waveguide isolator that many researchers have investigated are overviewed. The principle of operation and the demonstrated performance are discussed.

1.3.1 Faraday rotation type

Figure 1.4 shows a waveguide isolator based on TE-TM mode conversion. The principle of operation is based on a Faraday rotation used in a bulk isolator. In a planar waveguide, lights propagate as two orthogonal eigenmodes, transverse electric (TE) mode or transverse magnetic (TM) mode. Since it is difficult to construct 45° -rotated polarizer on a planar waveguide, additional 45° reciprocal polarization conversion is installed. Then the total polarization rotation is 0° or 90° depending on the propagation direction. Ando *et al.* demonstrated the waveguide isolator with Cotton-Mouton effect for the reciprocal polarization conversion [13]. This effect is based on a magnetic linear birefringence in a magneto-optic material obtained when its magnetization vector turns to a direction tilted from the film normal in perpendicular to the light propagation as shown in Fig. 1.4. The laser annealing with about 1200 C° at the spot can change the direction of the magnetization that forms the Faraday and Cotton-Mouton regions in a same magneto-optic film plane. The optical isolator was constructed by splitting the converted light with rutile prisms and the isolation ratio of 12.5 dB at $\lambda = 1150\text{ nm}$ was reported.

There is a problem that the difference in phase velocity (phase mismatch) between TE and TM modes determines the upper limit of the polarization conversion. In Ref. [14], a condition of phase matching is carefully analyzed and the fabrication tolerance in an isolator setting is turned out to be very strict.

Another type of the waveguide isolator using the Faraday rotation is a semi-leaky isolator as shown in Fig. 1.5 [15-16]. The isolator is based on the coupling between TE guided and TM radiation modes in a thin-film magneto-optic waveguide and an anisotropic cladding layer. Two kinds of mode coupling occur concurrently. One is a gyrotropic longitudinal mode coupling by the Faraday rotation in the guiding layer, and the other is an anisotropic polar coupling by the birefringence of the cladding layer. These couplings are set so as to be

cancelled in the forward direction but added in the backward direction. Since the waveguide structure is cut-off for the coupled TM modes, therefore called “semi-leaky,” an optical isolation is obtained as the light propagation. Compared with the mode conversion isolator described above, the coupling efficiency of the semi-leaky isolator is insensitive to the phase matching because the coupled radiation modes exist continuously.

This isolator was firstly proposed by Yamamoto *et al.* but it is required to realize a continuous layered-structure of magneto-optic garnet and an anisotropic material without any gap. Recently the isolator was fabricated and demonstrated with an isolation ratio of 20.2 dB at $\lambda = 1550$ nm in our group [17]. A cerium-substituted yttrium iron garnet (Ce:YIG) as the magneto-optic layer and LiNbO_3 as the anisotropic layer were bonded directly by the surface activated bonding (this technique is described more in detail in Chapter. 3).

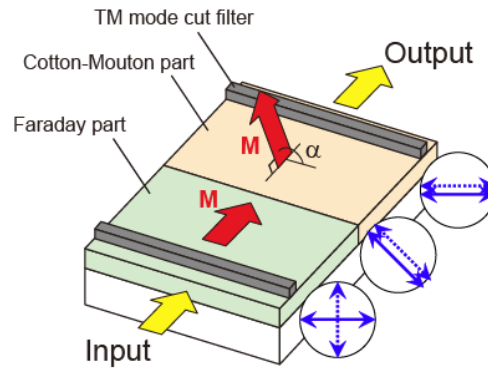


Fig. 1.4 TE-TM mode conversion isolator utilizing Faraday and Cotton-Mouton effect.

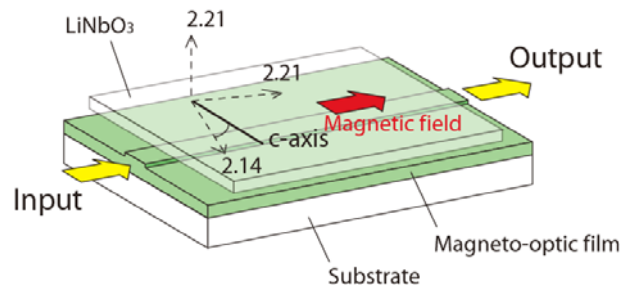


Fig. 1.5 Semi-leaky isolator.

1.3.2 Nonreciprocal phase shift type

Nonreciprocal phase shift is a direction-dependent change of the propagation constant which occurs for one propagation mode propagating in a magneto-optic waveguide when an external magnetic field is applied transversely to the light propagation direction [18]. Since phase matching is not required, this effect is insensitive to the fabrication errors and suitable for a waveguide isolator.

Auracher *et al.* firstly proposed a Mach-Zehnder interferometer (MZI) configuration in which nonreciprocal and reciprocal phase differences between two interferometer arms are induced [19] and many researchers have intensively investigated with this configuration [20-24]. Figure 1.6 shows the schematic diagram of the isolator. By applying external magnetic fields to the two arms in anti-parallel direction, where the nonreciprocal phase shift is yielded with different sign, the nonreciprocal phase difference of $-\pi/2$ or $+\pi/2$ is induced depending on the propagation direction between two interferometer arms. A reciprocal phase difference of $+\pi/2$ given by an optical path difference cancels it in the forward direction but is added to it in the backward direction. Therefore the MZI isolator exhibits constructive and destructive interferences in respective direction.

Fujita *et al.* fabricated this type of isolator with $(\text{Bi,Lu,Nd})_3(\text{Fe,Al})_5\text{O}_{12}$ garnet film, and demonstrated an isolation ration of 19 dB at $\lambda = 1540$ nm [23]. Yokoi *et al.* proposed an improved design of the MZI configuration with different upper cladding layers in two arms to simplify the magnetization, and demonstrated an isolation ratio of 9.9 dB at $\lambda = 1550$ nm [24]. When the magnetization is aligned in the film plane, a nonreciprocal phase shift is induced in TM mode. On the other hand, when the magnetization is aligned vertically to the film plane, it is induced in TE mode. Two research groups have proposed a polarization-independent isolator using TE and TM mode nonreciprocal phase shift in a MZI simultaneously. Zhuromskyy *et al.* used horizontal and vertical domain walls in the magneto-optic guiding layer [25] and Fujita *et al.* used different side cladding layer [26].

The author has also studied about the improvement of the magneto-optical isolator with the MZI configuration in this dissertation. The objective is mentioned in the Section 1.5.

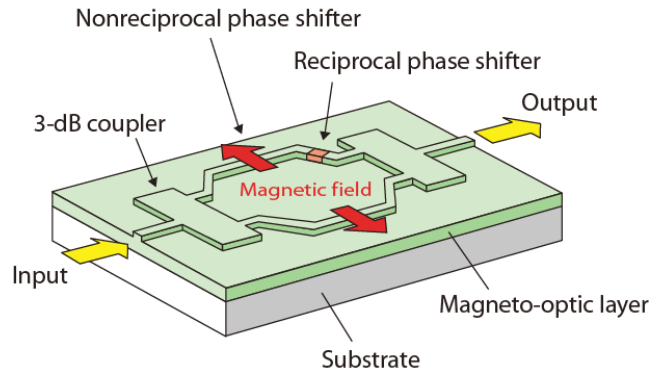


Fig. 1.6 Mach-Zehnder interferometric isolator employing nonreciprocal phase shift.

Shintaku *et al.* proposed and demonstrated another configuration of a waveguide isolator employing nonreciprocal phase shift in conjunction with nonreciprocal guided-radiation mode conversion [27]. Figure 1.7 shows the device structure and the relationship of the propagation constants required for the isolator operation. The directional-dependent propagation constants for TM modes provided by the nonreciprocal phase shift are set to across the propagation constant of the TE radiation mode. Then the TM mode with smaller propagation constant is converted to the TE radiation mode. Applying the external magnetic field with a little component of light propagation direction, the conversion efficiency is enhanced. An isolation ratio of 27 dB at $\lambda = 1535$ nm was reported. A large amount of the nonreciprocal phase shift is required to achieve the design such that one mode is guided but the other is cut-off.

Many other configurations of a waveguide isolator employing nonreciprocal phase shift were proposed by a research group of Osnabrück University. They proposed a nonreciprocal directional coupler [28], a nonreciprocal multi-mode interference isolator [29], a cross strip isolator utilize an nonreciprocal interference between fundamental mode and first-order mode [30], and also a nonreciprocal mode conversion using combination of Faraday rotation and nonreciprocal phase shift [31]. However, since the amount of the nonreciprocal phase shift itself is small, the MZI configuration is the most superior in the device size, fabrication tolerance, and operation bandwidth.

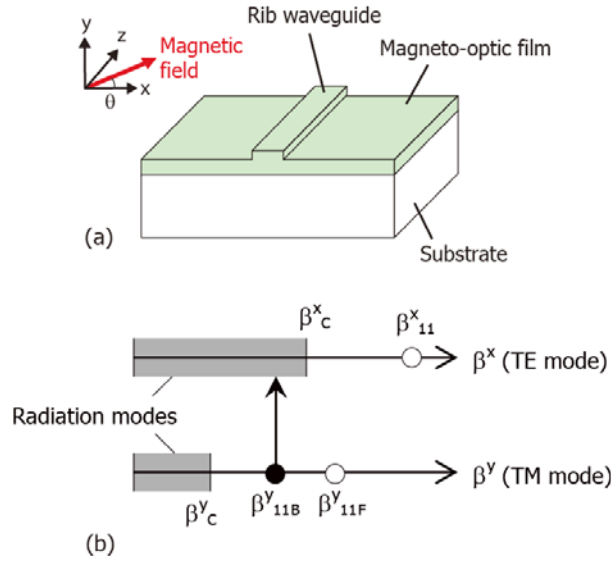


Fig. 1.7 Nonreciprocal mode conversion isolator employing nonreciprocal phase shift. (a) Device structure and (b) relationship of the propagation constants required for the isolator operation.

1.3.3 Nonreciprocal loss shift type

A new concept of waveguide isolator using a magneto-optic effect in a ferromagnetic metal contact was proposed by two research groups. Takenaka *et al.* used InGaAsP active layer grown on InP substrate and Ni or Fe ferromagnetic layer [32], and Zayets *et al.* used GaAsP/AlGaAs-quantum well (QW) active layer grown on GaAs substrate and Co ferromagnetic layer [33]. Figure 1.8 shows the layer structure and the diagram of the complex effective refractive indices in the isolator operation. This waveguide is a semiconductor optical amplifier (SOA) as well as a magneto-optical waveguide. By magnetizing the ferromagnetic metal in a direction transversely to the propagation direction, the magneto-optic Kerr effect induces a nonreciprocal complex index change, that is, the direction-dependent change in the optical absorption loss as well as phase shift. The loss in the forward direction is compensated by the gain of SOA. Consequently, this isolator is transparent in the forward direction and the remaining loss in the backward direction extinguishes the reflected lights.

The position of the ferromagnetic metal and the direction of its magnetization determine the operating polarization. When they are arranged as shown in Fig. 1.8, the nonreciprocal loss shift occurs in TM mode. Whereas, when the metal layer is located on the side of the

waveguide and the magnetization is aligned transversely to the waveguide plane, the nonreciprocal loss shift occurs in TE mode. The isolator operations were demonstrated in TE mode with the isolation ratio of 14.7 dB/mm [34] and in TM mode with that of 9.9 dB/mm [35].

The problem of this isolator is the ASE noise of SOA. Nonetheless, this waveguide isolator is one of the most suitable configurations for integration with a semiconductor laser diode.

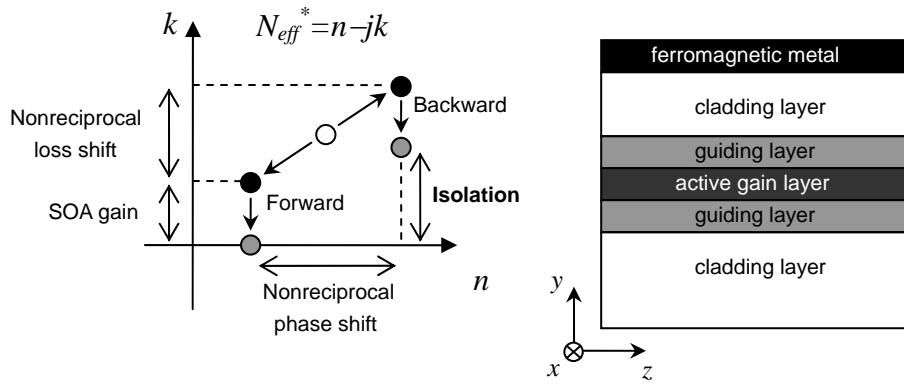


Fig. 1.8 Nonreciprocal loss shift isolator. (a) Operation principle and (b) the device structure.

1.4 Integration technology

These waveguide isolators except the nonreciprocal loss shift type are basically composed of a magneto-optic garnet thin-film waveguide grown on a lattice-matched garnet substrate, such as Bi or Ce substituted rare-earth iron garnet film on a gadolinium gallium garnet (GGG) substrate. It is impossible to deposit the film epitaxially on a semiconductor or a silica substrate. This makes it difficult to integrate a waveguide isolator with other optical devices.

Optical hybrid integration is a promising way of producing a low cost and highly functional optical component. Sugimoto *et al.* demonstrated a hybrid integrated waveguide isolator by assembling a magneto-optic waveguide, thin-film half-wave plate sheet, and thin-film polarizer sheets on a silica-based planar lightwave circuit (PLC) as shown in Fig. 1.9 [36]. They realized a high isolation ratio of 25-34 dB at $\lambda = 1550$ nm, and also a polarization-independent operation by using a MZI configuration [37].

However, the insertion loss of 2.3-3.2 dB is mainly dominated by the reflection loss at the interfaces of each component. In addition, high accuracy of the alignment position is required to achieve the low insertion loss. Hence, it is preferable to configure the monolithically integrated optical isolator.

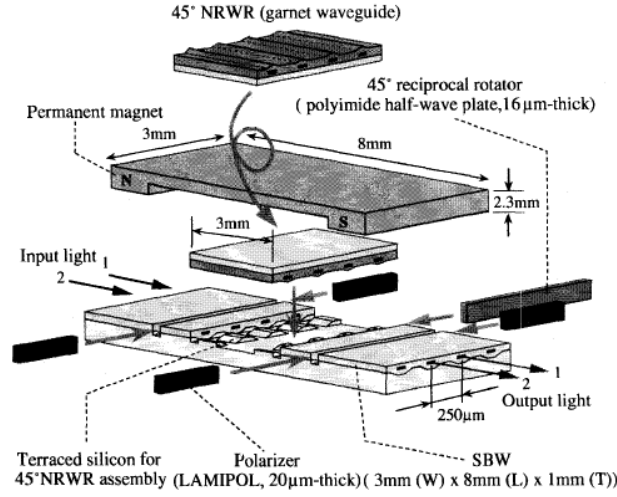


Fig. 1.9 Configuration of hybrid integrated waveguide optical isolator [36].

Debnath *et al.* used a magnetic semiconductor $\text{Cd}_{1-x}\text{Mn}_x\text{Te}$ which can be grown on a GaAs substrate for an integrated isolator [38]. The maximum mode conversion efficiency of $98\% \pm 2\%$ at $\lambda = 735\text{nm}$ was reported. The conversion length of about 1.6 mm, the applied external magnetic field of 5.5 kG, and the optical loss of 0.2 dB/cm led a magneto-optical figure-of-merit of 1000 deg/dB/kG.

Guo *et al.* fabricated a magneto-optical semiconductor by doping Fe into InP or InGaAsP [39]. Magnetic dopants couple to the free carriers in a semiconductor to dramatically enhance the Faraday rotation due to interband transitions. With an appropriate choice of magnetic dopant, the free carrier concentration can be reduced along with free carrier absorption, and it is possible to simultaneously enhance the magneto-optical activity and reduce the optical absorption of a semiconductor. A 45° Faraday rotation with a Verdet coefficient of 23.8 deg/cm/T and the insertion loss of 1.66 dB at $\lambda = 1550\text{ nm}$ were reported.

Although these magnetic semiconductor waveguides are suitable for monolithic integration with semiconductor optical active devices, the magneto-optic effects are still

smaller than that of magneto-optic garnet. Integrating technology by adhesives such as an epoxy and solder is reliable for hybrid integrated devices. However, they cannot be applied to monolithic integration as an intermediate thin layer because of the difficulties in controlling the thickness and its uniformity. A wafer direct bonding technique is one of the promising solutions to overcome this problem.

Wafer direct bonding is a phenomenon that two flat and clean wafers are directly bonded without any adhesives. Yokoi *et al.* proposed a use of direct bonding technique to realize a magneto-optic waveguide with a semiconductor waveguide GaInAsP/InP and a magneto-optic upper cladding layer as shown in Fig. 1.10 [40]. It enables one to realize a semiconductor laser diode monolithically integrated with a magneto-optical isolator by using epitaxial selective area growth technique of semiconductor waveguides [41]. Moreover, it was found that waveguide structure of Si based on a silicon-on-insulator (SOI) substrate with a magneto-optic upper cladding layer has large nonreciprocal phase shift [42,43]. Due to the strong optical confinement in the Si waveguides, the total device size can be miniaturized dramatically. In addition, the field of Si photonic device is the most attractive in the recent years. It is mentioned more in detail in Chapter 3.

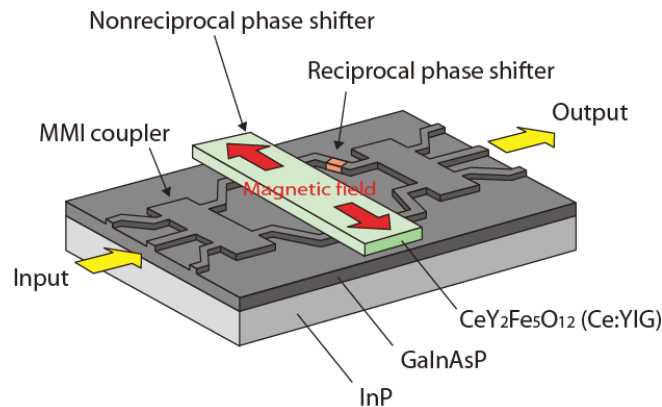


Fig. 1.10 Integrated isolator with semiconductor waveguide.

1.5 Objective of study and organization of dissertation

1.5.1 Objective

Table 1 summarizes the characteristics of the optical isolators mentioned above. The bulk isolator composed of discrete components is not suitable for integration. The fabrication tolerance is large because it is aligned in open space and there is no need of phase matching. However, the fabrication accuracies are required in polishing bulk crystals and collimating them. The device size is about 1 – 2 mm and some lenses are required to collect the lights. The operation bandwidth is about 30 – 40 nm which is dominated by the wavelength dependence of the Faraday rotation of the magneto-optic material. The TE-TM mode conversion types can be composed of either magneto-optic garnet or magnetic semiconductors where strict phase matching condition is required for each case. Using a waveguide polarizer can reduce the device size of the isolator. While semi-leaky isolator has large fabrication tolerance and large operation bandwidth, it is not suitable for integration with other devices because it is composed of a magneto-optic garnet waveguide with a birefringent cladding layer. The isolation ratio increases as the propagation length, for example it is 2.2 mm to obtain an isolation ratio of 30 dB [17]. Nonreciprocal loss shift type is much suitable for integration with semiconductor laser diodes and is relatively easy to fabricate. However, it is not recommended for passive use due to its ASE noise. The isolation ratio increases as the length, e.g. 2.0 mm to obtain an isolation of 30 dB. Nonreciprocal phase shift type especially based on MZI configuration is less sensitive to the fabrication errors and can be integrated with other components by a direct bonding technique. The Si waveguide makes the device size smaller than any other optical isolator ever-reported.

The objectives of this study are the following three about the nonreciprocal phase shift type magneto-optical isolator:

- 1) Fabrication and demonstration of the magneto-optical isolator with Si waveguides

As mentioned above, it has much impact to demonstrate the magneto-optical isolator with Si waveguides for not only integrated optics in long transmission systems but also recent Si photonics. The author investigates the fabrication of the isolator with Si waveguide by direct bonding technique. In this study, a surface activated bonding is employed and examined for

the first demonstration of the isolator operation.

2) Wideband operation of the magneto-optical isolator using phase adjustment

The operation bandwidth of the nonreciprocal phase shift type isolator is as much as that of bulk types. A wideband operation is attractive for WDM application in an optical circuit. Moreover, it becomes the great advantage over bulk isolators. The author proposes a novel design of the wideband isolator and demonstrates the operation. The proposed design is applicable to any kind of structures for the nonreciprocal phase shift type isolator.

3) Polarization-independent magneto-optical isolator using TM-mode nonreciprocal phase shift

The operating polarization is preferred in TE mode because most semiconductor laser diodes operate in TE mode. However, the integrated structure realized by direct bonding has the nonreciprocal phase shift only in TM mode. The author proposes a novel configuration of the polarization-independent waveguide isolator using only TM mode nonreciprocal phase shift and examines the design principle. The isolator is comprised of waveguide polarization converters and nonreciprocal phase shifters. Since the configuration uses only TM mode nonreciprocal phase shift, it is well matched with the integrated structure fabricated by direct bonding.

If these developments are achieved, the magneto-optical isolator employing nonreciprocal phase shift becomes the most promising waveguide isolator to be practically used.

Table 1 Summary of the characteristics of the optical isolators.

Type	Material	Integration	Fabrication tolerance	Device size	Operation bandwidth	Polarization
Bulk	Bi:RIG [*]	×	○	△	△	TE/ independent
TE-TM mode conversion	Bi:RIG ^[13]	△	×	○	△	TE
	CdMnTe/GaAs ^[38] Fe:GaInAsP ^[39]	○	×	△	△	TE
Semi-leaky	LiNbO ₃ /Ce:YIG ^[17]	×	○	△	○	TE
Nonreciprocal loss shift	GaInAsP/InP ^[34,35]	○	○	△	○	TE/TM
Nonreciprocal phase shift (MZI)	Bi:RIG ^[23]	△	○	△	△	TM
	Ce:YIG/GaInAsP/InP ^[40]	○	○	×	△	TM
	Ce:YIG/Si/SiO ₂ ^[42]	○	○	○	△	TM

*RIG: rare-earth (Gd, Lu, Y) iron garnet

1.5.2 Organization of the dissertation

The organization of this dissertation is summarized in Fig. 1.11.

In Chapter 2, the magneto-optical isolator employing nonreciprocal phase shift is described. The nonreciprocal phase shift is numerically examined by 1-dimensional and 2-dimensional simulations. All of the calculations and designs in the following chapter are based on this analysis. The operation principle of the magneto-optical isolator is explained.

In Chapter 3, a magneto-optical isolator with Si waveguides fabricated by a direct bonding technique is described. First, the device is designed with Si waveguides. Second, Si waveguides on a SOI substrate are fabricated and characterized. Third, a surface activated direct bonding is investigated to realize a magneto-optic isolator with a Ce:YIG/Si/SiO₂-layered structure. Finally, fabricated magneto-optical isolator with Si waveguides is characterized.

In Chapter 4, a wideband operation of the magneto-optical isolator is described. First, the principle of the proposed wideband operation is explained. Second, the numerical results of

the wideband design are presented and the fabrication tolerance is examined. Third, a magneto-optical isolator of the wideband design is fabricated with a Ce:YIG rib waveguide, and then characterized.

In Chapter 5, a polarization-independent isolator using TM-mode nonreciprocal phase shift is described. First, the principle of the proposed polarization-independent operation is explained. Next, the numerical results of the polarization-independent design in the nonreciprocal phase shifter are presented. Finally, designs of the waveguide polarization converter are investigated by a finite-element method and a full-vector beam propagation method.

In Chapter 6, the results obtained from this study are summarized.

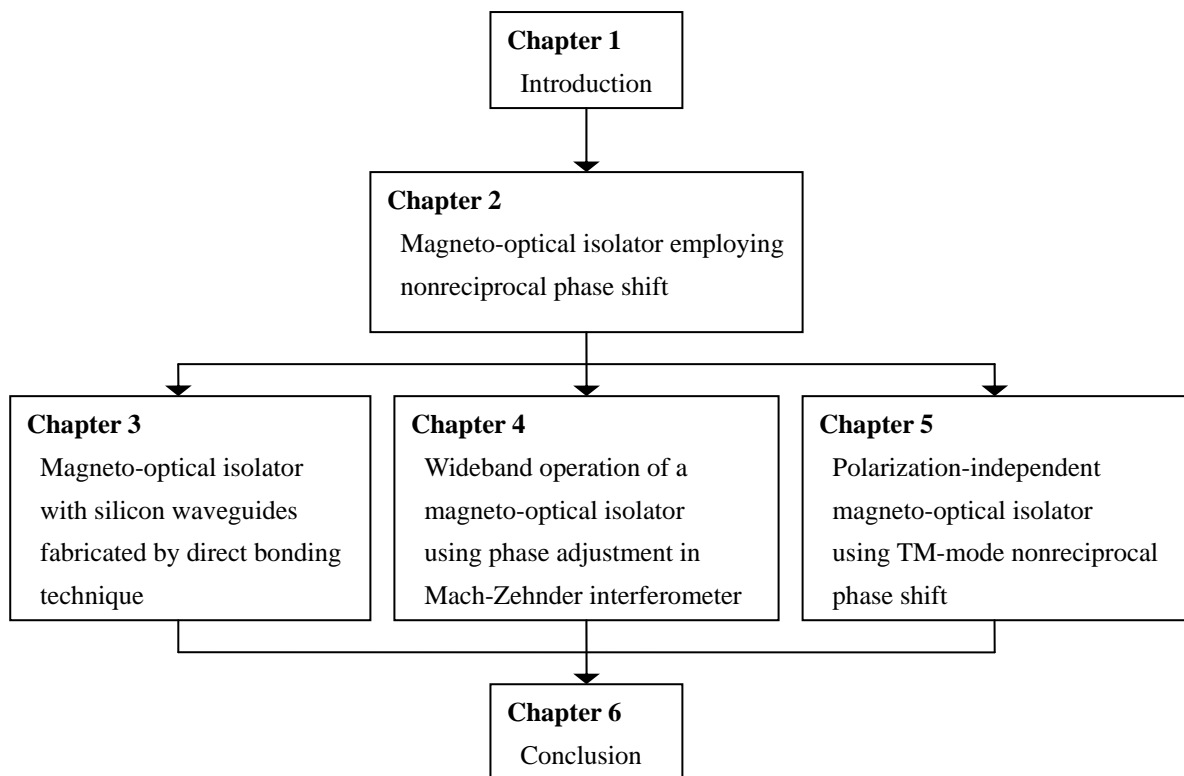


Fig. 1.11 Organization of this dissertation.

References

- [1] Statistical data of Ministry of Internal Affairs and Communications (<http://www.soumu.go.jp/>)
- [2] T. H. Maiman, R. H. Hoskins, I. J. D’Haenens, C. K. Asawa, and V. Evtunov, “Stimulated optical emission in solids,” *Phys. Rev.*, vol. 123, pp.1151-1157 (1961).
- [3] F. P. Kapron, D. B. Keck, and R. D. Maurer, “Radiation losses in glass optical waveguides,” *Appl. Phy. Lett.*, vol. 17, pp.423-425 (1970).
- [4] T. Miya, Y. Terunuma, T. Hosaka, and T. Miyashita, “Ultimate low-loss single mode fiber at 1.55 μm ,” *Electron. Lett.*, vol.15, pp.106-108 (1979).
- [5] M. K. Smit and C. Dam, “PHASAR-based WDM-devices: principles, design and applications,” *IEEE J. Select. Topics Quantum Electron.*, vol.2, pp.236-250 (1996).
- [6] R. Lang and K. Kobayashi, “External optical feedback effects on semiconductor injection properties,” *IEEE J. Quantum Electron.*, vol.16, pp.347-355 (1980).
- [7] H. Fukui, K. Furuya, and Y. Suematsu, “Suppression of mode hopping noise caused by external reflection in dynamic single mode (DSM) lasers,” *Trans. IEICE*, vol.E70, pp.857-864 (1987).
- [8] K. Ikeda and O. Akimoto, “Instability leading to periodic and chaotic self-pulsations in a bistable optical cavity,” *Phys. Rev. Lett.*, vol.48, pp.617-620 (1982).
- [9] D. Lenstra, B. H. Verbeek, and A. J. Boef, “Coherence collapse in single-mode semiconductor lasers due to optical feedback,” *IEEE J. Quantum Electron.*, vol.QE-21, pp.674-679 (1985).
- [10] M. Suhara, S. Islam, M. Yamada, “Criterion of external feedback sensitivity in index-coupled and gain-coupled DFB semiconductor lasers to be free from excess intensity noise,” *IEEE J. Quantum Electron.*, vol.30, pp.3-9 (1994).
- [11] T. Hibiya, T. Ishikawa, and Y. Ohta, “Growth and characterization of 300- μm thick Bi-substituted gadolinium iron garnet films for an optical isolator,” *IEEE Trans. on Magn.*, vol.MAG-22, pp.11-13 (1986).
- [12] Products catalog of TDK Corporation (<http://www.tdk.co.jp/>)
- [13] K. Ando, T. Okoshi, and N. Koshizuka, “Waveguide magneto-optic isolator fabricated by laser annealing,” *Appl. Phys. Lett.*, vol.53, pp.4-6 (1988).
- [14] M. Lohmeyer, N. Bahlmann, O. Zhuromskyy, H. Dötsch, and P. Hertel, “Phase-matched rectangular magneto-optic waveguides for applications in integrated optics isolators: numerical

- assessment,” *Opt. Commun.*, vol.158, pp.189-200 (1998).
- [15] S. Yamamoto, Y. Okamura, and T. Makimoto, “Analysis and design of semileaky-type thin-film optical waveguide isolator,” *IEEE J. Quantum Electron.*, vol.QE-12, pp.764-770 (1974).
- [16] S. T. Krisch, W. A. Biolsi, S. L. Blank, P. K. Tien, R. J. Martin, P. M. Bridenbaugh, and P. Grabbe, “Semileaky thin-film optical isolator,” *J. Appl. Phys.*, vol.52, pp.3190-3199 (1981).
- [17] T. Mizumoto and H. Saito, “Fabrication of semi-leaky optical isolator using surface activation bonding,” *IEICE Trans. on Electron.*, vol.J89-C, pp.423-424 (2006).
- [18] S. Yamamoto and T. Makimoto, “Circuit theory for a class of anisotropic and gyrotropic thin-film optical waveguides and design of nonreciprocal devices for integrated optics,” *J. Appl. Phys.*, vol.45, pp.882-888 (1974).
- [19] F. Auracher and H. H. Witte, “A new design for an integrated optical isolator,” *Opt. Commun.*, vol.13, pp.435-438 (1975).
- [20] T. Mizumoto and Y. Naito, “Nonreciprocal propagation characteristics of YIG thin film,” *IEEE Trans. on Microwave Theory and Technique*, vol.MTT-30, pp.922-925 (1982).
- [21] Y. Okamura, T. Negami, and S. Yamamoto, Integrated optical isolator and circulator using nonreciprocal phase shifters: a proposal,” *Appl. Opt.*, vol.23, pp.1886-1889 (1984).
- [22] N. Bahlmann, M. Lohmeyer, H. Dötsch, and P. Hertel, “Integrated magneto-optic Mach-Zehnder interferometer isolator for TE modes,” *Electron. Lett.*, vol.34, pp.2122-2123 (1998).
- [23] J. Fujita, M. Levy, and R. M. Osgood, Jr., “Waveguide optical isolator based on Mach-Zehnder interferometer,” *Appl. Phys. Lett.*, vol.76, pp.2158-2160 (2000).
- [24] H. Yokoi, Y. Shoji, E. Shin, and T. Mizumoto, “Interferometric optical isolator employing a nonreciprocal phase shift operated in a unidirectional magnetic field,” *Appl. Opt.*, vol.43, pp.4745-4752 (2004).
- [25] O. Zhuromskyy, M. Lohmeyer, N. Bahlmann, H. Dötsch, P. Hertel, and A. F. Popkov, “Analysis of polarization independent Mach-Zehnder-type integrated optical isolator,” *J. Lightwave Technol.*, vol.17, pp.1200-1205 (1999).
- [26] J. Fujita, M. Levy, R. M. Osgood, Jr., L. Wilkens, and H. Dötsch, “Polarization-independent waveguide optical isolator based on nonreciprocal phase shift,” *IEEE Photon. Technol. Lett.*, vol.12, pp.1510-1512 (2000).

- [27] T. Shintaku, "Integrated optical isolator based on efficient nonreciprocal radiation mode conversion," *Appl. Phys. Lett.*, vol.73, pp.1946-1948 (1998).
- [28] N. Bahlmann, M. Lohmeyer, O. Zhuromskyy, H. Dötsch, and P. Hertel, "Nonreciprocal coupled waveguides for integrated optical isolators and circulators for TM modes," *Opt. Commun.*, vol.161, pp.330-337 (1999).
- [29] O. Zhuromskyy, M. Lohmeyer, N. Bahlmann, H. Dötsch, P. Hertel, and A. F. Popcov, "Analysis of nonreciprocal light propagation in multimode imaging devices," *Opt. Quantum Electron.*, vol.32, pp.885-897 (2000).
- [30] M. Lohmeyer, N. Bahlmann, O. Zhuromskyy, H. Dötsch, and P. Hertel, "Integrated magneto-optic cross strip isolator," *Opt. Commun.*, vol.189, pp.251-259 (2001).
- [31] M. Lohmeyer, N. Bahlmann, O. Zhuromskyy, H. Dötsch, and P. Hertel, "Unidirectional magneto-optic polarization converters," *J. Lightwave Technol.*, vol.17, pp.2605-2611 (1999).
- [32] M. Takenaka and Y. Nakano, "Proposal of a novel semiconductor optical waveguide isolator," *Proceeding of 11th International Conference on Indium Phosphide and Related Materials*, pp.289-292 (1999).
- [33] W. Zayets and K. Ando, "Optical waveguide isolator based on nonreciprocal loss/gain of amplifier covered by ferromagnetic layer," *IEEE Photon. Technol. Lett.*, vol.11, pp.1012-1014 (1999).
- [34] H. Shimizu and Y. Nakano, "First demonstration of TE mode nonreciprocal propagation in an InGaAsP/InP active waveguide for an integrated optical isolator," *Jpn J. Appl. Phys.*, vol.43, pp.L1561-L1563 (2004).
- [35] W. V. Parys, B. Moeyersoon, D. V. Thourhout, R. Beats, M. Vanwolleghem, B. Dagens, J. Decobert, O. L. Guezigou, D. Make, R. Vanheertum, and L. Lagae, "Transverse magnetic mode nonreciprocal propagation in an amplifying AlGaAs/InP optical waveguide isolator," *Appl. Phys. Lett.*, vol.88, pp.071115-1-071115-3 (2006).
- [36] N. Sugimoto, H. Terui, A. Tate, Y. Katoh, Y. Yamada, A. Sugita, A. Shibukawa, and Y. Inoue, "A hybrid integrated waveguide isolator based on a silica-based planar lightwave circuit," *J. Lightwave Technol.* Vol.14, pp.2537-2546 (1996).
- [37] N. Sugimoto, T. Shintaku, A. Tate, H. Terui, M. Shimokozono, E. Kubota, M. Ishii, and Y. Inoue,

- “Waveguide polarization-independent optical circulator,” *IEEE Photn. Technol. Lett.*, vol.11, pp.355-357 (1999).
- [38] M. C. Debnath, V. Zayets, and K. Ando, “Complete magneto-optical TE-TM mode conversion in $\text{Cd}_{1-x}\text{Mn}_x\text{Te}$ waveguide for integrated optical isolator,” *Phys. Stat. Sol.*, vol.3, pp.1164-1167 (2006).
- [39] X. Guo, T. Zaman, and R. J. Ram, “Magneto-optical semiconductor waveguides for integrated isolators,” *Proceeding of SPIE; Optoelectronic Integrated Circuits VII*, vol.5729, pp.152-159 (2005).
- [40] H. Yokoi and T. Mizumoto, “Proposed configuration of integrated optical isolator employing wafer-direct bonding technique,” *Electron. Lett.*, vol.33, pp.1787-1788 (1997).
- [41] M. Bouda and Y. Nakano, “Development of metal-organic vapor phase diffusion enhanced selective area epitaxy, a novel metal-organic vapor phase epitaxy selective area growth technique, and its application to multi-mode interference device fabrication,” *Jpn. J. Appl. Phys.*, vol.38, pp.1029-1033 (1999).
- [42] H. Yokoi, T. Mizumoto, and Y. Shoji, “Optical nonreciprocal devices with a silicon guiding layer fabricated by wafer bonding,” *Appl. Opt.*, vol.42, pp.6605-6612 (2003).
- [43] R. L. Espinola, T. Izuhara, M.-C. Tsai, and R. M. Osgood, Jr., “Magneto-optical nonreciprocal phase shift in garnet/silicon-on-insulator waveguides,” *Opt. Lett.*, vol.29, pp.941-943 (2004).

Chapter 2:

Nonreciprocal Phase Shift for Magneto-Optical Isolator

2.1 Introduction

Optical nonreciprocal devices are indispensable to eliminate unwanted reflected light in the fiber link and protect optical active devices. The optical nonreciprocity is obtained from magneto-optic effect. A waveguide magneto-optical isolator employing nonreciprocal phase shift is investigated in this study. The nonreciprocal phase shift provides direction-dependent propagation constants due to the first-order magneto-optic effect with an external magnetic field applied transversally to the light propagation direction. A Mach-Zehnder interferometer configuration with the nonreciprocal phase shift realizes a magneto-optical isolator.

In this chapter, the nonreciprocal phase shift in a planar waveguide structure is analyzed by numerical calculation. Two numerical approaches are presented. One is solving directly the eigenvalue equation derived from the Maxwell equation with 1-dimensional (1-D) waveguide models. The other is a calculation using the perturbation theory with 2-dimensional (2-D) waveguide models. Then the principle of isolator operation and its design of the magneto-optical isolator are presented.

2.2 Theoretical analysis of nonreciprocal phase shift

The magneto-optic effects are described by the off-diagonal components of the dielectric permittivity tensor in a magneto-optic material [1]. The complex relative permittivity tensor of dielectric materials is given by

$$\tilde{\epsilon} = \begin{bmatrix} \epsilon_{xx} & \epsilon_{xy} & \epsilon_{xz} \\ \epsilon_{yx} & \epsilon_{yy} & \epsilon_{yz} \\ \epsilon_{zx} & \epsilon_{zy} & \epsilon_{zz} \end{bmatrix}. \quad (2.1)$$

As we consider loss-free material, the diagonal elements are real. The real and imaginary parts of the off-diagonal elements involve anisotropic and gyrotropic systems, respectively. Anisotropic systems are generated by the crystal-axis rotation in birefringent materials or the electro optic effect. Gyrotropic systems are generated by the magneto-optic effect. Since the corresponding elements such as ε_{xy} and ε_{yx} are complex conjugate to each other, the anisotropic systems are reciprocal due to the real part, and the gyrotropic systems are nonreciprocal due to the imaginary part. The imaginary off-diagonal elements are induced by an orthogonal magnetization. When the light propagates along the z -axis, the ε_{xy} induced by z -aligned magnetization is related to the Faraday rotation and the ε_{xz} or ε_{yz} induced by y - or x -aligned magnetization are related to the nonreciprocal phase shift.

In this section, the nonreciprocal phase shift is theoretically analyzed. We assume a loss-free magneto-optic waveguide in which the magneto-optic film is located in the x - z plane. The magnetization is aligned along the x -axis and lightwaves propagate along the z -axis. Here, a magneto-optic linear effect such as Cotton-Mouton effect is neglected. The relative permittivity of a magneto-optic film is then given by

$$\tilde{\varepsilon} = \begin{bmatrix} \varepsilon_x & 0 & 0 \\ 0 & \varepsilon_y & j\gamma \\ 0 & -j\gamma & \varepsilon_z \end{bmatrix} \quad (2.2)$$

where ε_x , ε_y , and ε_z are related to the isotropic refractive indices denoted as $\varepsilon = n^2$ in the x , y , and z direction, respectively. The off-diagonal elements γ are proportional to the specific Faraday rotation coefficient Θ_F by

$$\gamma = \frac{2n\Theta_F}{k_0} \quad (2.3)$$

where k_0 is the wavenumber in vacuum.

The Maxwell equation is written as

$$\nabla \times \mathbf{E} = -j\omega\mu_0\mathbf{H} \quad (2.4)$$

$$\nabla \times \mathbf{H} = j\omega\tilde{\varepsilon}\varepsilon_0\mathbf{E} \quad (2.5)$$

$$\nabla \cdot \mathbf{H} = 0 \quad (2.6)$$

$$\nabla \cdot (\tilde{\varepsilon}\mathbf{E}) = 0 \quad (2.7)$$

where ω is the angular frequency, \mathbf{E} and \mathbf{H} are the electric and magnetic field vectors, respectively, ϵ_0 and μ_0 are the permittivity and permeability of free space, respectively. From (2.2), the Maxwell equation (2.4) and (2.5) are rewritten in component form as

$$\frac{\partial E_z}{\partial y} - \frac{\partial E_y}{\partial z} = -j\omega\mu_0 H_x, \quad (2.8)$$

$$\frac{\partial E_x}{\partial z} - \frac{\partial E_z}{\partial x} = -j\omega\mu_0 H_y, \quad (2.9)$$

$$\frac{\partial E_y}{\partial x} - \frac{\partial E_x}{\partial y} = -j\omega\mu_0 H_z, \quad (2.10)$$

$$\frac{\partial H_z}{\partial y} - \frac{\partial H_y}{\partial z} = j\omega\epsilon_0 \epsilon_x E_x, \quad (2.11)$$

$$\frac{\partial H_x}{\partial z} - \frac{\partial H_z}{\partial x} = j\omega\epsilon_0 (\epsilon_y E_y + j\gamma E_z), \quad (2.12)$$

$$\frac{\partial H_y}{\partial x} - \frac{\partial H_x}{\partial y} = j\omega\epsilon_0 (\epsilon_z E_z - j\gamma E_y). \quad (2.13)$$

2.2.1 Solving eigenvalue equation with 1-D waveguide model

We consider a 1-dimensional waveguide model as shown in Fig. 2.1. The thickness of the guiding layer is defined d . Since all layers are uniform along the x -axis, $\partial/\partial x = 0$.

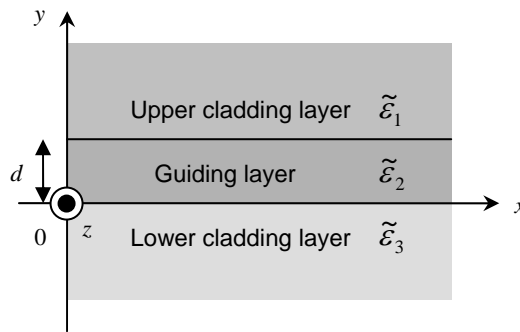


Fig. 2.1 Geometry of the three-layered slab waveguide model.

First, TM mode propagating along the z -axis is examined. Then the propagating modes are described by

$$\mathbf{E} = (0, E_y, E_z) \exp\{j(\omega t - \beta z)\}, \quad (2.14)$$

$$\mathbf{H} = (H_x, 0, 0) \exp\{j(\omega t - \beta z)\} \quad (2.15)$$

where β denotes the longitudinal propagation constants along the z -axis. From (2.12) and (2.13), E_y and E_z are expressed as

$$E_y = \frac{1}{\omega \epsilon_0 (\epsilon_y \epsilon_z - \gamma^2)} \left(\gamma \frac{\partial H_x}{\partial y} - j \epsilon_z \frac{\partial H_x}{\partial z} \right), \quad (2.16)$$

$$E_z = \frac{1}{\omega \epsilon_0 (\epsilon_y \epsilon_z - \gamma^2)} \left(\gamma \frac{\partial H_x}{\partial z} + j \epsilon_y \frac{\partial H_x}{\partial y} \right). \quad (2.17)$$

Substituting (2.16) and (2.17) into (2.8), we obtain the following wave equation for H_x

$$\frac{1}{\epsilon_y \epsilon_z - \gamma^2} \left(\epsilon_y \frac{\partial^2 H_x}{\partial y^2} + \epsilon_z \frac{\partial^2 H_x}{\partial z^2} \right) + k_0^2 H_x = 0 \quad (2.18)$$

where we use $k_0^2 = \omega^2 \epsilon_0 \mu_0$. Using $\partial/\partial z = -j\beta$, (2.18) is rewritten as

$$\frac{\partial^2 H_x}{\partial y^2} + \left(k_0^2 \epsilon' - \beta^2 \frac{\epsilon_z}{\epsilon_y} \right) H_x = 0 \quad (2.19)$$

with

$$\epsilon' = \frac{\epsilon_y \epsilon_z - \gamma^2}{\epsilon_y}. \quad (2.20)$$

For a guiding mode in the planar waveguide shown in Fig. 2.1, the effective refractive index $N (= \beta/k_0)$ must be

$$\epsilon_{y1}, \epsilon_{y3} < N^2 < \epsilon_{y2} \quad (2.21)$$

and the wave vectors along y -axis are defined with

$$k_0^2 \epsilon_i' - \frac{\epsilon_{zi}}{\epsilon_{yi}} \beta^2 = \begin{cases} -\eta_i^2 & (i=1,3) \\ k_2^2 & (i=2) \end{cases} \quad (2.22)$$

One can solve the wave equation (2.19) for each layer by

$$H_x = \begin{cases} A_1 \exp\{-\eta_1(y-d)\} \exp(-j\beta z) & (y \geq d) \\ (A_2 \cos k_2 y + B_2 \sin k_2 y) \exp(-j\beta z) & (0 \leq y < d) \\ A_3 \exp(\eta_3 y) \exp(-j\beta z) & (y < 0) \end{cases} \quad (2.23)$$

where A_1 , A_2 , B_2 , and A_3 are the field amplitudes. Substituting (2.23) into (2.17), E_z for each layer is obtained as

$$E_z = \begin{cases} \frac{(\gamma_1\beta + \eta_1\varepsilon_{y1})A_1}{j\omega\varepsilon_0\varepsilon_1'\varepsilon_{y1}} \exp\{-\eta_1(y-d)\} \exp(-j\beta z) \\ \frac{(\gamma_2\beta A_2 - \varepsilon_{y2}k_2B_2) \cos k_y y + (\gamma_2\beta B_2 + \varepsilon_{y2}k_2A_2) \sin k_y y}{j\omega\varepsilon_0\varepsilon_2'\varepsilon_{y2}} \exp(-j\beta z) \\ \frac{(\gamma_3\beta - \eta_3\varepsilon_{y3})A_3}{j\omega\varepsilon_0\varepsilon_3'\varepsilon_{y3}} \exp(\eta_3 y) \exp(-j\beta z) \end{cases} \quad (2.24)$$

Using the boundary condition that H_x and E_z are continuous across $y=0$ and $y=d$, we obtain the following eigenvalue equation

$$\tan k_2 d = \frac{\frac{k_2}{\varepsilon_2'} \left\{ \left(\eta_1 + \frac{\gamma_1\beta}{\varepsilon_1} \right) \frac{1}{\varepsilon_1'} + \left(\eta_3 - \frac{\gamma_3\beta}{\varepsilon_3} \right) \frac{1}{\varepsilon_3'} \right\}}{\frac{k_2^2}{\varepsilon_2'^2} - \left(\eta_1 + \frac{\gamma_1\beta}{\varepsilon_1} \right) \left(\eta_3 - \frac{\gamma_3\beta}{\varepsilon_3} \right) \frac{1}{\varepsilon_1'\varepsilon_3'} + \left\{ \left(\eta_3 - \frac{\gamma_3\beta}{\varepsilon_3} \right) \frac{1}{\varepsilon_3'} - \left(\eta_1 + \frac{\gamma_1\beta}{\varepsilon_1} \right) \frac{1}{\varepsilon_1'} \right\} \frac{\gamma_2\beta}{\varepsilon_2'\varepsilon_2} + \left(\frac{\gamma_2\beta}{\varepsilon_2'\varepsilon_2} \right)^2} \quad (2.25)$$

where ε_{yi} is simplified as ε_i for each layer $i=1, 2$, or 3 . This equation can be solved by a numerical analysis. Because of the linear terms in β involving the off-diagonal elements γ , there are nonreciprocal solutions for β as the propagation and magnetization directions. And the nonreciprocal phase shift is given by

$$\Delta\beta = \beta_+ - \beta_- \quad (2.26)$$

Notice that, when the slab structure is symmetric denoted as $\varepsilon_1=\varepsilon_3$ and $\gamma_1=\gamma_3$, the linear terms in β vanish and $\Delta\beta$ becomes zero. This means that the nonreciprocal phase shift is induced by the asymmetry of the waveguide structure transversally to the magnetization direction. The difference in the propagation constant means the difference in the distribution of electro-magnetic field depending on the propagation direction.

Next, TE mode propagating along the z -axis is examined. The propagating modes are described by

$$\mathbf{E} = (E_x, 0, 0) \exp\{j(\omega t - \beta z)\}, \quad (2.27)$$

$$\mathbf{H} = (0, H_y, H_z) \exp\{j(\omega t - \beta z)\}. \quad (2.28)$$

Substituting (2.9) and (2.10) into (2.11), we obtain the following wave equation for E_x

$$\frac{\partial^2 E_x}{\partial y^2} + (k_0^2 \epsilon_x - \beta^2) E_x = 0. \quad (2.29)$$

With the wave vectors along the y -axis

$$k_0^2 \epsilon_{xi} - \beta^2 = \begin{cases} -\eta_i^2, & (i=1,3) \\ k_2^2, & (i=2) \end{cases} \quad (2.30)$$

one can solve (2.29) for E_x and H_z . Using the boundary condition for E_x and H_z across $y=0$ and $y=d$, we obtain the following eigenvalue equation

$$\tan k_2 d = \frac{k_2(\eta_1 + \eta_3)}{k_2^2 - \eta_1 \eta_3}. \quad (2.31)$$

Since there are no linear terms in β , nonreciprocal phase shift is not induced for TE mode propagations with the magnetization along the x -axis.

In the same way, we consider a four-layered waveguide model shown in Fig. 2.2. An interlayer with the thickness of d_2 is inserted above the guiding layer with the thickness of d_3 . TM propagating modes are described as (2.14) and (2.15), and we obtain the same wave equation as (2.19). The wave vectors along the y -axis are defined with

$$k_0^2 \epsilon_i - \frac{\epsilon_{zi}}{\epsilon_{yi}} \beta^2 = \begin{cases} -\eta_i^2, & (i=1,4) \\ \pm \eta_2^2, & (i=2) \\ k_3^2, & (i=3) \end{cases} \quad (2.32)$$

where the sign of $i=2$ is positive when the interlayer works as a part of core layer as $\epsilon_2 > N^2$ and negative when it works as a cladding layer as $\epsilon_2 < N^2$. The solutions for H_x are given by

$$H_x = \begin{cases} A_1 \exp\{-\eta_1(y - d_2 - d_3)\} \exp(-j\beta z) & (y \geq d_2 + d_3) \\ [A_2 \exp\{\eta_2(y - d_3)\} + B_2 \exp\{-\eta_2(y - d_3)\}] \exp(-j\beta z) & (d_3 \leq y < d_2 + d_3) \\ (A_3 \cos k_3 y + B_3 \sin k_3 y) \exp(-j\beta z) & (0 \leq y < d_3) \\ A_4 \exp(\eta_4 y) \exp(-j\beta z) & (y < 0) \end{cases} \quad (2.33)$$

Substituting (2.33) into (2.17), E_z for each layer is obtained. Using the boundary condition that H_x and E_z are continuous across $y=0$, $y=d_2$ and $y=d_2+d_3$, we obtain the following eigenvalue equation

$$\left(\eta_4 - \frac{\gamma_4\beta}{\varepsilon_4}\right)\frac{1}{\varepsilon'_4} + \frac{\gamma_3\beta}{\varepsilon'_3\varepsilon_3} - \frac{k_3}{\varepsilon'_3}C_0 = 0 \quad (2.34)$$

where

$$C_0 = \left[\left\{ \left(\eta_2 - \frac{\gamma_2\beta}{\varepsilon_2} \right) \frac{1}{\varepsilon'_2} - \left(\eta_2 + \frac{\gamma_2\beta}{\varepsilon_2} \right) \frac{1}{\varepsilon'_2} C_1 \right\} \frac{1}{1+C_1} \cos k_3 d_3 + \frac{\gamma_3\beta}{\varepsilon'_3\varepsilon_3} \cos k_3 d_3 + \frac{k_3}{\varepsilon'_3} \sin k_3 d_3 \right] \\ \left/ \left[\left\{ - \left(\eta_2 - \frac{\gamma_2\beta}{\varepsilon_2} \right) \frac{1}{\varepsilon'_2} + \left(\eta_2 + \frac{\gamma_2\beta}{\varepsilon_2} \right) \frac{1}{\varepsilon'_2} C_1 \right\} \frac{1}{1+C_1} \sin k_3 d_3 - \frac{\gamma_3\beta}{\varepsilon'_3\varepsilon_3} \sin k_3 d_3 + \frac{k_3}{\varepsilon'_3} \cos k_3 d_3 \right] \right. \quad (2.35)$$

and

$$C_1 = - \left\{ \left(\eta_1 + \frac{\gamma_1\beta}{\varepsilon_1} \right) \frac{1}{\varepsilon'_1} + \left(\eta_2 - \frac{\gamma_2\beta}{\varepsilon_2} \right) \frac{1}{\varepsilon'_2} \right\} \exp(2\eta_2 d_2) \left/ \left\{ \left(\eta_1 + \frac{\gamma_1\beta}{\varepsilon_1} \right) \frac{1}{\varepsilon'_1} - \left(\eta_2 + \frac{\gamma_2\beta}{\varepsilon_2} \right) \frac{1}{\varepsilon'_2} \right\} \right. . \quad (2.36)$$

This equation can be solved by a numerical analysis. The linear terms in β involving the off-diagonal elements γ induce nonreciprocal solutions for β , and the nonreciprocal phase shift $\Delta\beta$ is obtained.

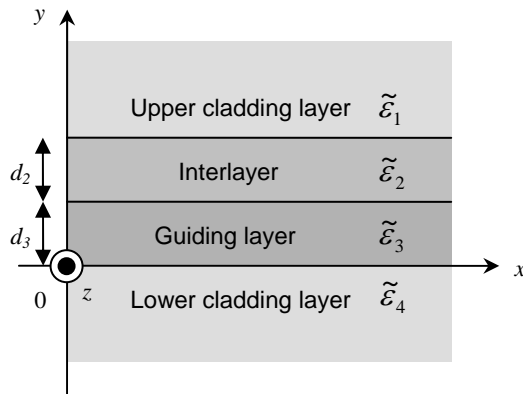


Fig. 2.2 Geometry of the four-layered slab waveguide model.

2.2.2 Perturbation theory with 2-D waveguide model

We consider a 2-dimensional waveguide model as shown in Fig. 2.3. In this case, the wave equation for H_x derived from the Maxwell equation (2.4)-(2.7) has differential terms $\partial/\partial x$, $\partial/\partial y$ with respect to x and y . The 2-D Maxwell equation considering $\partial/\partial x$ and $\partial/\partial y$ with the magneto-optic effect is a complex system even though a directly solution by finite element method is reported [2]. Easier way to obtain the nonreciprocal phase shift is using perturbation theory [1,3,4]. When the off-diagonal elements γ of the permittivity tensor are much smaller than the diagonal elements ε , the gyrotropic effect can be treated as a perturbation in an unperturbed system without magnetization. The nonreciprocal propagation constants are given by

$$\beta_{\pm} = \beta_0 \pm \frac{\Delta\beta}{2} \quad (2.37)$$

where β_0 is the propagation constant of the unperturbed system. In perturbation theory, the nonreciprocal characteristic is given by

$$\Delta\beta = \frac{2\omega\varepsilon_0}{P} \iint E^* \Delta\tilde{\varepsilon} E dx dy \quad (2.38)$$

normalized by the power flow in the z direction

$$P = \left(\iint E \times H^* + E^* \times H \right)_z dx dy. \quad (2.39)$$

\mathbf{E} and \mathbf{H} are the electric and magnetic fields of the unperturbed system and $\Delta\tilde{\varepsilon}$ is the perturbation induced by the magnetization.

Using the semi-vector approximation, TM modes propagating along the z -axis are described by

$$\mathbf{E} = (0, E_y, E_z) \exp\{j(\omega t - \beta z)\}, \quad (2.40)$$

$$\mathbf{H} = (H_x, 0, 0) \exp\{j(\omega t - \beta z)\}. \quad (2.41)$$

From (2.12) and (2.13), E_y and E_z of the unperturbed system are expressed as

$$E_y = -\frac{j}{\omega\varepsilon_0\varepsilon_y} \frac{\partial H_x}{\partial z}, \quad (2.42)$$

$$E_z = \frac{j}{\omega\varepsilon_0\varepsilon_z} \frac{\partial H_x}{\partial y}. \quad (2.43)$$

Then a magnetization along the x -axis yields the perturbation along the y -axis for TM modes, and the nonreciprocal phase shift is given by

$$\begin{aligned}
 \Delta\beta &= \frac{2\omega\epsilon_0}{P} \iint \begin{bmatrix} 0 & E_y^* & E_z^* \\ 0 & 0 & j\gamma \\ 0 & -j\gamma & 0 \end{bmatrix} \begin{bmatrix} 0 \\ E_y \\ E_z \end{bmatrix} dx dy \\
 &= \frac{2\omega\epsilon_0}{P} \iint \{E_y^*(j\gamma)E_z + E_z^*(-j\gamma)E_y\} dx dy \\
 &= \frac{2\omega\epsilon_0}{P} \iint 2 \operatorname{Re}\{j\gamma E_y^* E_z\} dx dy \\
 &= \frac{2}{P} \iint \frac{2\gamma\beta}{\omega\epsilon_0\epsilon_y\epsilon_z} H_x \frac{\partial H_x}{\partial y} dx dy, \tag{2.44}
 \end{aligned}$$

$$\begin{aligned}
 P &= \iint \{E_y H_x^* + H_x^* E_y\} dx dy \\
 &= 2 \operatorname{Re} \iint E_y^* H_x dx dy = \frac{2\beta}{\omega\epsilon_0\epsilon_y} \iint |H_x|^2 dx dy. \tag{2.45}
 \end{aligned}$$

The integral term of y in (2.44) exists only across the interfaces of the magneto-optic layer at $y=y_m$ as

$$\int \frac{\gamma}{\epsilon_y\epsilon_z} \frac{\partial H_x}{\partial y} dy = \left[\frac{\gamma}{\epsilon_y\epsilon_z} H_x \right]_{y_m-0} - \left[\frac{\gamma}{\epsilon_y\epsilon_z} H_x \right]_{y_m+0}. \tag{2.46}$$

Finally, we obtain

$$\Delta\beta = \frac{\sum_m \nu \int \gamma(\epsilon_y\epsilon_z)^{-1} |H_x(y_m)|^2 dx}{\iint \epsilon_y^{-1} |H_x|^2 dx dy} \tag{2.47}$$

where ν is $+1$ or -1 determined by the position of magneto-optic layer in (2.46).

The $|H_x|$ of the unperturbed system can be calculated by numerical simulation such as a beam propagation method (BPM) or a finite element method (FEM). The numerator of (2.47) is obtained from the calculation of the integral of off-diagonal elements, permittivity tensors, and simulated magnetic fields along the magneto-optic interface. The denominator of (2.47) is obtained from the integral of permittivity tensors and simulated fields all over the simulation region.

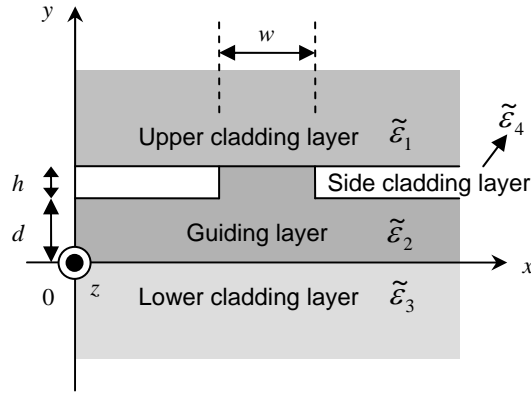


Fig. 2.3 Geometry of the 2-D waveguide model.

2.2.3 Calculation results and comparison

In this study, a cerium-substituted yttrium iron garnet $\text{CeY}_2\text{Fe}_5\text{O}_{12}$ (Ce:YIG) grown on a (Ca,Mg,Zr)-doped GGG substrate (SGGG) is used as the magneto-optic garnet. The Faraday rotation coefficient Θ_F of Ce:YIG is -4500 deg/cm, which corresponds to the off-diagonal permittivity γ of 0.008525, at $\lambda=1.55$ μm [5]. As described in Chapter 1, our group has proposed the magneto-optical isolator employing nonreciprocal phase shift with some material systems. Here, we consider three kinds of waveguide structure as shown in Fig. 2.4, (a) $\text{SiO}_2/\text{Ce:YIG}/\text{SGGG}$, (b) $\text{Ce:YIG}/\text{GaInAsP}/\text{InP}$, and (c) $\text{Ce:YIG}/\text{Si}/\text{SiO}_2$ -layered structures, respectively. Rib waveguides are formed on the guiding layer to confine lightwave laterally. The latter two structures have side-cladding layer of air so that they are realized by a direct bonding [6-8]. The refractive indices of the material at $\lambda=1.55$ μm are shown in Table 2.1.

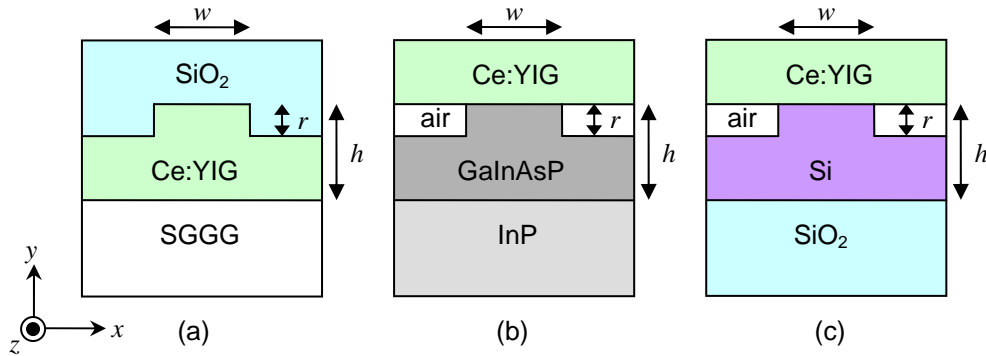


Fig. 2.4 Waveguide structures for magneto-optical isolator.

Table 2.1 Refractive indices at $\lambda = 1.55 \mu\text{m}$.

Material	Refractive index
Ce:YIG	2.20
SGGG	1.94
GaInAsP ($\lambda_g = 1.42 \mu\text{m}$)	3.45
InP	3.17
Si	3.48
SiO ₂	1.44

Figure 2.5 shows calculation results of the nonreciprocal phase shift as a function of waveguide height h . Dashed lines are calculated by solving eigenvalue equation with 1-D slab waveguide model where the side cladding layer is neglected. Solid lines are calculated by the perturbation theory with 2-D waveguide model where the unperturbed magnetic field is simulated by the mode solving via imaginary distance BPM [9,10]. In the semi-vector simulation, the magnetic fields are derived from the electric fields. For all the structure, the waveguide width w and rib height r are fixed at $2.0 \mu\text{m}$ and $0.1 \mu\text{m}$, respectively. The simulation grid sizes along x - and y -axis are $\Delta x = 0.05 \mu\text{m}$ and $\Delta y = 0.01 \mu\text{m}$, respectively, and the slice step along z -axis is $\Delta z = 0.005 - 0.05 \mu\text{m}$. There is little difference in the results between two methods, solving eigenvalue equation and perturbation theory. It is observed that a large nonreciprocal phase shift is obtained from the waveguide structure with Ce:YIG/Si/SiO₂. This is because there is a large intensity of the magnetic field at the interface between Ce:YIG and Si layer as can be seen in Fig. 2.6.

Figure 2.7 shows calculation results of the nonreciprocal phase shift for different waveguide widths with 2-D structure. Here, we use the waveguide structure with Ce:YIG/Si/SiO₂ and the rib height is the same as the waveguide height, i.e., it is a channel waveguide. The simulation grid sizes are $\Delta x = 0.01 \mu\text{m}$ and $\Delta y = 0.01 \mu\text{m}$ to model the narrow waveguide width. As is the particular problem for the software, spin-off intensity peaks sometime appear on the magnetic fields at the waveguide corners as shown in Fig. 2.8. The semi-vector simulation derives the magnetic fields from the firstly calculated electric fields so

as to satisfy the Maxwell equation. They appear only when the simulation is carried with small grid size for a high-index-contrast waveguide. These must be eliminated when the nonreciprocal phase shift is calculated using the magnetic fields. As you can see in Fig. 2.7, the maximum nonreciprocal phase shift becomes small for narrower width. This means that the magnetic field distribution is broaden in the vertical direction due to the lateral optical confinement as the waveguide width is narrow. Consequently, we should calculate the nonreciprocal phase shift with 2-D structure instead of 1-D structure if the lateral optical confinement is strong in the waveguide structure.

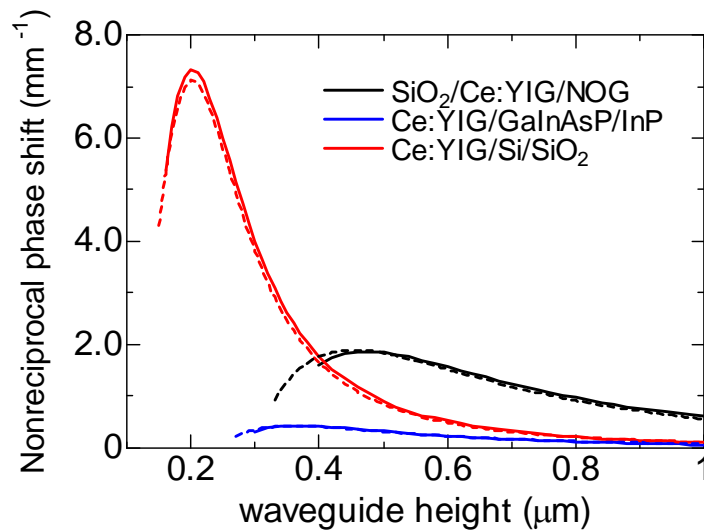


Fig.2.5 Calculated nonreciprocal phase shift for some waveguide structures. Dashed lines are calculated by solving eigenvalue equation with 1-D structure and Solid lines are calculated by perturbation theory with 2-D structure, at $\lambda = 1.55 \mu\text{m}$.

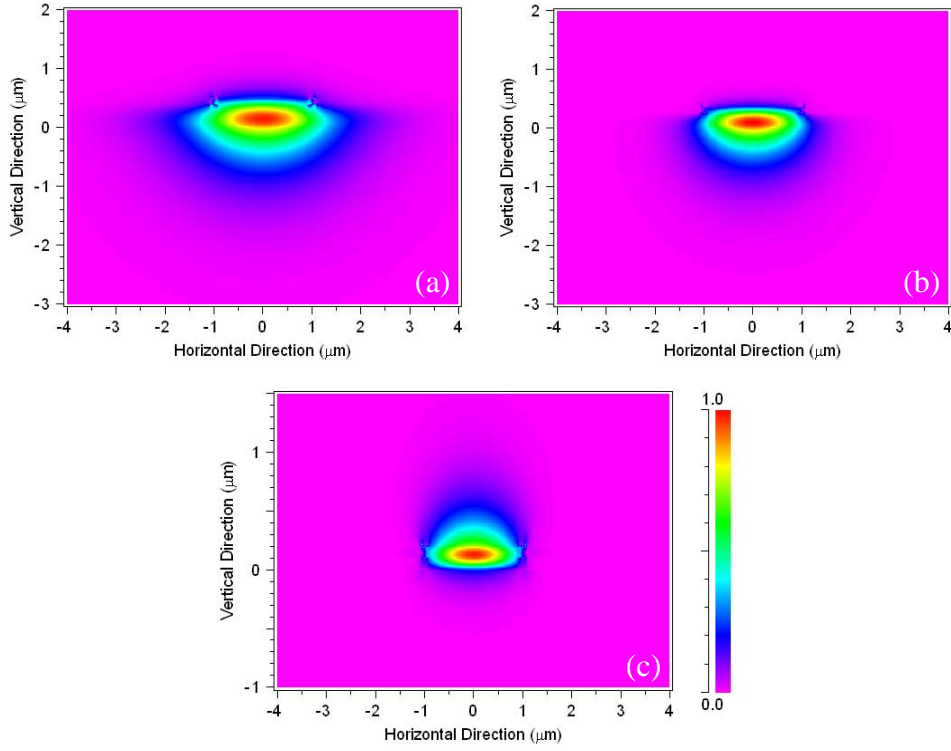


Fig. 2.6 Mode profiles of magnetic field calculated by semi-vector BPM.

(a) $\text{SiO}_2/\text{Ce:YIG}/\text{SGGG}$ at $h = 0.48\mu\text{m}$, (b) $\text{Ce:YIG}/\text{GaInAsP}/\text{InP}$ at $h = 0.36\mu\text{m}$, and (c) $\text{Ce:YIG}/\text{Si}/\text{SiO}_2$ at $h = 0.20\mu\text{m}$. All the width and rib height are $w = 2.0\mu\text{m}$ and $r = 0.1\mu\text{m}$, respectively.

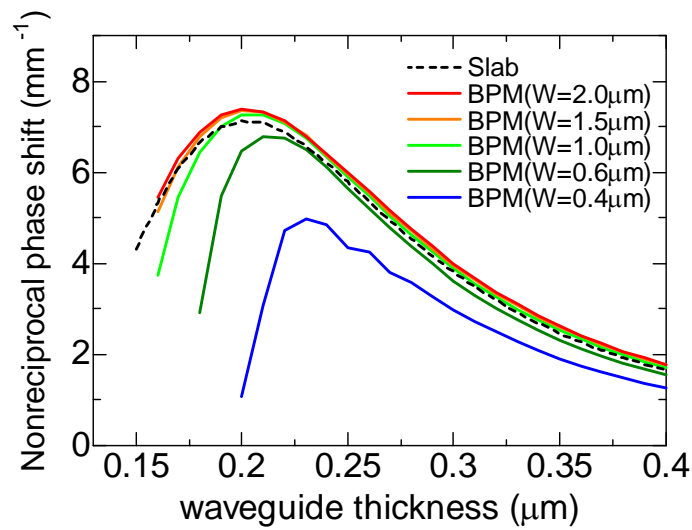


Fig.2.7 Calculated nonreciprocal phase shift for some waveguide width with the $\text{Ce:YIG}/\text{Si}/\text{SiO}_2$ structure, at $\lambda = 1.55\mu\text{m}$.

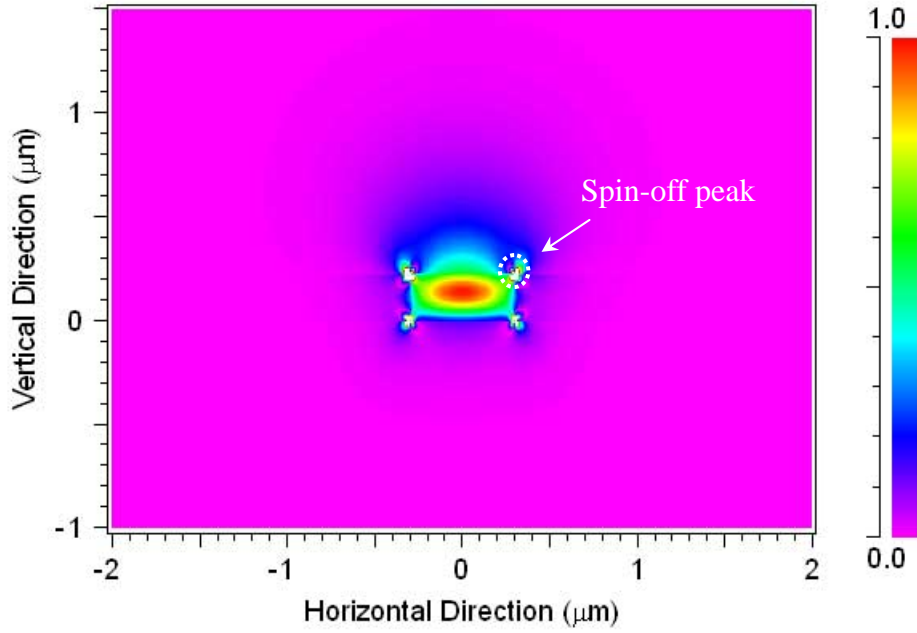


Fig. 2.8 Mode profile of magnetic field with the Ce:YIG/Si/SiO₂ structure at $w = 0.6\mu\text{m}$ and $h = r = 0.20\mu\text{m}$.

Next, we compare the simulation methods to calculate the magnetic field distribution with 2-D structure. The mode solving via semi-vector BPM, full-vector BPM, and full-vector FEM are considered [9,11]. The full-vector simulations provide H_x and H_y fields which are distinguished major or minor component as their distributions. Typically, major and minor components are distributed at the center and the corner in the waveguide, respectively. The H_x of major component is called quasi-TM mode or TM-like mode.

Figures 2.9 and 2.10 show the calculation results for comparison of the semi-vector BPM with the full-vector BPM and the full-vector FEM, respectively. The waveguide is composed of SiO₂/Ce:YIG/SGGG and is a channel waveguide $h=r$. The magnetic fields are calculated directly in the full-vector simulations where no spin-off peaks appear as shown in Fig. 2.11. The semi-vector BPM shows larger maximum nonreciprocal phase shift than the full-vector simulations for small dimension of the waveguide. At the same time, the semi-vector BPM gives larger propagation constant than the full-vector simulations. This difference is thought to be caused by the spin-off peaks at the waveguide corners as mentioned above. The peaks

seem to prevent the field distribution from broadening to upper region as can be seen in Fig. 2.11 (a). This results in large distribution of the magnetic field at the magneto-optic interface and enhances the nonreciprocal phase shift.

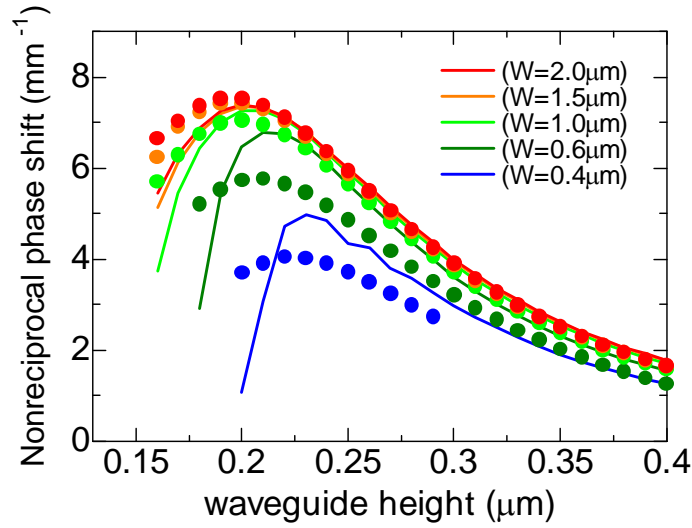


Fig. 2.9 Comparison between semi-vector BPM and full-vector BPM. The lines are calculated by the semi-vector BPM, and the dots are calculated by the full-vector BPM.

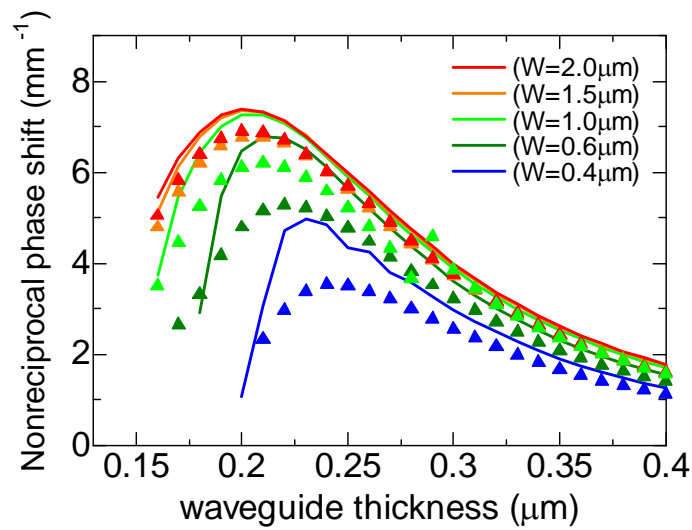


Fig. 2.10 Comparison between semi-vector BPM and full-vector FEM. The lines are calculated by the semi-vector BPM, and the dots are calculated by the full-vector FEM.

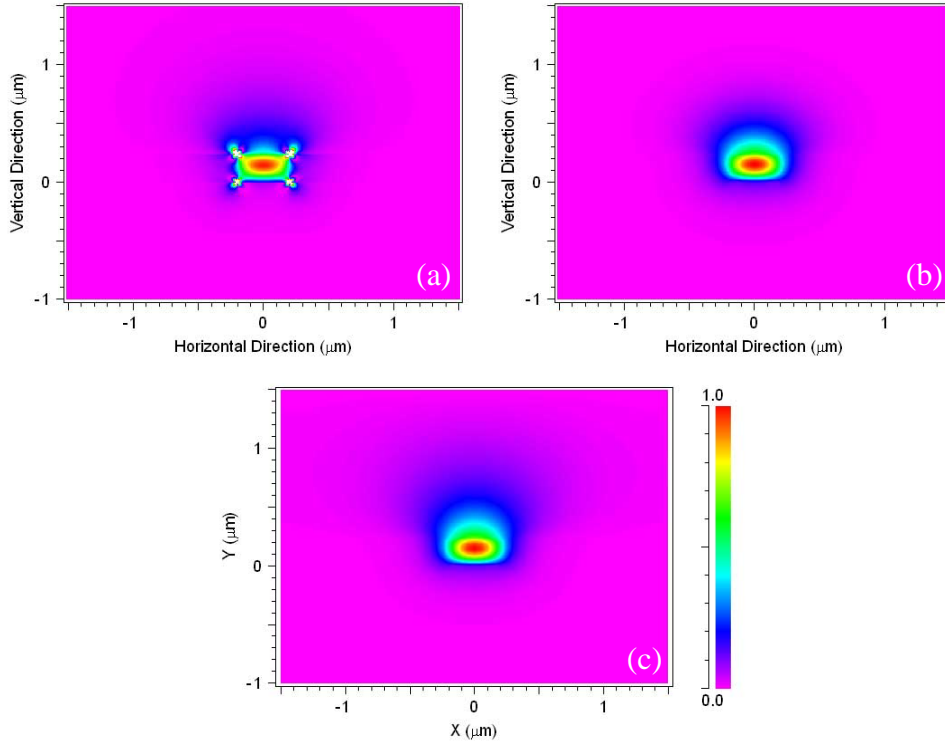


Fig. 2.11 Mode profiles of magnetic field with the $\text{SiO}_2/\text{Ce:YIG}/\text{SGGG}$ structure at $w=0.40\mu\text{m}$ and $h=0.24\mu\text{m}$ calculated by (a) semi-vector BPM, (b) full-vector BPM, and (c) full-vector FEM.

The discontinuity of the data for $w=1.0\mu\text{m}$ in Fig. 2.10 is due to hybrid supermodes. To understand the hybrid supermodes, effective refractive indices and nonreciprocal phase shift are calculated at the fixed height of $0.28\mu\text{m}$ as shown in Fig. 2.12 and Fig. 2.13. The mode-0 corresponds to the TE_0 mode. On the other hand, as the width increase, the mode-1 changes from TM_0 mode into TE_1 mode, and the mode-2 changes from TE_1 mode into TM_0 mode across $w \sim 1.0\mu\text{m}$. The nonreciprocal phase shift is calculated with H_x component considered as TM_0 mode. The magnetic field distributions around the cross point of mode-1 and mode-2 are shown in Table 2.2. At $w=1.0\mu\text{m}$, the H_x and H_y can not be distinguished as major or minor component, then they are considered as hybrid supermodes. This behavior of the mode transition affects the field distributions at $w \sim 1.0\mu\text{m}$. For example, H_{x1} at $w=0.95\mu\text{m}$ and H_{x2} at $w=1.0\mu\text{m}$ are slightly pushed up and down, respectively. Therefore, the nonreciprocal phase shift calculated from the field distributions becomes discontinuous across $w \sim 1.0\mu\text{m}$.

As a result, we should not design a waveguide with such parameter as hybrid supermode appears because they induce mode transition between TM fundamental and TE higher-order modes. Such mode transition is observed during the full-vector BPM simulation when the propagation constant of TM_0 is close to that of TE_1 .

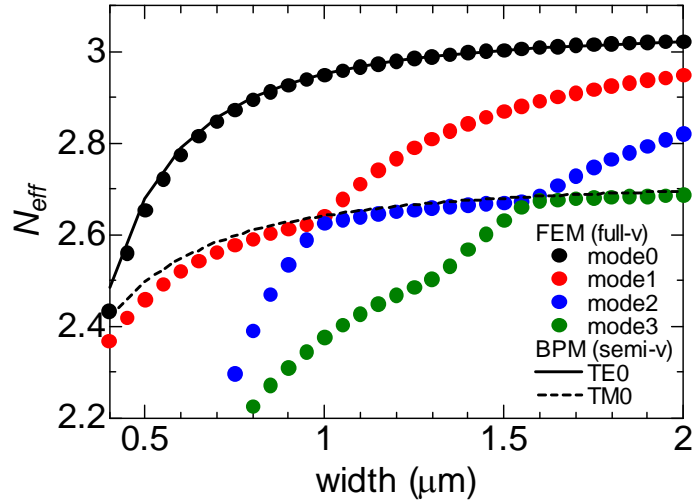


Fig. 2.12 Effective refractive indices simulated by semi-vector BPM and full-vector FEM with the Ce:YIG/Si/SiO₂ structure at $h = r = 0.28 \mu\text{m}$.

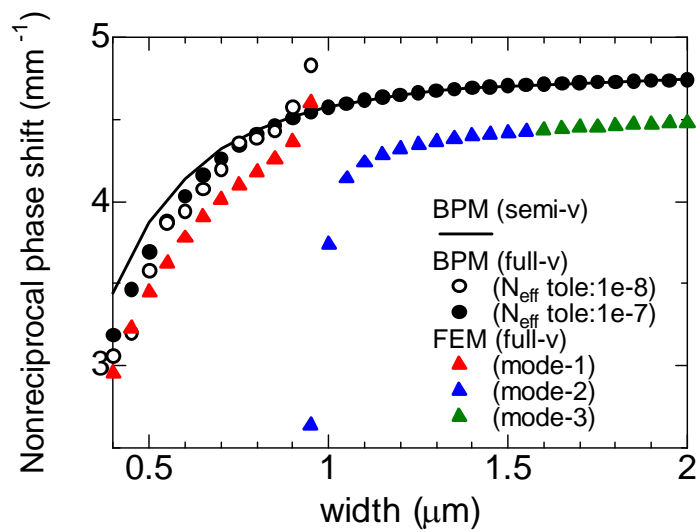
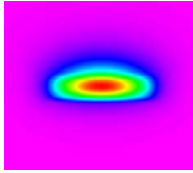
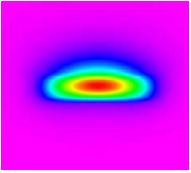
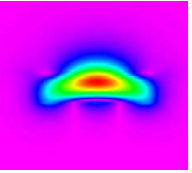
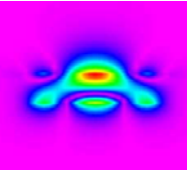
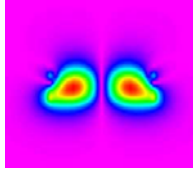
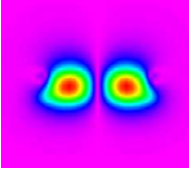
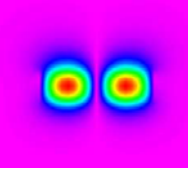
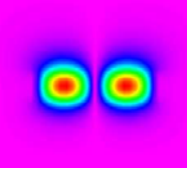
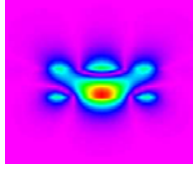
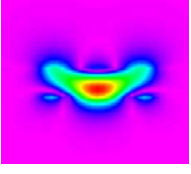
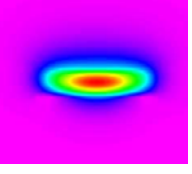
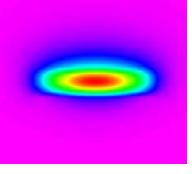
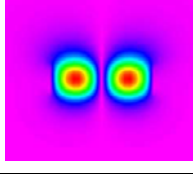
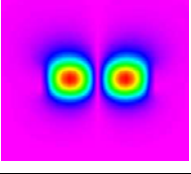
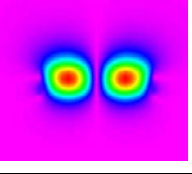
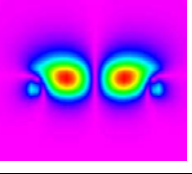


Fig. 2.13 Calculated nonreciprocal phase shift using the magnetic fields simulated by semi-vector BPM and full-vector FEM.

Table 2.2 Mode profiles of magnetic field calculated by full-vector FEM with the Ce:YIG/Si/SiO₂ structure at $h=r=0.28\text{ }\mu\text{m}$.

w	$0.9\text{ }\mu\text{m}$	$0.95\text{ }\mu\text{m}$	$1.0\text{ }\mu\text{m}$	$1.05\text{ }\mu\text{m}$
H_{x1}				
H_{y1}				
H_{x2}				
H_{y2}				

2.3 Principle of isolator operation

In this section, the principle of a magneto-optical isolator operation employing nonreciprocal phase shift is described. Figure 2.14 shows the basic configuration of the isolator which is a Mach-Zehnder interferometer with nonreciprocal and reciprocal phase shifters. Hence we utilize the nonreciprocal phase shift for TM mode, the isolator operates for TM mode. External magnetic fields are applied in anti-parallel direction to the two arms of the nonreciprocal phase shifter. These provide direction-dependent propagation constants for the lightwave traveling in each arm. The nonreciprocal phase differences θ_N between the two arms are given by

$$\theta_{N(\text{forward})} = (\beta_{f1} - \beta_{f2})L, \quad (2.48)$$

$$\theta_{N(\text{backward})} = (\beta_{b1} - \beta_{b2})L \quad (2.49)$$

where L is the propagation length of the nonreciprocal phase shifter. When the waveguide structures of the two arms are symmetric, the θ_N has different sign depending on the propagation direction

$$\beta_0 - \Delta\beta/2 = \beta_{f1} = \beta_{b2}, \quad (2.50)$$

$$\beta_0 + \Delta\beta/2 = \beta_{f2} = \beta_{b1}. \quad (2.51)$$

In the isolator operation, the θ_N are set at $-\pi/2$ and $+\pi/2$ in the forward and backward directions, respectively. The reciprocal phase difference θ_R is set at $+\pi/2$ by an optical path difference ΔL between the two arms given by

$$\theta_R = \beta \cdot \Delta L \quad (2.52)$$

where β is the longitudinal propagation constant of the mode propagating in the waveguide of reciprocal phase shifter.

A forward traveling wave from the input port is divided into two waves with identical amplitudes and phases at the 3dB coupler. The nonreciprocal phase difference is cancelled by the reciprocal one and the total phase difference is 0. So the two waves are coupled to the output port by the constructive interference at the 3dB coupler. A backward traveling wave from the output port is divided into identical two waves at the 3dB coupler. In this time, the nonreciprocal phase shift is added to the reciprocal one and the total phase difference is $+\pi$. Then the two waves are not coupled to the input port and radiated at the 3dB coupler by the destructive interference. Consequently, the MZI functions as a magneto-optical isolator. Table 2.3 shows designed length of the nonreciprocal and reciprocal phase shifters for some waveguide structures. The refractive indices as shown in the Table 2.1 are used.

The output intensity of a MZI is given by [12]

$$\begin{aligned} |E_{out}|^2 &= \left| \frac{-j}{2} \left(\sqrt{a_1} e^{j\theta_1} + \sqrt{a_2} e^{j\theta_2} \right) E_{in} \right|^2 \\ &= \frac{1}{4} \left\{ a_1 + a_2 + 2\sqrt{a_1 a_2} \cos(\theta_2 - \theta_1) \right\} |E_{in}|^2 \end{aligned} \quad (2.53)$$

where E_{in} and E_{out} are the amplitudes of the electric field at the input and output ports and θ_1 , θ_2 , a_1 , and a_2 are the phase differences and attenuations of intensity in each arm. As the 3 dB coupler divided a wave into two waves with identical phase and amplitude, and the waves

propagate without any attenuation in both arms, the (2.53) is rewritten as

$$|E_{out}|^2 = \frac{1 + \cos(\theta_2 - \theta_1)}{2} |E_{in}|^2. \quad (2.54)$$

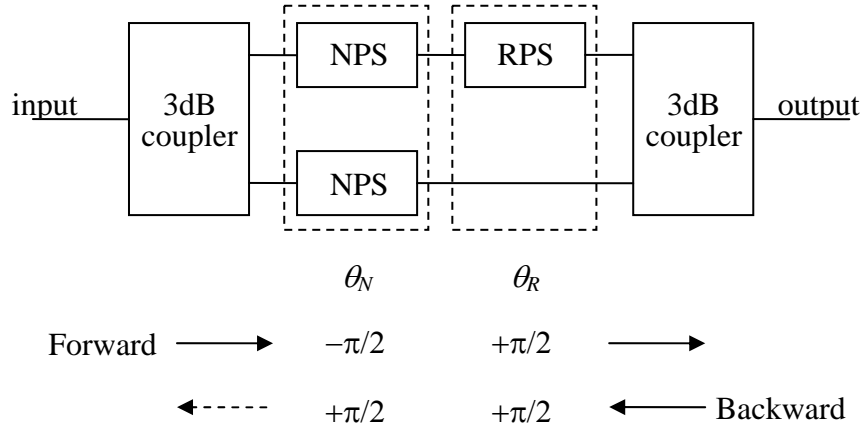


Fig. 2.14 Basic configuration of the magneto-optical isolator employing nonreciprocal phase shift. NPS: Nonreciprocal phase shifter, RPS: Reciprocal phase shifter.

Table 2.3 Designed lengths of nonreciprocal and reciprocal phase shifters.

$\Theta_F = -4500$ deg/cm of Ce:YIG at $\lambda = 1.55$ μm .

Structure	Parameters $w/h/r$ (μm)	L_{NPS} (mm)		L_{RPS} (μm)	
		(a)	(b)	(a)	(b)
SiO ₂ /Ce:YIG/SGGG	2.0 / 0.48 / 0.10	0.840	0.839	0.196	0.196
Ce:YIG/GaInAsP/InP	2.5 / 0.36 / 0.16	3.498	3.661	0.121	0.121
Ce:YIG/Si/SiO ₂	2.0 / 0.20 / 0.01	0.213	0.231	0.164	0.165
Ce:YIG/Si/SiO ₂	0.6 / 0.22 / 0.22	0.233	0.298	0.168	0.170

(a) semi-vector BPM, (b) full-vector FEM

2.4 Summary

In this chapter, the nonreciprocal phase shift is analyzed by numerical calculation. Using 1-D and 2-D waveguide models, the nonreciprocal phase shift is calculated. For narrower waveguide, 2-D model should be used for taking the effect of the lateral optical confinement into account. In the comparison among the several mode solving methods, reliable results are obtained by using full-vector simulations than semi-vector BPM. However, the full-vector simulations take much time to obtain the field distributions and make it complex due to the hybrid supermode.

References

- [1] S. Yamamoto and T. Makimoto, "Circuit theory for a class of anisotropic and gyrotropic thin-film optical waveguides and design of nonreciprocal devices for integrated optics," *J. Appl. Phys.*, vol.45, pp.882-888 (1974).
- [2] M. Koshiba and X-P. Zhuang, "An efficient finite-element analysis of magneto-optic channel waveguides," *J. Lightwave Technol.*, vol.11, pp.1453-1458 (1993).
- [3] M. Shamonin and P. Hertel, "Analysis of nonreciprocal mode propagation in magneto-optic rib-waveguide structures with the spectral-index method," *Appl. Opt.*, vol.33, pp.6415-6421 (1994).
- [4] N. Bahlmann, V. Chandrasekhara, A. Erdmann, R. Gerhardt, P. Hertel, R. Lehmann, D. Salz, F-J. Schröteler, M. Wallenhost, and H. Dötsch, "Improved design of magneto-optic rib waveguides for optical isolators," *J. Lightwave Technol.*, vol.16, pp.818-823 (1998).
- [5] T. Shintaku, "Integrated optical isolator based on efficient nonreciprocal radiation mode conversion," *Appl. Phys. Lett.*, vol.73, pp.1946-1948 (1998).
- [6] H. Yokoi and T. Mizumoto, "Proposed configuration of integrated optical isolator employing wafer-direct bonding technique," *Electron. Lett.*, vol.33, pp.1787-1788 (1997).
- [7] H. Yokoi, T. Mizumoto, and Y. Shoji, "Optical nonreciprocal devices with a silicon guiding layer fabricated by wafer bonding," *Appl. Opt.*, vol.42, pp.6605-6612 (2003).
- [8] R. L. Espinola, T. Izuhara, M.-C. Tsai, and R. M. Osgood, Jr., "Magneto-optical nonreciprocal phase shift in garnet/silicon-on-insulator waveguides," *Opt. Lett.*, vol.29, pp.941-943 (2004).
- [9] BeamPROP software from RSoft Design Group, (<http://www.rsoftdesign.com/>)
- [10] S. Jungling and J. C. Chen, "A study and optimization of eigenmode calculations using the imaginary-distance beam-propagation methods for modal analysis," *J. Quantum Electron.*, vol.30, pp.2098-2105 (1994).
- [11] FemSIM software from RSoft Design Group, (<http://www.rsoftdesign.com/>)
- [12] T. Suhara, "Optical-wave Engineering (Kouha-kougaku)," (Corona publishing co., ltd., Tokyo, 1998), Chap.3, p.49. (in Japanese)

Chapter 3:

Magneto-Optical Isolator with Silicon Waveguides Fabricated by Direct Bonding Technique

3.1 Introduction

A silicon-on-insulator (SOI) material system is an efficient platform for both electronic and photonic devices. The high refractive index contrast of a Si waveguide enables one to realize ultracompact photonic devices and dense integrated optical circuits [1]. A high speed optical modulator based on a MOS capacitor has attracted much attention for advanced Si photonics [2]. In addition, combining III-V compound semiconductors that have direct bandgap and high mobility with Si-LSI provides new scope of optoelectronic integrated circuits (OEICs). Because, Si offers several advantages that it is low-cost, mechanically strong, and transparent at the emission and absorption wavelengths of III-V materials. A hybrid evanescent laser integrating III-V active region with Si waveguide is an example of the high-potential application [3]. Recently, Luxtera, Inc. released an optical transceiver using a Si photonics technology based on monolithic optoelectronic devices manufactured in a low-cost CMOS process [4]. An optical isolator or circulator is as yet unrealized in Si-based waveguide, while it is required for high-speed transmission in optical fiber links to ensure the stable operation of active devices.

On the other hand, magneto-optical garnets such as yttrium iron garnet (YIG), that have a large magneto-optic effect and are transparent in the near-infrared region, are grown epitaxially on a garnet substrate. We have investigated a waveguide magneto-optical isolator using a Mach-Zehnder interferometer (MZI) with a directly bonded magneto-optic garnet

upper cladding layer [5,6]. As mentioned in Chapter 2, a use of a Si high-index-contrast waveguide enhances nonreciprocal phase shift in a magneto-optic garnet / Si / SiO₂ layered structure, which enables an ultracompact optical isolator with Si waveguides. Figure 3.1 shows an application of Si-based optical transceiver integrated with a magneto-optical isolator. Since a WDM scheme is promising technology for high capacity transmission, a wideband operation of the magneto-optical isolator which is proposed in Chapter 4 is suitable for this scheme. In other words, a high-performance optical transceiver can be realized on a Si platform owing to the magneto-optical isolator.

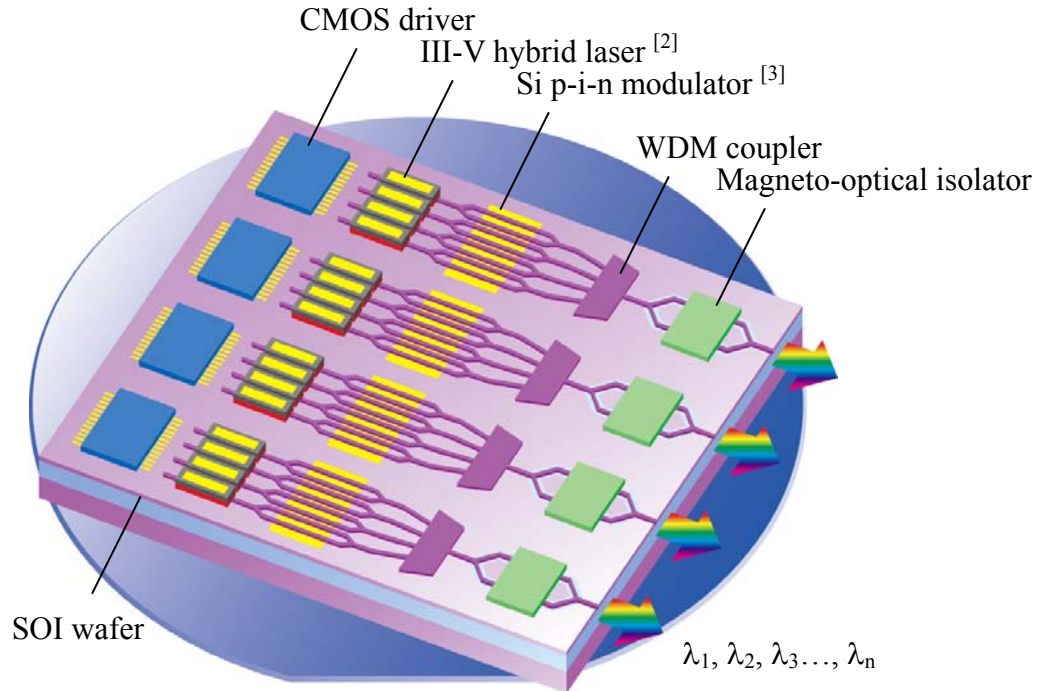


Fig. 3.1 Concept image of Si-based optical transceiver integrated with a magneto-optical isolator.

3.2 Device structure and design

The schematic drawing of the device structure is shown in Fig. 3.2. The principle of the isolator operation composed of a MZI configuration has been mentioned in Section 2.3. The nonreciprocal phase shifter is composed of a Ce:YIG / Si / SiO₂ -layered structure. The 3×2 multi-mode interference (MMI) coupler is employed as 3dB coupler in which a lightwave

from the center port of the 3 branches are divided into two waves with identical amplitude and phase through the two ports of the other 2 branches. And the MMI coupler provides interferences between the two waves from the 2 branches so that constructive and destructive interferences lead the lightwave to the center port and the side ports of the 3 branches, respectively.

In this section, all the designs are calculated with the refractive indices as shown in Table 3.1. First, the thickness of the Si guiding layer on a SOI wafer is determined. Figure 3.3 shows a nonreciprocal phase shift calculated by the perturbation theory with an electromagnetic field distribution given by the full-vector FEM as a function of the Si-thickness. The waveguide width and rib height are fixed at $2.0\mu\text{m}$ and $0.01\mu\text{m}$, respectively. The nonreciprocal phase shift is maximized at the Si-thickness of $\sim 0.20\mu\text{m}$ and the required propagation length is $213\mu\text{m}$ to obtain $\pm\pi/2$ phase differences by external magnetic fields in anti-parallel direction.

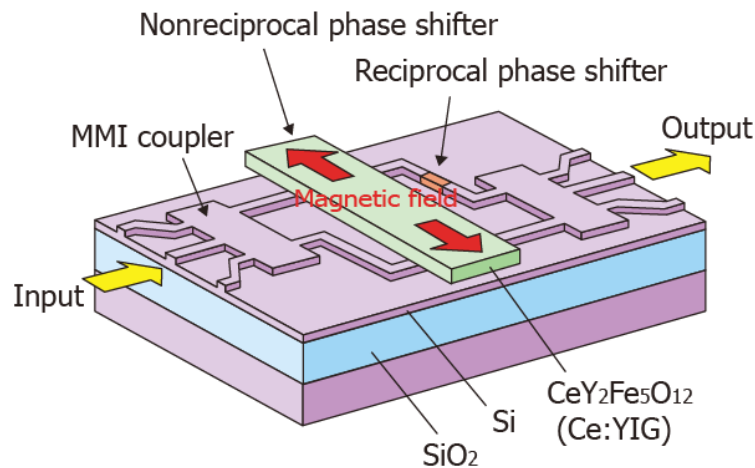


Fig. 3.2 Schematic drawing of the magneto-optical isolator with Si waveguide.

Table 3.1 Refractive indices at $\lambda = 1.55 \mu\text{m}$.

Material	Refractive index
Si	3.48
SiO ₂	1.44
air	1.0
Ce:YIG	2.20
SGGG	1.94
HfO ₂	1.98

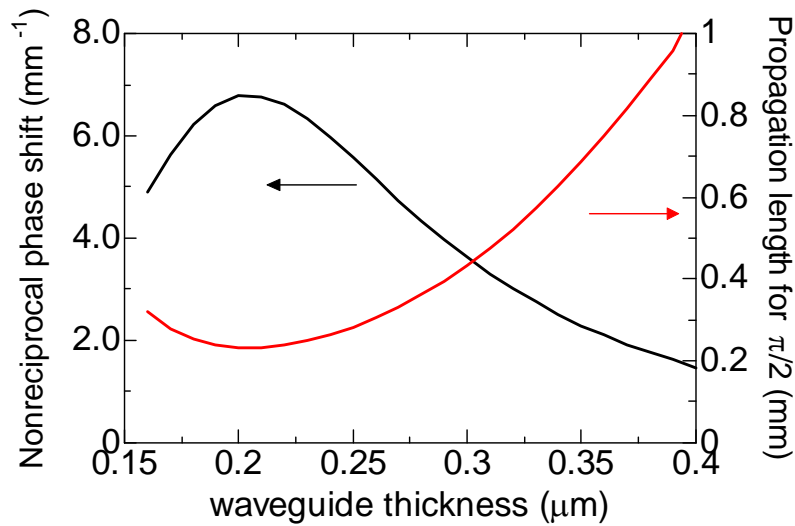
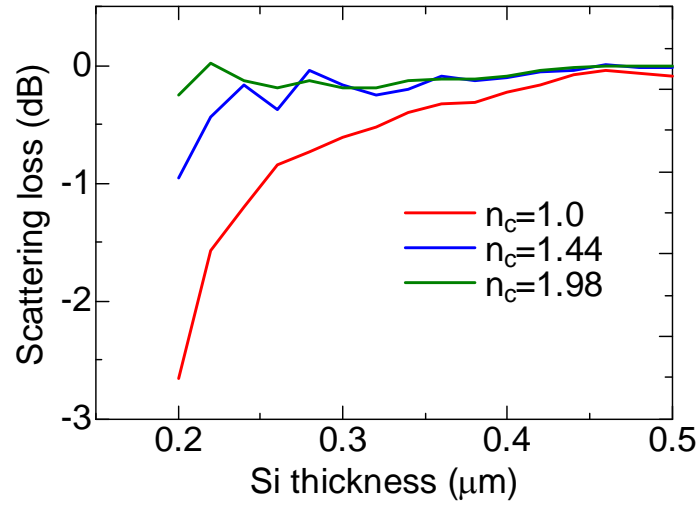


Fig. 3.3 Calculated nonreciprocal phase shift and the propagation length required for $\pi/2$ phase difference of Ce:YIG/Si/SiO₂ structure at $w = 2.0 \mu\text{m}$, $r = 0.01 \mu\text{m}$, and $\lambda = 1.55 \mu\text{m}$.

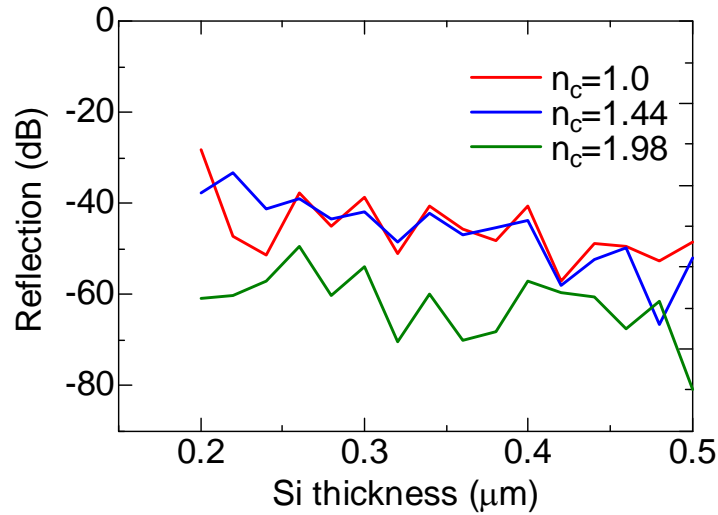
However, there are some problems when the thickness is small. One is a leakage loss into the Si substrate through the SiO₂ lower cladding layer due to large evanescent fields in this layer. For example, the thickness of the SiO₂ layer required for loss-free guiding of TM fundamental mode is more than $2.0 \mu\text{m}$ as the $0.20\text{-}\mu\text{m}$ -thick Si layer while $1.0 \mu\text{m}$ is sufficient for the case of the $0.30\text{-}\mu\text{m}$ -thick Si layer. The other problems are a scattering loss

and a reflection at the boundary between the different upper cladding regions fabricated by a direct bonding technique. Figures 3.4 (a) and 3.5 (a) show the decrease in transmittance due to the scattering at a boundary with different upper cladding regions on a Si waveguide calculated by a bi-directional finite difference (FD) BPM in a 2-D (x - z) structure [7] and a bi-directional optical propagation analysis based on eigenmode expansion method [8]. The material of the upper cladding layers are assumed to be air, SiO₂, and HfO₂ against Ce:YIG region. The decrease in transmittance is 2.6 dB for a 0.20- μ m-thick Si guiding layer at a boundary between Ce:YIG and air cladding regions. Also, the reflection coming back to the input is calculated by these methods as shown in Figs. 3.4 (b) and 3.5 (b). The reflection is -27 dB for a 0.20- μ m-thick Si guiding layer. It is possible to prevent the reflections from returning into the input port by adjusting the phase difference between the reflections in two arms to be antiphase. The scattering loss and reflection can be reduced as the thickness of Si increases or the refractive index of the upper cladding layer is close to that of Ce:YIG. However, the required length of the nonreciprocal phase shifter is long for a thicker Si layer as shown in Fig. 3.3. Also, the waveguide dimensions become large for lower index contrast between Si and the cladding layer. Consequently, the thickness of Si guiding layer is to be determined taking into account the trade-off between the scattering loss and the device size.

Hence, we consider two designs of the isolator. One is a low-loss design for a test fabrication with 2.0- μ m-wide and 0.01- μ m-height rib waveguide on 0.30- μ m-thick Si layer. The other is for an ultracompact design with 0.6- μ m-wide channel waveguide on 0.22- μ m-thick Si layer. The propagation lengths of the nonreciprocal phase shifter (L_{NPS}) and reciprocal phase shifter (L_{RPS}) are designed by mode solving based on FEM and a perturbation theory as described in Section 2.3. The MMI coupler is designed by 3-D FD-BPM [7]. Figure 3.6 shows the configuration and its design parameters. Table 3.2 shows two designs of the magneto-optical isolator. A 1 \times 2 MMI coupler is designed for the ultracompact design. The total length of 364 μ m is the world's smallest among optical isolators ever-reported.

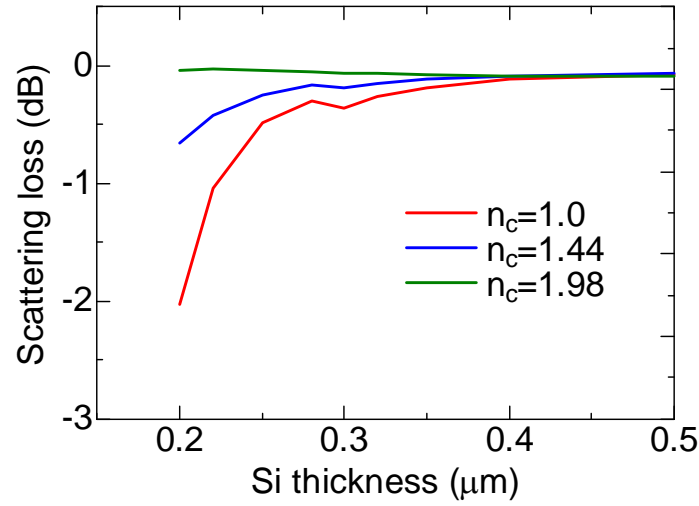


(a)

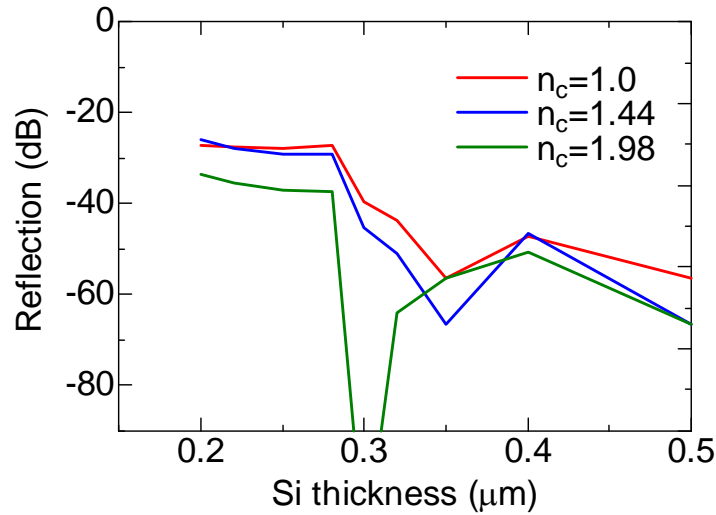


(b)

Fig. 3.4 (a) Decrease in transmittance due to scattering and (b) reflection at a boundary between different upper cladding layers on a Si waveguide calculated by a bi-directional BPM. One side of the upper cladding layer is Ce:YIG with the refractive index of 2.20. Simulation grid sizes are $\Delta x = 0.01 \mu\text{m}$ and $\Delta z = 0.02 \mu\text{m}$ and the Padé order is (2,2).



(a)



(b)

Fig. 3.5 (a) Decrease in transmittance due to scattering and (b) reflection at a boundary between different upper cladding layers on a Si waveguide calculated by a bi-directional optical propagation analysis based on eigenmode expansion method. One region has upper and side cladding layers of 2.20 and 1.0, respectively, and the other region has covered layer of modified index. The width of Si channel waveguide is set at 2.0 μm.

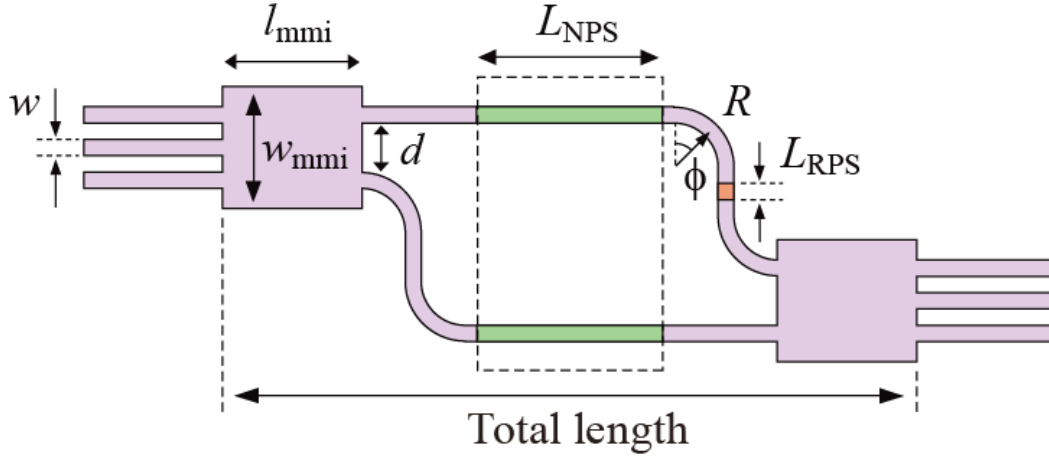


Fig. 3.6 Design of a MMI coupler on SOI wafer.

Table 3.2 Two sets of design parameters of the magneto-optical isolator with Si waveguides.

(unit: μm)		
	Low-loss design	Ultracompact design
Cover material	Air	SiO_2
Width (w)	2.0	0.60
Height (h)	0.30	0.22
Rib height (r)	0.01	(channel)
L_{NPS} for $\pm\pi/2$	401	298
L_{RPS} for $+\pi/2$	0.152	0.170
MMI width (w_{mmi})	15.0	4.0
MMI length (l_{mmi})	210	22
Arm distance (d)	6.0	1.6
Bending (R, ϕ)	$\sim 500, 60^\circ$	10, 90°
Total length	~ 3000	364

3.3 Fabrication of Si waveguide

Figure 3.7 shows a fabrication process of the Si waveguide. We use a Unibond SOI wafer manufactured by wafer bonding and splitting techniques with a hydrogen-implantation called “Smart-Cut®” proposed by Bruehl [9]. The SOI wafer is first cleaned with ethanol, acetone, and isopropanol. The native oxide on Si surface is not removed by hydrofluoric acid in this stage so as to protect the wafer surface until a direct bonding process. After coating 300-nm-thick electron-beam resist ZEP-520A on the sample surface by a spin coater with 6000 rpm for 60 sec, it is baked at 170 °C for 15 min. The waveguide patterns are exposed by electron-beam lithography with accelerating voltage of 50 kV and are developed with a mixture of methyl isobutyl ketone and isopropanol (1:1) for 2 min. The patterns are transferred to an e-beam deposited Cr mask, which is then lifted off with dimethylformamide. The rib or channel waveguide is formed on Si surface by reactive ion etching (RIE) in a CHF₃:O₂ (15:1) plasma with a 50-W radio frequency (RF) power. The Cr mask is stripped off with hydrochloric acid at ~120 °C. Finally, the ends of the Si waveguide are obtained by cleaving the sample at a notch formed by dicing-saw.

Figure 3.8 shows scanning electron microscope (SEM) images of the fabricated 0.20- μ m-thick and 0.60- μ m-wide Si-wire waveguides. The roughness of the sidewall is about 10 nm. The bending radius and angle are 2.5 μ m and 90 degree. The 2.0- μ m-wide and 3.0- μ m-length MMI coupler is well fabricated.

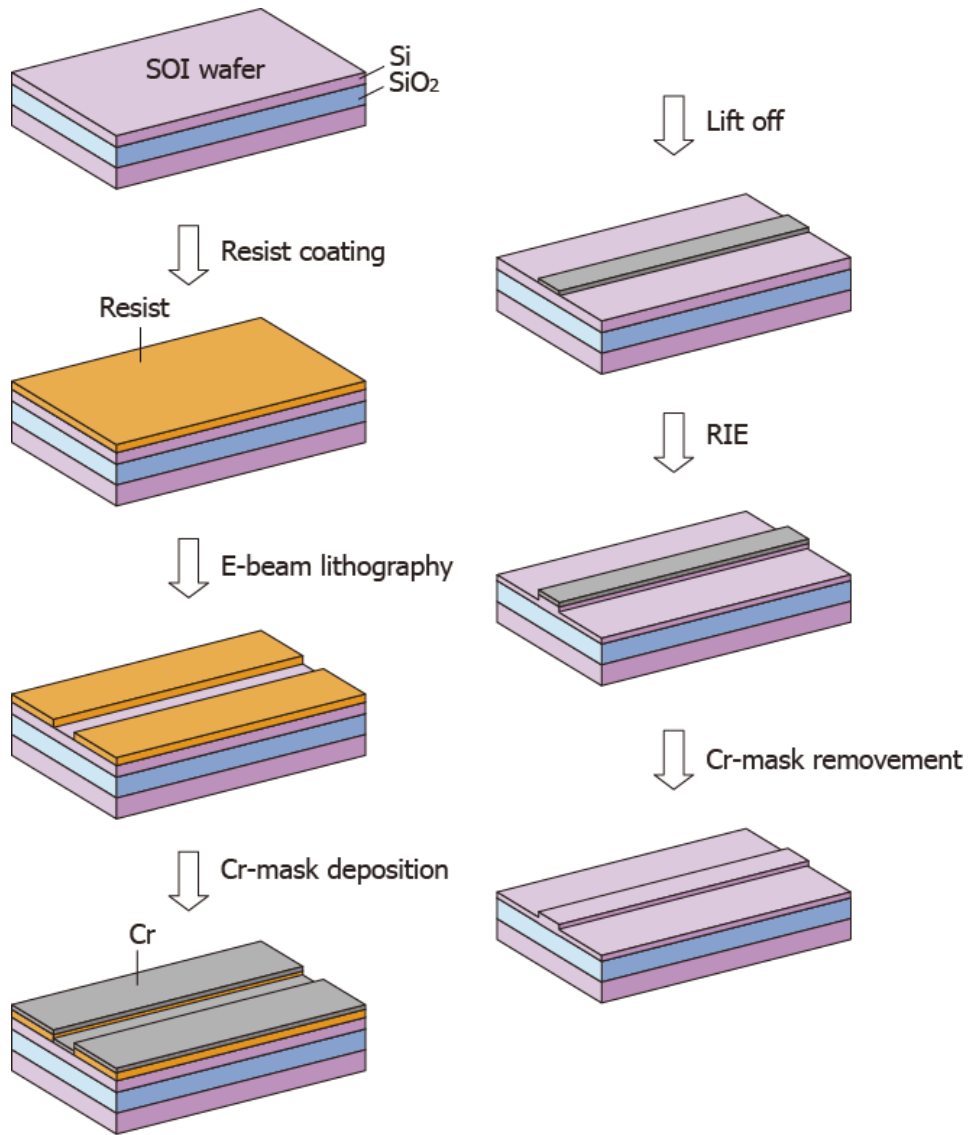


Fig. 3.7 Fabrication process of Si waveguide.

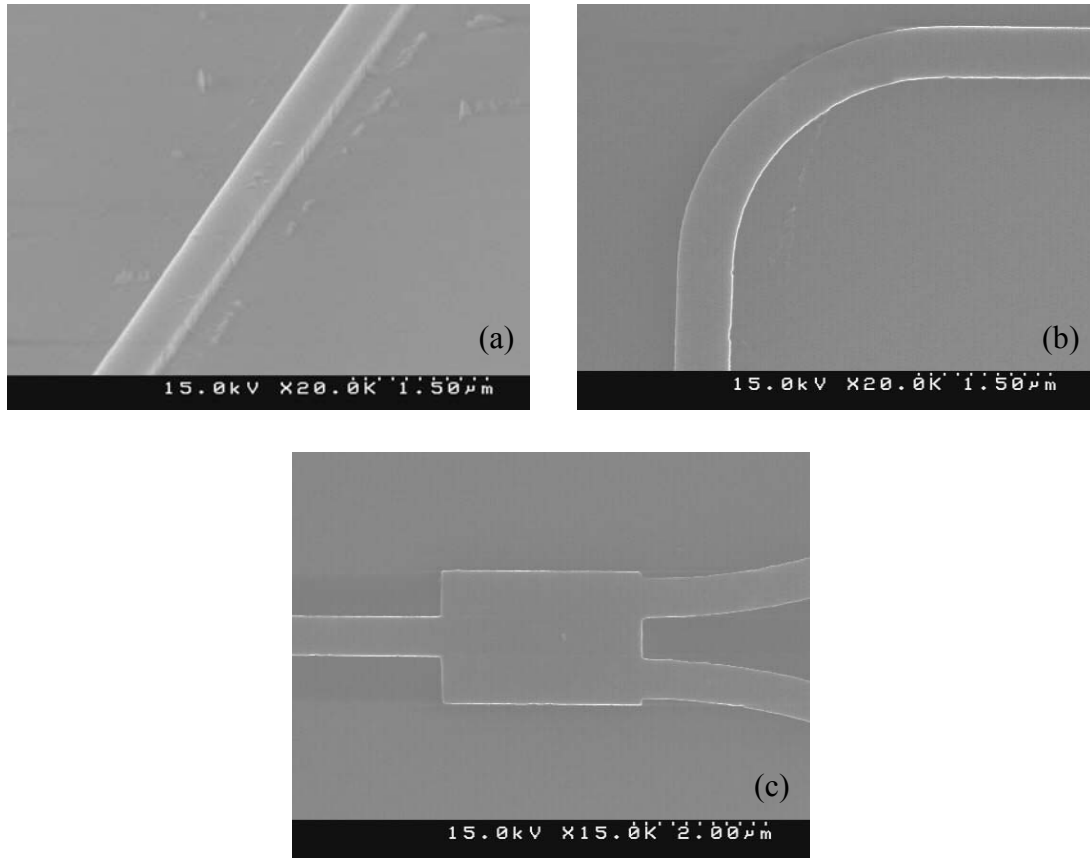


Fig. 3.8 Fabricated Si-wire waveguides. (a)Straight waveguide, (b)bending waveguide, and (c)MMI coupler.

Figure 3.9 shows measurement results of the propagation loss of 0.2- μm -thick Si channel waveguides for TM mode propagation. The losses shown in (a) and (b) are measured for a sample with the upper cladding of air and that after 0.8- μm -thick SiO_2 deposition, respectively. The transmitted power of the Si waveguides with several widths through fiber to fiber alignment is measured by optical power meter at $\lambda=1.55 \mu\text{m}$. The propagation loss except the coupling loss between fiber/sample is estimated from the gradient as a function of propagation length, which is known as a “cut-back” method. The propagation loss is about 3.7 – 4.0 dB/mm independent of the waveguide width. The sidewall roughness $\sim 10 \text{ nm}$ of Si waveguide dominates the propagation loss. The coupling loss decreases after covering SiO_2 cladding layer.

In the same way, the propagation loss of 0.3- μm -thick and 2.0- μm -wide Si rib waveguides with several rib heights are measured as shown in Fig. 3.10. The propagation loss is 0.63

dB/mm for the rib height of 10 nm.

Figure 3.11 shows the measured bend loss of curved section for 0.2- μm -thick and 0.6- μm -wide Si-wire waveguide with several bending radii. The loss of 90-degree bend with 2.5- μm -radius is ~ 4.9 dB that is dominated by the sidewall roughness. It becomes negligible small when the bending radius is more than 20 μm . Figure 3.12 shows the measured excess loss of branching characteristic of the fabricated MMI coupler. 0.2- μm -thick and 0.6- μm -wide Si-wire waveguides are connected to the 2.0- μm -wide multimode section. The divided powers of around -3 dB, almost identical to each port, are obtained at the coupler length of 3.2 μm .

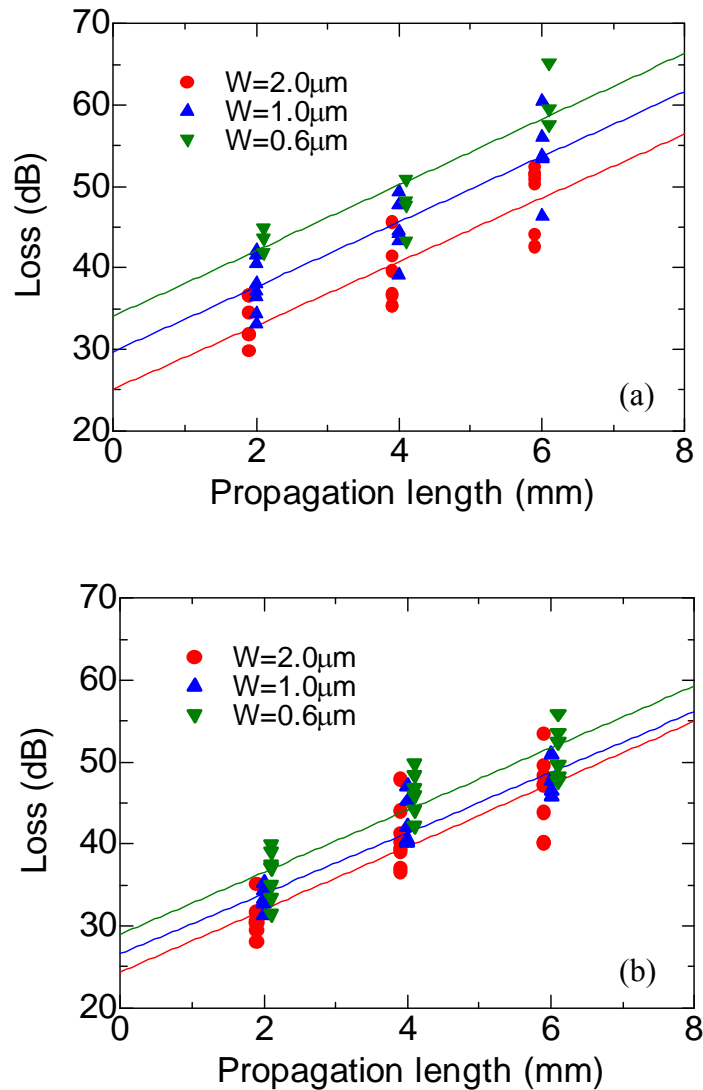


Fig. 3.9 Propagation loss of 0.2- μm -thick Si channel waveguide with (a) air and (b) SiO_2 upper cladding materials for TM mode, at $\lambda = 1.55\mu\text{m}$.

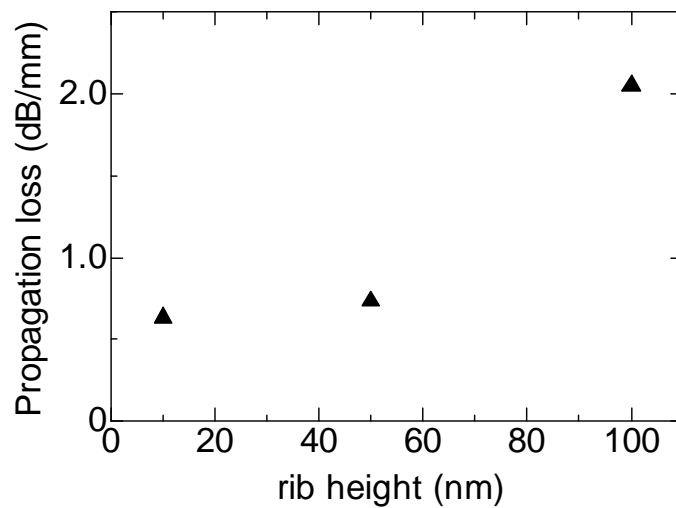


Fig. 3.10 Propagation loss of 0.3- μm -thick and 2.0- μm -wide Si rib waveguides with several rib heights for TM mode, at $\lambda = 1.55 \mu\text{m}$.

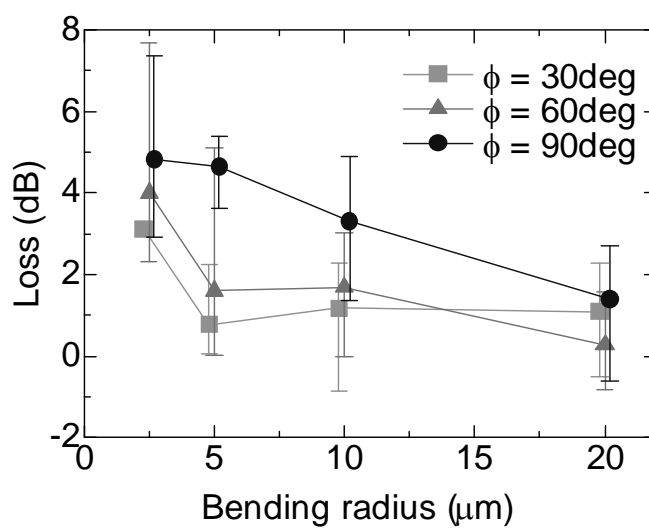


Fig. 3.11 Bend loss of 0.2- μm -thick and 0.6- μm -wide Si-wire waveguide for TM mode, at $\lambda = 1.55 \mu\text{m}$.

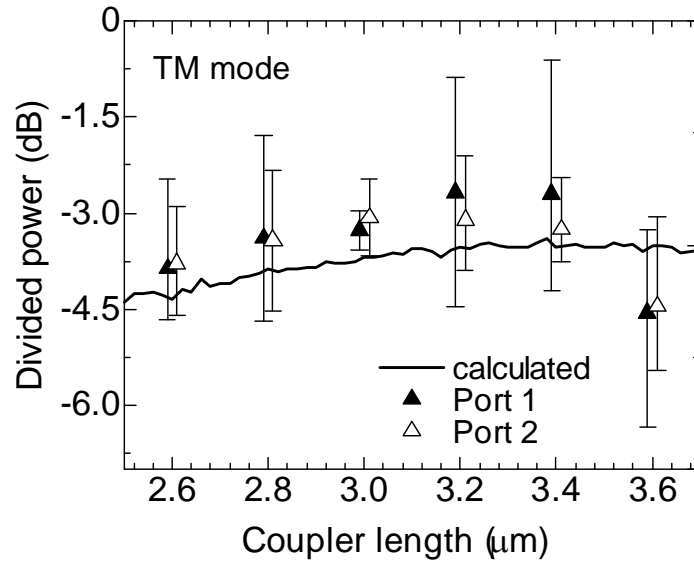


Fig. 3.12 Excess loss of branching characteristic of the fabricated MMI coupler for TM mode, at $\lambda = 1.55 \mu\text{m}$. The solid line is calculated by 3-D BPM.

A spot-size converter in the Si waveguide is investigated to improve the coupling efficiency between fiber and waveguide. The coupling loss is induced by the mismatch in the field distribution between fiber and waveguide. The width and height of Si channel waveguide are set at $0.60 \mu\text{m}$ and $0.20 \mu\text{m}$, respectively. The waveguide is covered with $\sim 1.0\text{-}\mu\text{m}$ -thick SiO_2 cladding layer by sputter deposition. The 0.2-mm -long waveguide from the end facet is changed its width and is connected to the normal waveguide by a 0.3-mm -long tapered region. First, the coupling efficiency between a waveguide and a fiber through air gap of $10 \mu\text{m}$ is calculated by 3-D BPM. The coupling loss is calculated by normalizing the fiber mode power in a fiber with the launched power in a waveguide. Figure 3.13 (a) shows the doubled coupling loss assuming the two connections. Next, the spot-size converter is fabricated on a $0.20\text{-}\mu\text{m}$ -thick SOI waveguide with several widths of waveguide end. Figure 3.13 (b) shows the measured coupling loss through two fiber/waveguide connections that is obtained from transmitted power except the propagation loss. The calculated and measured coupling losses show similar behavior though they have different peaks. For the channel waveguide, the coupling loss is the smallest at the width of $0.20 \mu\text{m}$ in

the measurement while it is the smallest at the width of $0.06\ \mu\text{m}$ in the calculation. This is due to that the fabricated waveguide has large scattering loss at the sidewall which increases the propagation loss more than the improvement of coupling efficiency at the narrower width. The coupling loss is reduced about 10 dB for $0.20\text{-}\mu\text{m}$ -width of the end waveguide compared with $0.60\text{-}\mu\text{m}$ -width of the waveguide without any taper. On the other hand, for a rib waveguide, such a down tapered spot-size converter is not effective as the field distribution at the narrower width is confined in the slab region of the Si layer.

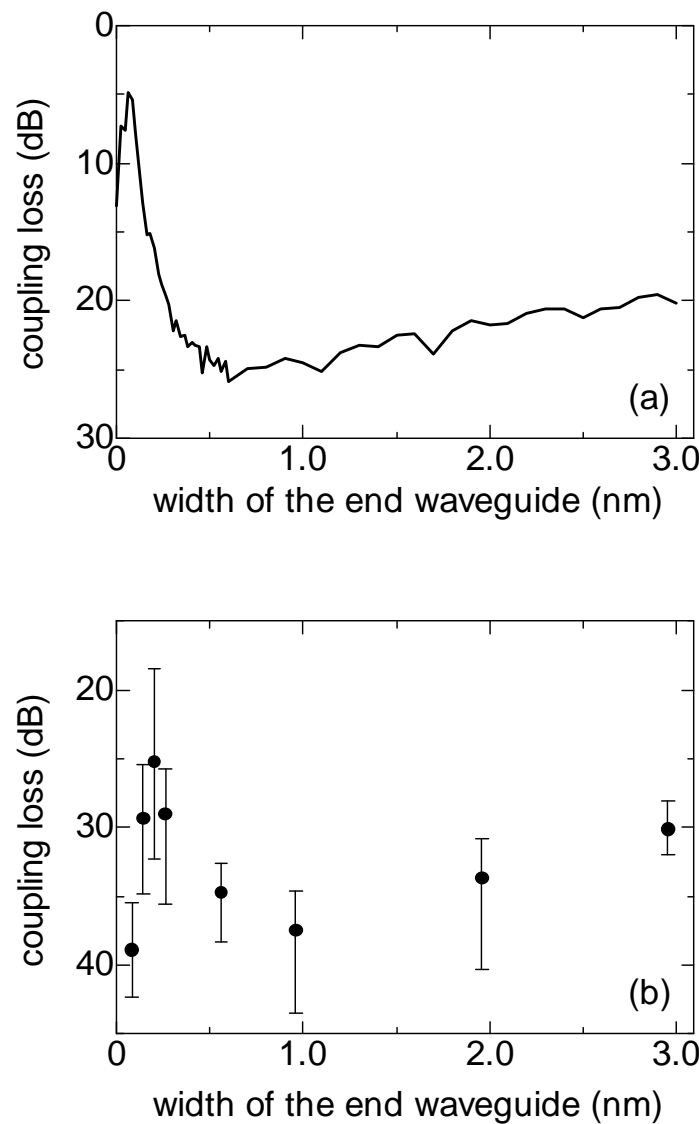


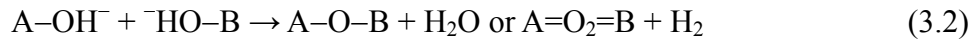
Fig. 3.13 (a) Calculation and (b) measurement results of coupling loss between an optical fiber to Si channel waveguide. The simulation grid sizes are $\Delta x = 0.05\ \mu\text{m}$, $\Delta y = 0.02\ \mu\text{m}$, and $\Delta z = 0.02\ \mu\text{m}$.

3.4 Direct bonding between Si and Ce:YIG

A wafer bonding is key technique to realize integrated optical devices since III-V compound semiconductor, crystalline Si, and magneto-optic garnet can not be epitaxially grown on each other due to the large lattice mismatch. Although indirect bonding technologies such as “adhesive bonding” and “eutectic bonding” are easy to use, the glue layer in the order of micron between the wafers is too thick to obtain an efficient magneto-optic effect. A conventional wafer bonding technique is classified in “hydrophobic” or “hydrophilic” bonding where hydrides or hydroxyl groups contribute to the bonding interface, respectively. Covalent bondings are formed by desorption of these chemisorbed molecules in high-temperature annealing at 800 – 1000 °C. These bonding procedures between two arbitral materials A and B are expressed as



for hydrophobic and



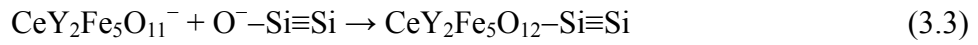
for hydrophilic treatments. Then, a difference in thermal expansion between dissimilar materials results in high mechanical stress at the interface. It can make the wafers crack and completely debond. Therefore, a number of effort and research in wafer bonding is focused on developing low-temperature procedures [10-14]. Typically, bonding strength increases proportional to the temperature of thermal treatment. In order to achieve strong bonding with low-temperature annealing procedures, the surface treatment of bonded wafers is very important.

3.4.1 Surface activated bonding with oxygen plasma treatment

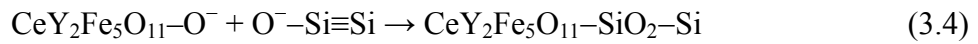
In this study, a surface activated bonding with oxygen plasma treatment [15,16] is utilized for bonding between Si and CeY₂Fe₅O₁₂ (Ce:YIG) grown on a (GdCa)₃(GaMgZr)₅O₁₂ (SGGG) substrate by a RF sputtering epitaxy. Two wafers activated by oxygen plasma treatment are bonded together and annealed at low temperature *in situ* the vacuum chamber.

The oxygen plasma is considered to affect a wafer surface physically and chemically at the same time. Physical effect is removal of contaminants on a surface by oxygen ions

accelerated by self-bias voltage of the RF plasma. It is well known that oxygen plasma treatment is very efficient in removing hydrocarbon and water related species. Chemical effect is a formation of oxidized or ionized thin layer by the ion “bombardment” that is indicated by observing a hydrophilic surface after oxygen plasma exposure. In Ref. [15], ultrathin oxide layer (< 5 nm) is observed at the bonding interface between Si and InP where SiO₂ is formed rather than InP-oxide. In the case of bonding between Si and Ce:YIG, we speculate that Si is oxidized by oxygen plasma to be O⁻-Si, while oxide atom terminating the crystal lattice of Ce:YIG is sputtered or ionized by oxygen plasma to be CeY₂Fe₅O₁₁⁻ or CeY₂Fe₅O₁₁-O⁻. It is plausible that a direct bonding is achieved as



or



by sharing the oxygen atoms in the intermediate oxide layer which is amorphous of Ce:YIG rich or SiO₂ rich in each case. We will discuss about the influence of the ultrathin interlayer on isolator design in Section 3.5.

There are two advantages to bond wafers *in situ* vacuum chamber without exposing them to ambient air after oxygen plasma treatment. One is enhancement of bonding strength by preventing dusts or molecules in air trapping at the activated surfaces which result in voids or failure of bonding [14]. In addition, the low ambient pressure enhances the bonding speed by efficient removal of gas molecules such as O₂ generating or remaining at the interface [17]. Whereas, Suga *et al.* have showed that strong bonding is obtained when two wafers are contacted in air after oxygen plasma activation owing to water molecules absorbed on the activated surfaces [16]. The author presumes that the oxygen activation and hydrophilic bonding contribute simultaneously in that case even though it is uncertain why the bonding strength is enhanced.

3.4.2 Experiment

We prepare an experimental setup for surface activated bonding with oxygen plasma treatment followed by *in situ* annealing and pressing as shown in Fig. 3.14. Si and Ce:YIG

wafers are cleaned elaborately with organic solutions and RCA cleaning for Si [18] as the procedures shown in Table 3.3, where the deionized (DI) water has the electrical resistivity of $> 18.2 \text{ M}\Omega\cdot\text{cm}$ refined by ultrapure water system. The surface roughness (RMS) of the two wafers is below 1 nm. When single particles or protrusions are much higher than this value, they will create voids and result in nonuniform bonding region. After placing wafers on the sample stage, the chamber is vacuumed to $\sim 1 \times 10^{-5} \text{ Pa}$. The plasma is generated with a RF system of 13.56 MHz between a $3 \times 4 \text{ cm}^2$ electrode and the chamber. The wafers are exposed to oxygen plasma with 100-W RF power for 30-s in the chamber pressure of 4.0 Pa, because moderate plasma treatment gives smooth surfaces and higher surface energy together with efficient removal of contaminants on the surfaces [15]. After that, the activated surfaces are attached to each other immediately by using a manipulator *in situ* the vacuum at $\sim 10^{-5} \text{ Pa}$. The samples loaded to the press position together with the sample stage are pressed with the applied pressure of $\sim 5 \text{ MPa}$. Temperature is then increased for annealing at $150 - 400 \text{ }^\circ\text{C}$ for 30 min and kept it for 1 hour with the pressure. To mitigate the stress induced by the difference in thermal expansions, the temperature is decreased gradually at a rate of $-50 \text{ }^\circ\text{C}/\text{hour}$.

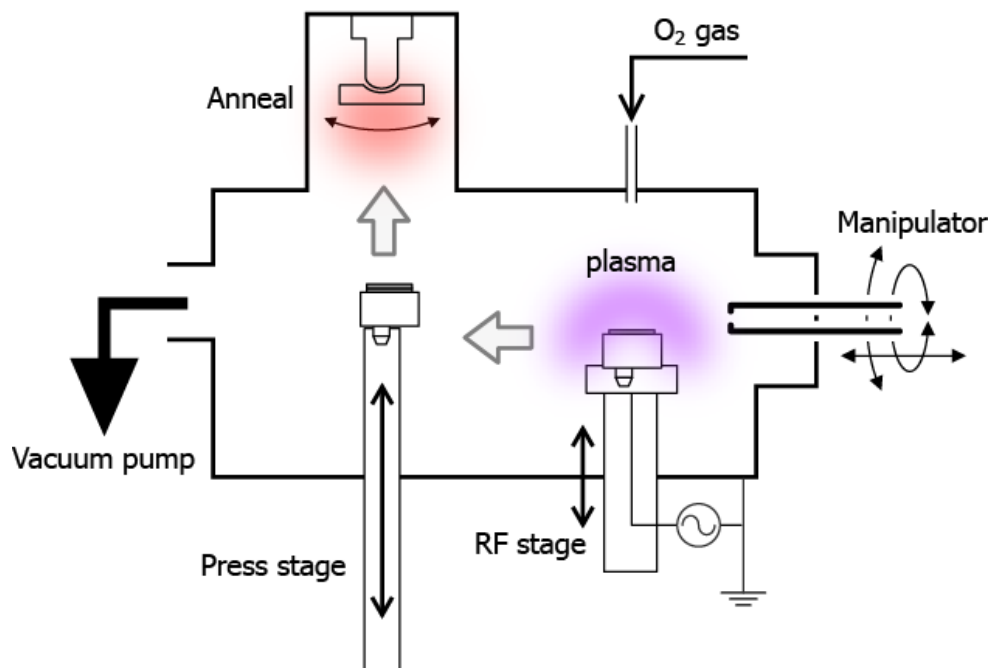


Fig. 3.14 Experimental setup for surface activated bonding with oxygen plasma treatment.

Table 3.3 Cleaning procedure before surface activated bonding.

Si (SOI)			Ce:YIG		
Solution	°C	min	Solution	°C	min
Ethanol	120	5	Ethanol	120	5
(Ultrasonic 100kHz)	R.T.	3	(Ultrasonic 100kHz)	R.T.	3
Ethanol	120	5	Ethanol	120	5
Acetone	100	5	Acetone	100	5
(Ultrasonic 100kHz)	R.T.	3	(Ultrasonic 100kHz)	R.T.	3
Acetone	100	5	Acetone	100	5
HF:H ₂ O (1:19)	R.T.	40s	Ethanol	120	5
DI water	R.T.	30s	(Ultrasonic 100kHz)	R.T.	3
NH ₄ OH:H ₂ O ₂ :H ₂ O (1:1:5)	90~100	10	Ethanol	120	5
DI water	R.T.	1	Acetone	100	5
HCl:H ₂ O ₂ :H ₂ O (1:1:5)	90~100	10			
DI water	R.T.	1			
HF:H ₂ O (1:19)	R.T.	30s			
DI water	R.T.	10s			

Figure 3.15 shows photo images of the sample of Ce:YIG bonded onto Si and SOI flat wafers with the annealing temperature at 400 °C. The bonded region and surrounding Newton ring are observed since a thin Ce:YIG layer and an SGGG substrate are transparent at visible light. Table 3.4 shows the experimental results of the bonding at several annealing temperatures. Direct bonding is obtained at annealing temperature higher than 200 °C. The wafers bonded at 300 °C are debonded as time goes by. Cracks are observed in the Ce:YIG wafer with the annealing at 350 °C and higher, while the bonding remains in the cracked regions. The bonding strength and the thermal stress increase as the annealing temperature independently to each other. We notice that debond occurs when the thermal stress becomes more than the bonding strength, and cracks occurs when both exceed the stiffness limit of the

Ce:YIG wafer since Si is mechanically a stronger material. The thermal shear stress τ_{\max} at the edge of the bonded interface can be estimated by the following equation [19]

$$\tau_{\max} = \frac{\Delta\alpha\Delta T}{\sqrt{\lambda k}}, \quad (3.5)$$

$$\lambda \equiv \left[\frac{1-\nu_1^2}{E_1 d_1} + \frac{1-\nu_2^2}{E_2 d_2} + \frac{3(d_1+d_2)(1-\nu_1^2)(1-\nu_2^2)}{E_1 d_1^3(1-\nu_2^2) + E_2 d_2^3(1-\nu_1^2)} \right], \quad (3.6)$$

$$k \equiv \frac{2d_1(1+\nu_1)}{3E_1} + \frac{2d_2(1+\nu_2)}{3E_2}, \quad (3.7)$$

where $\Delta\alpha$ is the difference in thermal expansion coefficients between the two bonded materials, ΔT is the temperature change, d_1 and d_2 are the wafer thickness, E_1 and E_2 are the Young's moduli, and ν_1 and ν_2 are the Poisson ratios. The τ_{\max} is calculated to be 2.44 kg/cm²/K or 3.37 kg/cm²/K for the interface between Si ($\alpha = 2.6 \times 10^{-6}$ /K, $d = 0.6$ mm, $E = 1.30 \times 10^{13}$ dyn/cm², $\nu = 0.28$) and Ce:YIG ($\alpha = 8.0 \times 10^{-6}$ /K, $d = 0.5$ mm, $E = 2.0 \times 10^{12}$ dyn/cm², $\nu = 0.29$) or between Si and GGG ($\alpha = 9.18 \times 10^{-6}$ /K, $d = 0.5$ mm, $E = 2.74 \times 10^{12}$ dyn/cm², $\nu = 0.281$), respectively. This can be reduced by using small chip of bonded wafer as well as annealing at low-temperature.

Figure 3.16 shows a SEM image of the bonding interface between Ce:YIG and Si rib waveguide bonded with annealing at 400 °C.

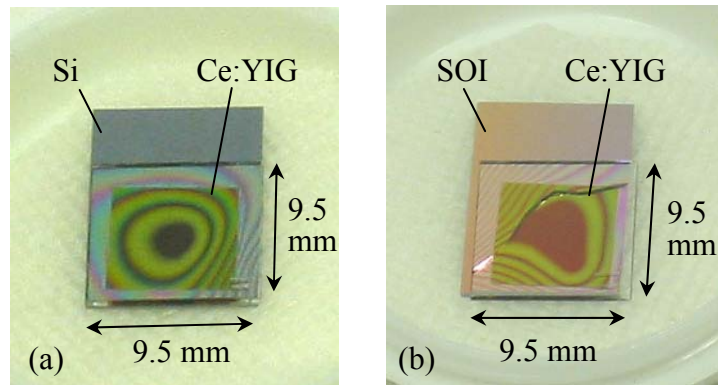


Fig. 3.15 Photo images of bonded sample between (a)Si and Ce:YIG, (b)SOI and Ce:YIG with the annealing temperature at 400 °C.

Table 3.4 Experimental results of the surface activated bonding with Si and Ce:YIG using oxygen plasma of 100-W RF power for 30s, pressed with ~5 MPa.

Temperature (°C)	Bonding	Crack
150	×	No
200	○	No
250	○	No
300	○	No → debonded as time goes by
350	○	Yes
400	○	Yes

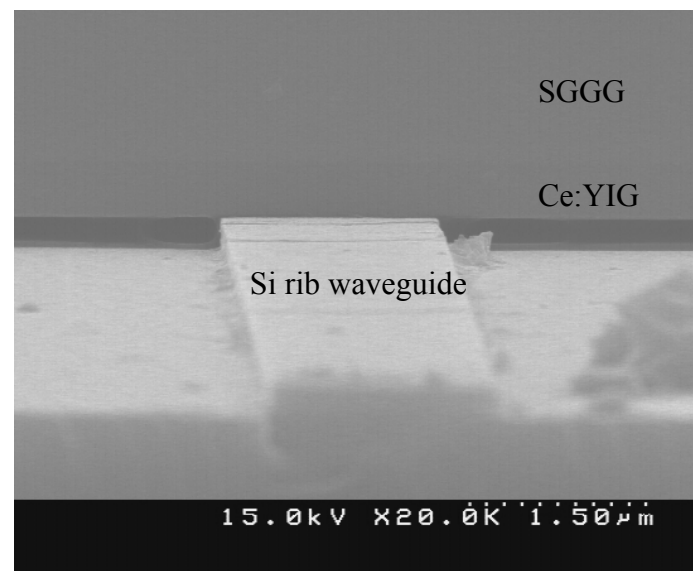


Fig. 3.16 SEM image of the bonding interface between Ce:YIG and Si rib waveguide.

3.5 Characterization

3.5.1 Isolator operation

A magneto-optical isolator with Si waveguides is fabricated. The MZI of the low-loss design shown in Table 3.2 is fabricated with Si rib waveguides on a SOI wafer with a 0.3- μm -thick Si top layer and a 1.0- μm -thick SiO_2 layer. Ce:YIG film is grown on a garnet substrate (SGGG) with the thickness of 0.5 μm , which is sufficient to offer a nonreciprocal phase shift without influence of the non-magneto-optic garnet substrate. Figure 3.17 shows the nonreciprocal phase shift as a function of the Ce:YIG thickness calculated by solving eigenvalue equation with four-layered structure as described in Section 2.2.1.

Figure 3.18 shows the photo image of the fabricated sample bonded with Ce:YIG by the surface activated bonding with oxygen plasma treatment and annealing at 250 °C for one hour with a pressure of 5 MPa. Broad contact areas are formed on Si surface 50- μm away from the rib waveguide to provide a sufficient bonding area. The total length of the waveguide is 4.0 mm, which includes 4.0- μm -wide taper waveguides at input and output ends to increase the coupling efficiency into connecting fibers. The length of the bonded garnet chip is 2.0 mm, where the nonreciprocal phase shifter is composed by parallel waveguides with the propagation length of 0.40 mm. The distance of the interferometer arms is to be 0.50 mm, sufficient to apply an external magnetic field in anti-parallel directions.

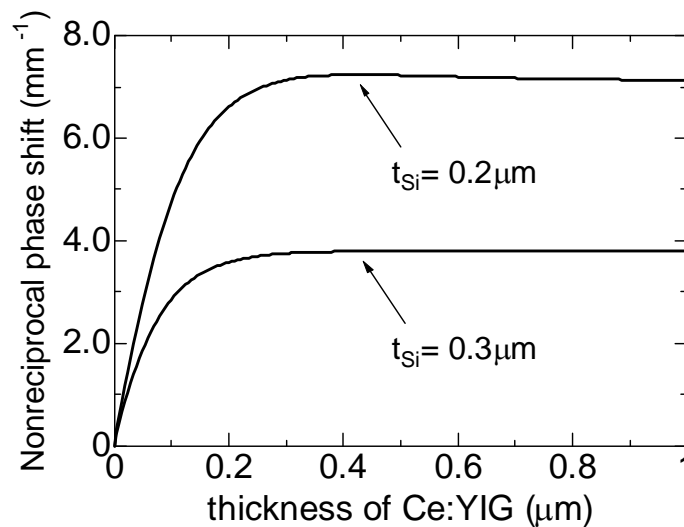


Fig. 3.17 Calculated nonreciprocal phase shift in a SGGG/Ce:YIG/Si/SiO₂ -layered structure as a function of Ce:YIG thickness by solving eigenvalue equation.

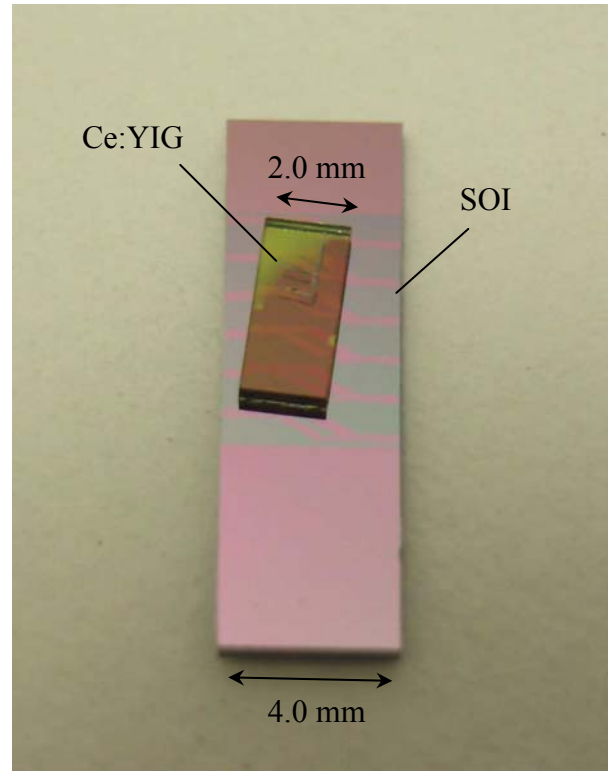


Fig. 3.18 Photo image of the fabricated sample.

The optical setup for the measurement of isolator operation is shown in Fig. 3.19. An amplified spontaneous-emission (ASE) diode having an optical gain in the wavelength range of $1.53 - 1.565 \mu\text{m}$, is used as a light source. This light is polarized to TM mode and is launched into the sample under test through a polarization maintaining fiber (PMF). An optical switch determines the optical path along clockwise (CW) or counter-clockwise (CCW) direction through the sample/fiber test setup. The output light transmitted through the sample is coupled to another PMF to measure the transmittance with a spectrum analyzer. An external magnetic field is applied to the interferometer arms in anti-parallel direction by using a pair of small permanent magnets with three reversed poles. The external magnetic field required to saturate the magnetization of Ce:YIG in-plane is 20 Oe.

The experimental characterizations of the isolator are shown in Fig. 3.20 and Fig. 3.21 that correspond to different isolators of fifth and fourth waveguides from the top on the sample shown in Fig. 3.18. The dashed lines show the wavelength dependence of the

transmission spectra for light propagating in CW and CCW directions without applying external magnetic fields. In this case, the symmetry of the expected two optical paths in the measurement setup is essentially confirmed. The small power difference in the transmittance between CW and CCW directions is ascribed to a difference in the performance of MMI couplers, since the left-hand and right-hand side MMI couples have different upper cladding layer, as shown in Fig. 3.18. Next, a permanent magnet is placed on the top surface of the sample to apply external magnetic fields in anti-parallel directions to the two MZI arms. In this case, it is observed that the transmission spectra differ significantly depending on the propagation direction as shown by the solid lines in Fig. 3.20 (a) and Fig. 3.21 (a). When we exchange the permanent magnet for another one with reversed poles, i.e., S-N-S for N-S-N, the directions of phase shift are also reversed as shown in Fig. 3.20 (b) and Fig. 3.21 (b). That is the change in transmission spectra by reversing the magnetic field direction corresponds to that given by reversing the propagation direction. It can be concluded that the direction-dependent transmittance is due to the nonreciprocal phase shift. The difference in the transmittance between CW and CCW directions corresponds to the isolation ratio of the magneto-optical isolator. The maximum isolation ratios of 21 dB at $\lambda = 1559$ nm and 17 dB at $\lambda = 1546$ nm are obtained in the measured transmittance of Fig. 3.20 and Fig. 3.21, respectively.

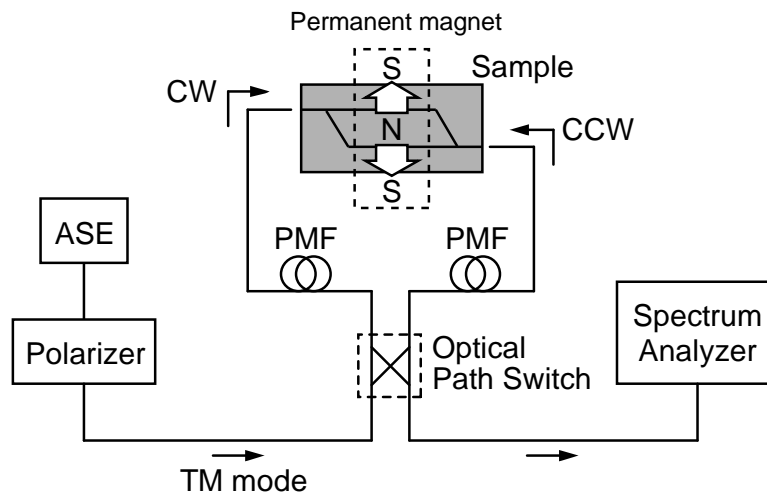
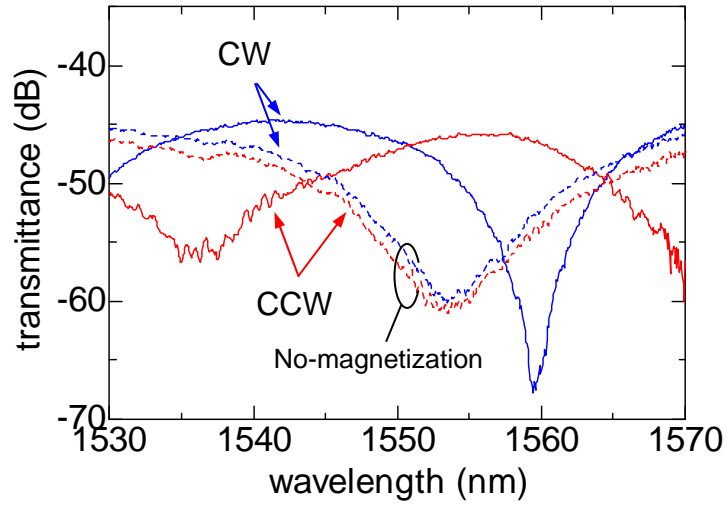
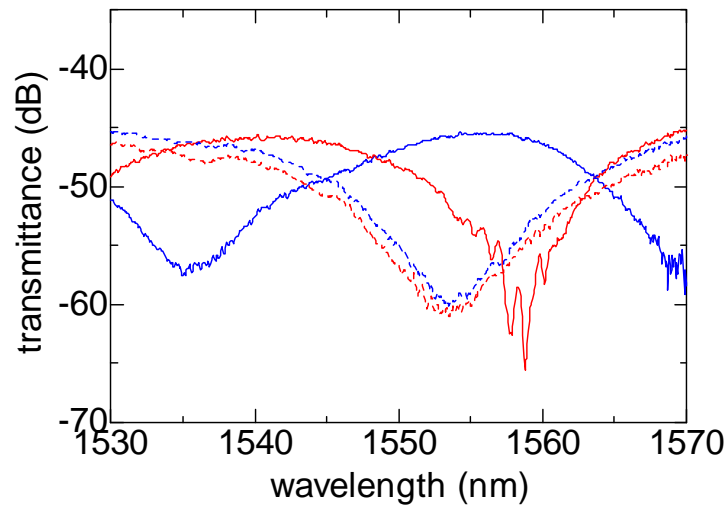


Fig. 3.19 Setup for the measurement of isolator operation.

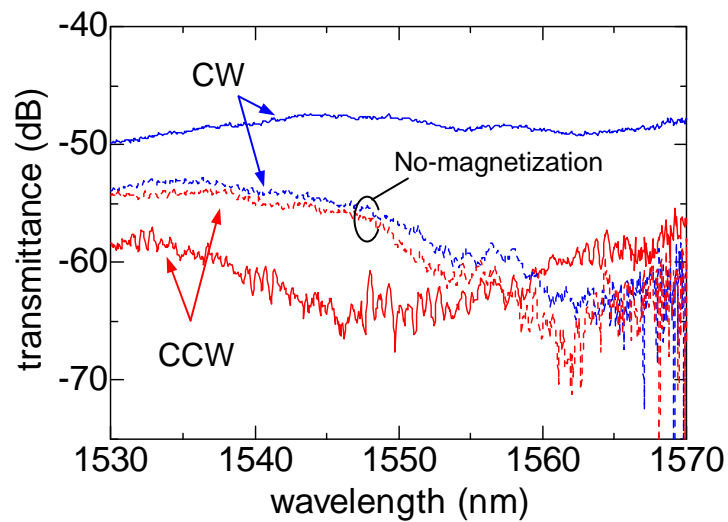


(a)

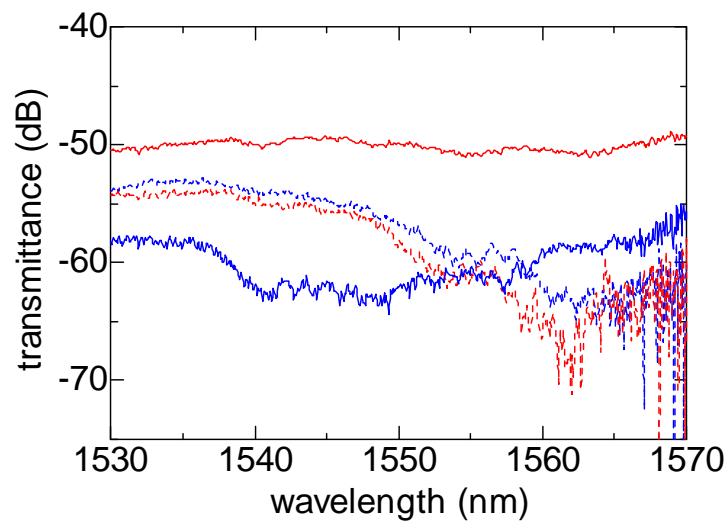


(b)

Fig. 3.20 Measured transmission spectra for different propagation directions. Light transmits the sample from left to right at clockwise (CW) direction and from right to left at counter-clockwise (CCW) direction. Solid lines show the transmission spectra measure with external magnetic fields applied to the interferometer arms in anti-parallel direction. Dashed lines show the transmission spectra measured without magnetic fields. The poles of the permanent magnet are (a) S-N-S and (b) N-S-N.



(a)



(b)

Fig. 3.21 Measured transmission spectra for different propagation directions. The poles of the permanent magnet are (a) N-S-N and (b) S-N-S.

Figure 3.22 shows the calculated transmission loss of the isolator design assuming that the MMI couplers work ideally. The measured transmittance in Fig. 3.21 agrees well with the solid lines in Fig. 3.22, while the lack of a deep isolation feature at ~ 1550 nm is limited by the experimental noise floor at ~ 70 dB. Note that the bandwidth of the high isolation ratio observed in Fig. 3.20 is narrower than the calculation and is shifted by ~ 10 nm. These differences can be ascribed qualitatively to small dimensional errors in assembling the bonded garnet chip. These errors cause deviation of the reciprocal phase difference from the designed value of $+\pi/2$, since they make the interferometer arm asymmetry. The modified reciprocal phase difference is then give by

$$\theta_R = (\beta_1 - \beta_2)L_{\text{asym}} + \beta_2\Delta L \quad (3.8)$$

where β_1 and β_2 are the longitudinal propagation constants with upper cladding layer of Ce:YIG and air, respectively, ΔL is the designed optical path difference given by EB lithography, and L_{asym} is the assumed dimensional error. As an example, the dashed lines in Fig. 3.22 show the calculated transmission loss when there is a dimensional error of $111 \mu\text{m}$ propagation distance where the two interferometer arms have different upper cladding regions, i.e., Ce:YIG and air. In this case, the calculated transmission loss agrees with the measured results in Fig. 3.20.

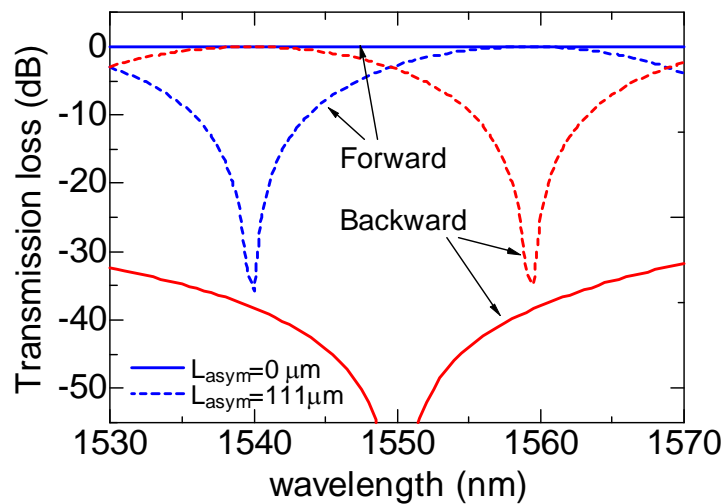


Fig. 3.22 Calculated transmission of the designed isolator. Solid lines show the transmission spectra without any dimensional error ($L_{\text{asym}} = 0 \mu\text{m}$), incurred during bonding. Dashed lines show the transmission spectra with an assumed dimensional error of $L_{\text{asym}} = 111 \mu\text{m}$.

3.5.2 Insertion loss

The insertion loss of the fabricated isolator is also examined. The measured transmission loss is dominated by a coupling loss of 37 dB between waveguide and fiber at the two waveguide-end facets. The value for coupling loss is obtained by fabricating a sample waveguide adjacent to the isolator, measuring the total insertion loss of this waveguide (41 dB), and subtracting off the waveguide propagation loss. The insertion loss due to the isolator itself is 8 dB at the transmission peak of 45 dB in Fig. 3.20. Of 8 dB loss, the excess loss of the interferometer is ~4 dB, total propagation loss of the interferometer waveguide is ~2.5 dB at a wavelength of 1550 nm based upon the 0.63 dB/mm transmission loss measured in Fig. 3.10 for 10-nm-height rib waveguide, and additional measured losses include ~0.2 dB after the direct bonding process due to Ce:YIG absorption and ~1.3 dB scattering losses at the bonding interfaces calculated in Fig. 3.4 for 0.3- μ m-thick waveguide.

3.5.3 Temperature dependence

Changing the temperature 20 – 60 °C with a temperature controller beneath the sample, the transmission spectrum of the isolator operation is measured as shown in Fig. 3.23, where the permanent magnet is fixed on the sample and the propagation direction is changed from (a) CW to (b) CCW direction in the measurement setup. The spectrum peak shifts about 3 nm as the temperature changes by 5 °C while the distance of corresponding peaks between forward and backward propagation directions is unchanged. This means that the temperature dependence of the nonreciprocal phase shift is small and the spectrum shifts are incurred by the temperature dependence of the refractive index of the composed materials. The phase difference between two symmetric arms ought to be unchanged since the refractive indices are simultaneously changed in both arms. The temperature dependences of refractive index $\Delta n/\Delta T$ in Si, SiO₂, and Ce:YIG are $1.8 \times 10^{-4}/^{\circ}\text{C}$, $1.0 \times 10^{-5}/^{\circ}\text{C}$, and $1.7 \times 10^{-5}/^{\circ}\text{C}$ (estimated from that of GGG [22]), respectively. On the other hand, there is no temperature dependence of refractive index in air. Thus, the measured spectrum shifts are mainly induced by the asymmetry in the MZI due to the assembly error as mentioned above. The difference in temperature dependence of the effective refractive index between the Ce:YIG and air cladding

regions along the estimated path length of 111 μm may give the spectrum shifts. The difference in the effective refractive index n_{eff} is estimated at 0.001 from the spectrum shifts of ~ 3 nm as the temperature changes by 5 $^{\circ}\text{C}$, i.e., $\Delta n_{\text{eff}}/\Delta T \sim 2.0 \times 10^{-4}/^{\circ}\text{C}$. However, this order is much larger than that of $\Delta n/\Delta T$ in Ce:YIG. Consequently, the $\Delta n_{\text{eff}}/\Delta T$ is caused by a difference in thermal diffusion at the waveguide surface between the Ce:YIG and air cladding regions since the temperature is provided from the bottom of substrate in this measurement. Anyway, the temperature dependence of the isolator operation can be restrained by an accurate fabrication ensuring the design.

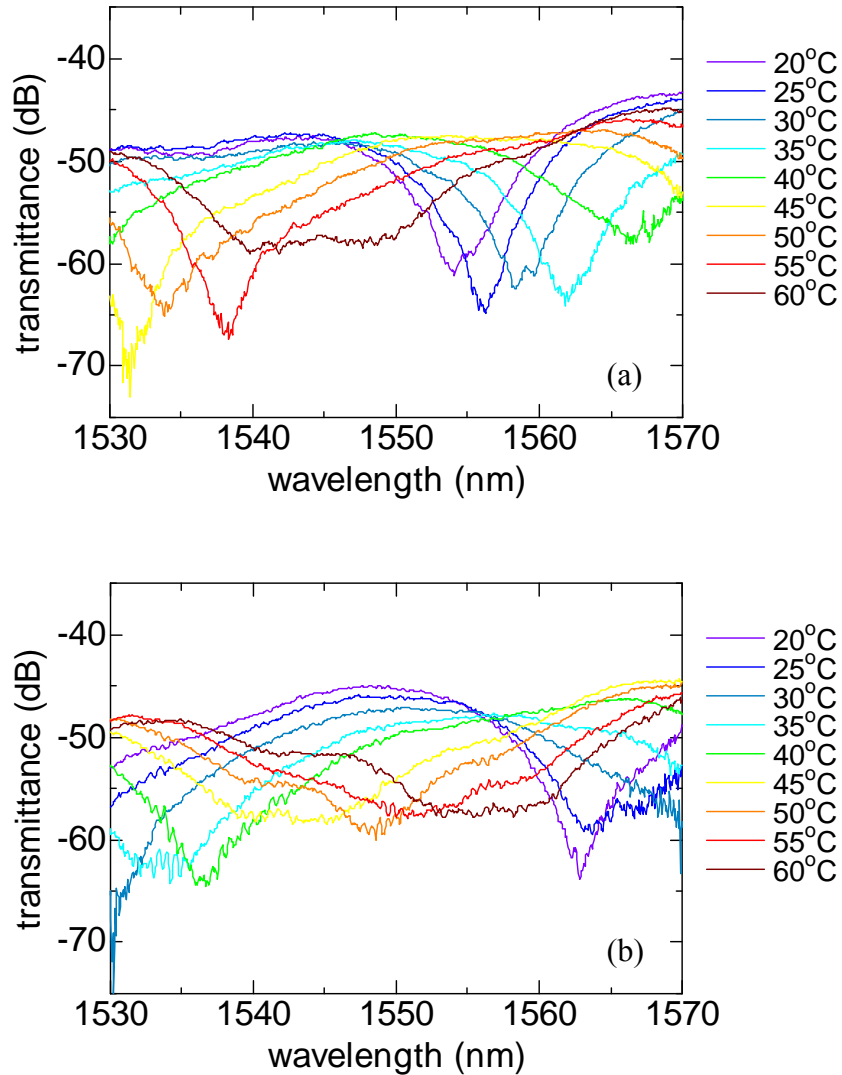


Fig. 3.23 Temperature dependence of the fabricated isolator. Light transmits the sample at (a)CW and (b)CCW directions in the measurement setup.

3.6 Discussion

A magneto-optical isolator with Si waveguides has been successfully demonstrated. And we need to discuss about the fabrication processes of Si waveguides and direct bonding technique prospecting for an ultracompact optical isolator.

The propagation loss and the bend loss can be reduced even for a Si-wire waveguide by using e-beam resist mask and etching with inductively coupled plasma (ICP) or electron cyclotron resonance (ECR). Yamada *et al.* realized a Si-wire waveguide with a propagation loss of 2.4 dB/cm, a 90-degree bend loss of 0.15 dB for 2- μ m-radius, and also the coupling loss from/into fiber of 0.5 dB through a spot-size converter of SiON second-core [1]. A MZI waveguides of the 0.36-mm-length ultracompact design shown in Table 3.2 can be realized with the insertion loss of about 2.9 dB including the propagation loss of ~ 0.9 dB, the two bend losses of ~ 0.3 dB, the scattering losses of ~ 1.2 dB at the two bonding boundaries, and the absorption loss of Ce:YIG of ~ 0.5 dB.

The direct bonding between Si and Ce:YIG is achieved by the surface activated bonding with oxygen plasma treatment at 200 – 250 °C which is compatible to a CMOS process. However, we have not examined the bonding strength yet. The annealing temperature should be determined after thermal durability testing in the temperature range of practical use.

The oxygen plasma treatment may generate ultrathin oxidized interlayer. The amorphous interlayer of Ce:YIG-rich without any magneto-optic effect or SiO₂-rich may be formed as eq. (3.3) and (3.4), respectively. Such interlayer makes the nonreciprocal phase shift smaller than the expected value, which results in longer propagation length to provide the designed nonreciprocal phase difference. Figure 3.24 shows the propagation length as a function of the interlayer thickness calculated by solving eigenvalue equation with four-layered structure. If there is an interlayer of 5-nm-thick SiO₂, which has been observed in the Si-to-Si bonding with oxygen plasma bonding in Ref. [15], the required propagation length changes by ~ 20 %. Therefore, we need to investigate the thickness and composition of the interlayer relating to the bonding conditions by using a transmission electron microscopy (TEM) and a X-ray photoelectron spectroscopy (XPS). Also, the amount of the nonreciprocal phase shift in the Ce:YIG/Si/SiO₂ waveguide should be examined by a measurement setup described in Ref

[20] or [21].

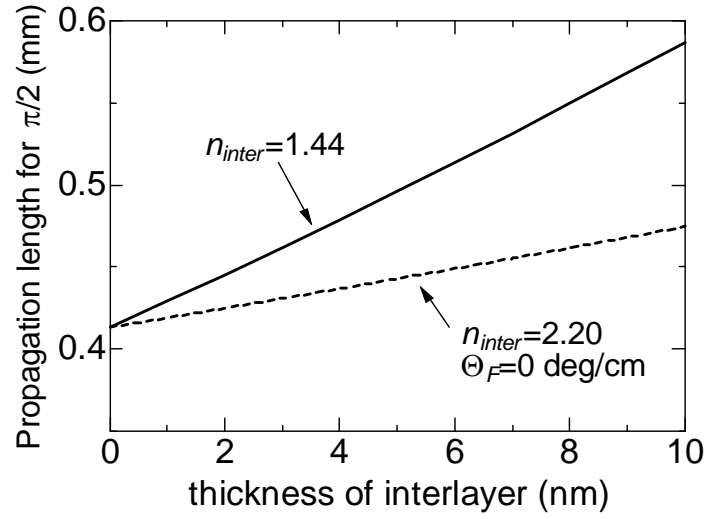


Fig. 3.24 Propagation length to obtain $\pm\pi/2$ nonreciprocal phase difference, where top layer is Ce:YIG ($n=2.20$) with $\Theta_F = -4500$ deg/cm, guiding layer is 0.3- μm -thick Si ($n=3.48$), lower cladding layer is SiO_2 ($n=1.44$), and the interlayer is located between top and guiding layers.

In order to obtain a high extinction in a MZI, it is important to balance the optical power in two arms. As described in Chapter 2, the output intensity of a MZI is expressed as (2.53)

$$|E_{out}|^2 = \frac{1}{4} \left\{ a_1 + a_2 + 2\sqrt{a_1 a_2} \cos(\theta_2 - \theta_1) \right\} |E_{in}|^2$$

where E_{in} and E_{out} are the amplitudes of the electric field at the input and output ports and θ_1 , θ_2 , a_1 , and a_2 are the phase differences and attenuations of power in each arm. Figure 3.25 shows the calculated output powers as a function of balance in two arms a_2/a_1 where the phase differences ($\theta_2 - \theta_1$) are in-phase and antiphase for forward and backward operations, respectively. The balance must be more than 0.9 to achieve an isolation ratio > 30 dB. The sub Mach-Zehnder structures in the MZI arms have been proposed for achieving high extinction ratio (~ 48 dB) [23]. The sub MZI is used as an attenuator to compensate the unbalance of powers in two arms. In the case of our isolator with Si waveguide, ultraviolet light irradiation can adjust the phase difference in the sub MZIs by changing the refractive indices of Si and SiO_2 after fabrication of the isolator.

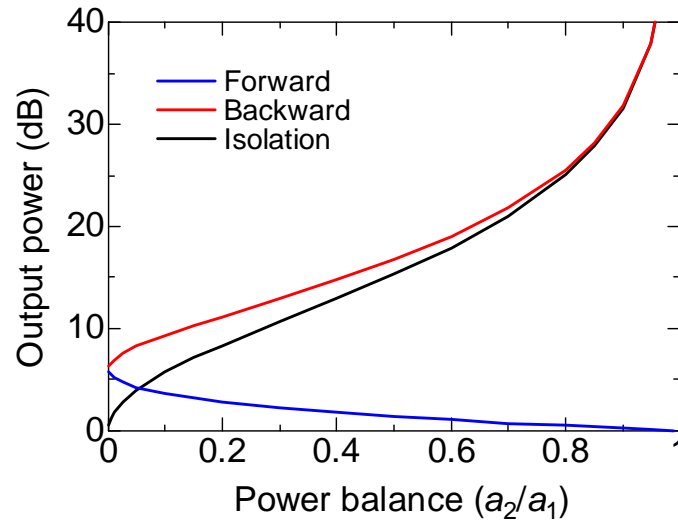


Fig. 3.25 Output power of a MZI as a function of balance of the intensities in two arms.

In consideration of mass productivity, there is difficulty in integrating refractory magneto-optic garnet crystals. It is impossible to cleave the Si gently with the garnet crystal. Dicing is necessary to cut the Si substrate with the garnet crystal in order to separate one device from the massively produced wafer. To separate the devices by means of cleaving, crystal ion slicing technique [24] is useful. Fig. 3.26 shows a schematic drawing of the fabrication process of the magneto-optical isolator with photonic integrated circuits on a Si substrate by using a crystal ion slicing technique. As shown in Fig. 3.1, laser diodes, optical modulators, their drive circuits, and optical waveguides for isolators without magnetic garnet crystals are fabricated all over one wafer with Si-LSI process. Grooves are formed on the surface of the garnet crystals coincident with a period of the device. Proper ions are implanted on the garnet crystals with a depth smaller than that of the grooves from the top surface. Then, the garnets are bonded onto the Si substrate by the direct bonding technique. By selective etching or rapid thermal annealing, the garnet substrate is removed and thin garnet layers are left on the Si substrate due to crystal ion slicing. Therefore, each device can be separated by cleaving the Si substrate. By preparing such grooved magneto-optic garnet crystals, a number

of photonic circuits integrated with a magneto-optical isolator can be fabricated in a single direct bonding process.

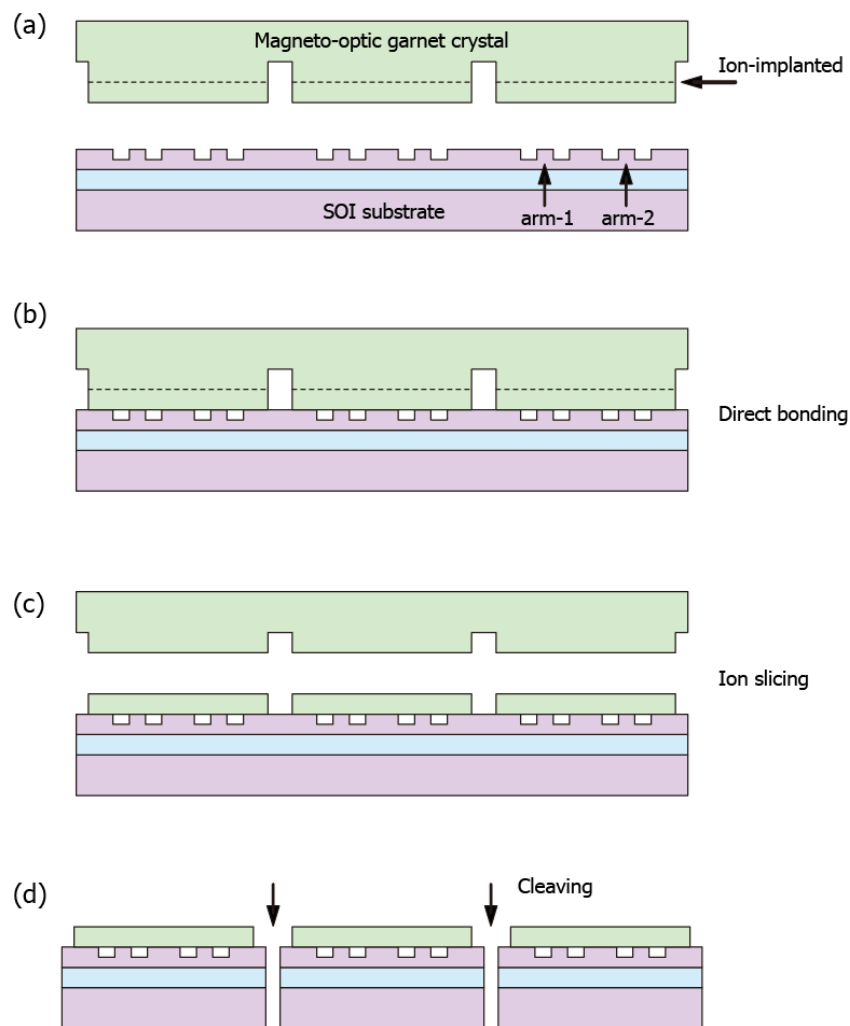


Fig. 3.26 Integration process of magneto-optical isolator with Si photonic circuits using a crystal ion slicing technique in consideration of mass productivity.

3.7 Summary

In this chapter, a magneto-optical isolator with Si waveguide is demonstrated. First, Si waveguide is fabricated on a SOI wafer and characterized. Second, a surface activated direct bonding with oxygen plasma treatment is investigated. A direct bonding between Si and Ce:YIG is successfully achieved with oxygen plasma treatment of 100-W RF power for 30-s followed by annealing at 200 – 250 °C with an applied pressure of ~5 MPa. Then, a magneto-optical isolator composed of a 0.3- μ m-thick Si rib waveguide for low-loss design is fabricated and characterized in terms of the nonreciprocal operation by reversing the propagation direction. The maximum isolation of 21 dB is obtained at a wavelength of 1559 nm. The insertion loss of 8 dB and the temperature dependence of the isolator are also examined.

References

- [1] K. Yamada, T. Tsuchizawa, T. Watanabe, J. Takahashi, H. Fukuda, M. Takahashi, T. Shoji, S. Uchiyama, E. Tamechika, S. Itabashi, and H. Morita, "Microphotronics devices based on silicon wire waveguiding system," *IEICE Trans. Electron.*, vol.E87-C, pp.351-357 (2004).
- [2] A. Liu, L. Liao, D. Rubio, H. Nguyen, O. Cohen, R. Nicholaescu, and M. Paniccia, "High-speed optical modulation based on carrier depletion in a silicon waveguide," *Opt. Express*, vol.15, pp.660-668 (2007).
- [3] A. W. Fang, H. Park, O. Cohen, R. Jones, M. J. Paniccia, and J. E. Bowers, "Electrically pumped hybrid AlGaInAs-silicon evanescent laser," *Opt. Express*, vol.14, pp.9203-9210 (2006).
- [4] Product information of Luxtera, Inc., (<http://www.luxtera.com/>)
- [5] H. Yokoi, T. Mizumoto, and Y. Shoji, "Optical nonreciprocal devices with a silicon guiding layer fabricated by wafer bonding," *Appl. Opt.*, vol.42, pp.6605-6612 (2003).
- [6] R. L. Espinola, T. Izuhara, M.-C. Tsai, and R. M. Osgood, Jr., "Magneto-optical nonreciprocal phase shift in garnet/silicon-on-insulator waveguides," *Opt. Lett.*, vol.29, pp.941-943 (2004).
- [7] BeamPROP software from RSoft Design Group, (<http://www.rsoftdesign.com/>)
- [8] FIMMPROP software from Opto Design Inc., (<http://www.opto-design.com/>)
- [9] M. Bruel, B. Aspar, B. Charlet, C. Maleville, T. Poumeyrol, A. Soubie, A. J. Auberton-Herve, J. M. Lamure, T. Barge, F. Metral, and S. Trucchi, "@Smart cut : a promising new SOI material technology," *Proc. of 1995 IEEE International SOI Conference*, pp.178-179 (1995).
- [10] J. Steinkirchner, T. Martini, M. Reiche, G. Kästner, and U. Gösele, "Silicon wafer bonding via designed monolayers," *Adv. Mater.*, vol.7, pp.662-665 (1995).
- [11] U. Gösele, H. Stenzel, T. Martini, J. Steinkirchner, D. Conrad, and K. Scheerschmidt, "Self-propagating room-temperature silicon wafer bonding in ultrahigh vacuum," *Appl. Phys. Lett.*, vol.67, pp.3614-3616 (1995).
- [12] H. Takagi, K. Kikuchi, R. Maeda, T. R. Chung, and T. Suga, "Surface activated bonding of silicon wafers at room temperature," *Appl. Phys. Lett.*, vol.68, pp.2222-2224 (1996).
- [13] A. Berthold, B. Jakoby, and M. J. Vellekoop, "Wafer-to-wafer fusion bonding of oxidized silicon to silicon at low temperatures," *Sens. Actuators*, vol.A68, pp.410-413 (1998).
- [14] Q.-Y. Tong, W. J. Kim, T.-H. Lee, and U. Gösele, "Low vacuum wafer bonding," *Electrochem.*

Solid State Lett., vol.1, pp.52-53 (1998).

- [15] D. Pasquariello and K. Hjort, "Plasma-assisted InP-to-Si low temperature wafer bonding," IEEE J. Selected Topics in Quantum Electron., vol.8, pp.118-131 (2002).
- [16] T. Suga, T. H. Kim, and M. M. R. Howlader, "Combined process for wafer direct bonding by means of the surface activation method," Proc. of Electronic Components and Technology Conference, pp.484-490 (2004).
- [17] U. Gösele, S. Hopfe, S. Li, S. Mack, T. Martini, M. Reiche, E. Schmidt, H. Stenzel, and Q.-Y. Tong, "What determines the lateral bonding speed in silicon wafer bonding?," Appl. Phys. Lett., vol.67, pp.863-865 (1995).
- [18] R. Hull, "Properties of crystalline silicon," (University of Verginia, Verginia, 1999), Chap.5, pp.219-225.
- [19] T. Izuhara, M. Levy, and R. M. Osgood, Jr., "Direct bonding and transfer of 10- μ m-thick magnetic garnet films onto semiconductor surfaces," Appl. Phys. Lett., vol.76, pp.1261-1263 (2000).
- [20] Y. Okamura, H. Inuzuka, T. Kikuchi, and S. Yamamoto, "Nonreciprocal propagation in magnetooptic YIG rib waveguides," J. Lightwave Technol., vol.LT-4, pp.711-714 (1986).
- [21] J. Fujita, M. Levy, R. U. Ahmad, and R. M. Osgood, Jr., "Observation of optical isolation based on nonreciprocal phase shift in a Mach-Zehnder interferometer," Appl. Phys. Lett., vol.75, pp.998-1000 (1999).
- [22] D. L. Wood and K. Nassau, "Optical properties of gadolinium gallium garnet," Appl. Opt., vol.29, pp.3704-3707 (1990).
- [23] A. Chiba, T. Kawanishi, T. Sakamoto, K. Higuma, and M. izutsu, "Low-crosstalk operation of LiNbO₃ optical switch having sub Mach-Zehnder structures," Proc. of 2006 IEICE Society Conference, p.178 (2006).
- [24] M. Levy, R. M. Osgood, Jr., A. Kumar, and H. Bakhru, "Epitaxial liftoff of thin oxide layers: Yttrium iron garnets onto GaAs," Appl. Phys. Lett., vol.71, pp.2617-2619 (1997).

Chapter 4:

Wideband Operation of a Magneto-Optical Isolator Using Phase Adjustment in Mach-Zehnder Interferometer

4.1 Introduction

Optical nonreciprocal devices are important components in high speed optical communication systems. At present, only bulk isolators are commercially available, which are not suitable for integration. In addition, the operation bandwidth where the isolation >30 dB is obtained is typically ± 30 nm around its center wavelength due to a large wavelength dependence of Faraday rotation of magneto-optic materials. Ando *et al.* demonstrated a waveguide isolator using TE-TM mode conversion with the isolation ratio of 12.5 dB [1]. Shintaku demonstrated a waveguide isolator using nonreciprocal radiation mode conversion with the isolation of 27 dB [2]. However, they suffered small fabrication tolerance as well as the narrow operation bandwidth.

A waveguide isolator employing nonreciprocal phase shift has been intensively investigated in Mach-Zehnder interferometer (MZI) configuration [3-7]. It is less sensitive to a fabrication error because there is no need of phase matching between orthogonally polarized modes. Fujita *et al.* demonstrated it with the isolation ratio of around 19 dB at a wavelength range of $1.49 - 1.57$ μm which is wider than the operation bandwidth of bulk isolators [7]. However, the wavelength dependence of this isolator has not been fully investigated. In this chapter, the author proposes and demonstrates a wideband operation of the isolator using phase adjustment in MZI. First, he explains the proposed principle of wideband operation. Next, the numerical results of the wideband design are presented for several types of the isolator, and

the influence on the fabrication tolerance is discussed in the wideband design. An ultra-wideband design operating at a wavelength range in $1.31 - 1.55 \mu\text{m}$ is investigated. A magnet-optical isolator is fabricated with the wideband design on a magneto-optic garnet waveguide, and the successful wideband operation is demonstrated experimentally.

4.2 Principle of wideband operation

The magneto-optical isolator is based on a MZI composed of nonreciprocal phase shifter (NPS) and reciprocal phase shifter (RPS) as shown in Fig 4.1. External magnetic fields are applied to the arms of NPS in anti-parallel directions to obtain a nonreciprocal phase difference (θ_N) of $\pm\pi/2$ in a push-pull manner. A reciprocal phase difference (θ_R) is provided by an optical path difference between two arms. In the conventional design, θ_R is set to be $+\pi/2$ to cancel the θ_N or add to the θ_N , which results in constructive or destructive interference in forward or backward direction, respectively. The phase differences are set at a center wavelength (λ_0) of the designed transmission bandwidth, e.g., $\lambda = 1.55 \mu\text{m}$. Figure 4.2 shows the schematic wavelength dependence of θ_N , θ_R , and the total phase difference in two directions. Typically, θ_N and θ_R decrease monotonically as the wavelength becomes longer. The wavelength dependence of θ_N is dominated by the field distribution and the Faraday rotation of the magneto-optic material. The wavelength dependence of θ_R is dominated by the refractive indices of the waveguide structure and the wavenumber k . Deviations of the nonreciprocal and reciprocal phase differences from respective designed values are cancelled in the forward direction, while added in the backward direction as shown in Fig. 4.2 (a) and (b). This behavior determines the wavelength dependence of the isolator operation, and large backward loss is obtained only in a narrow wavelength range.

To obtain a large backward loss in a wide wavelength range, we change the phase differences as shown in the lower part of Fig. 4.1. The θ_R is set to be $+3\pi/2$, instead of $+\pi/2$, and the sign of the θ_N is reversed, which is done just by reversing the direction of applied magnetic field, to satisfy the isolator operation. This makes the backward loss less sensitive to wavelength change as shown in Fig. 4.2 (c) and (d). In addition, the wavelength dependence of θ_R is adjusted by tailoring the waveguide parameters such as waveguide width and length

of the reciprocal phase shifter as shown in Fig 4.3. Then the θ_R is expressed as $\beta_2 L_2 - \beta_1 L_1$ with the longitudinal propagation constants β_1 , β_2 and their modified lengths L_1 , L_2 . When the deviation of θ_R cancels that of θ_N in a wide wavelength range, the wideband operation of isolator is realized. On the other hand, wavelength dependence of the forward loss is deteriorated compared with the conventional design as one can see in Fig. 4.2 (d). However, the increase in the forward loss is acceptably small for a dramatic improvement of the backward loss, which is shown by the calculation results mentioned in the next section.

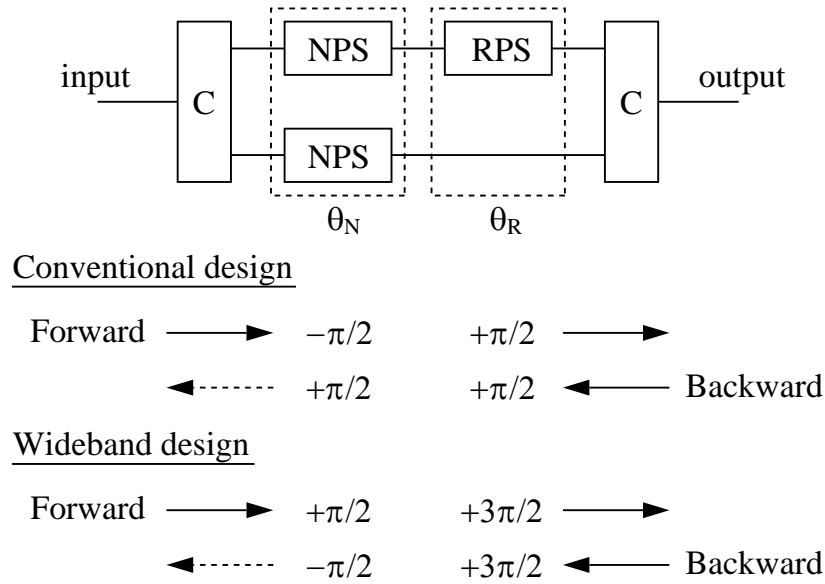


Fig. 4.1 Schematic diagram of MZI configuration of magneto-optical isolator employing nonreciprocal phase shift.

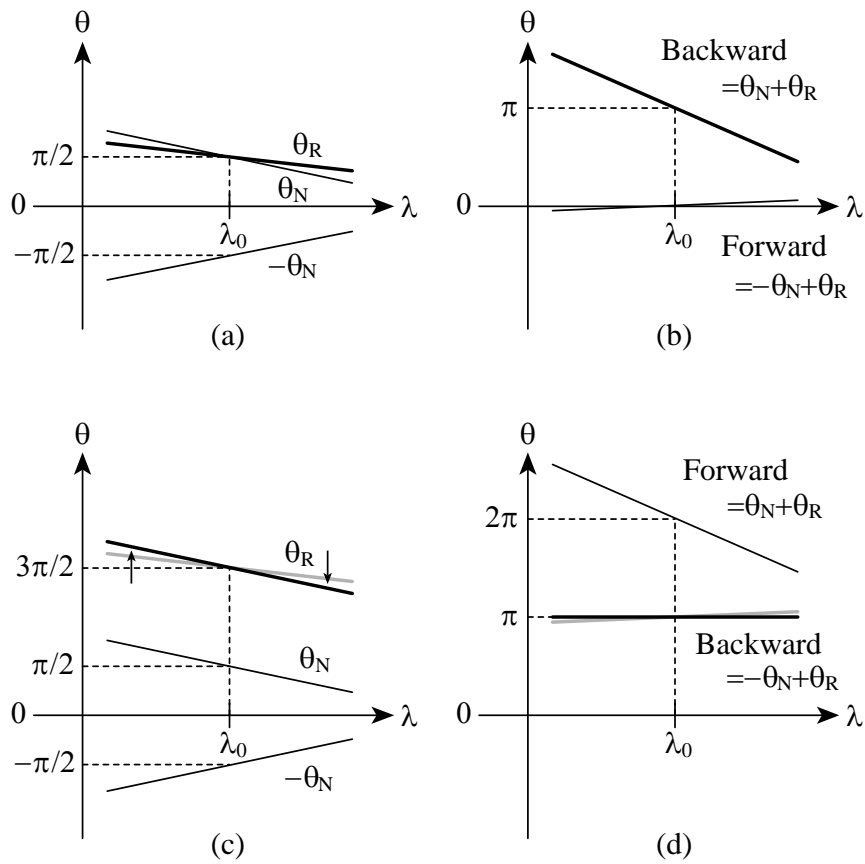


Fig. 4.2 Schematic illustration of wavelength dependence of nonreciprocal and reciprocal phase differences and the total phase differences in the MZI isolator. (a), (b) correspond to the conventional design and (c), (d) correspond to the wideband design.

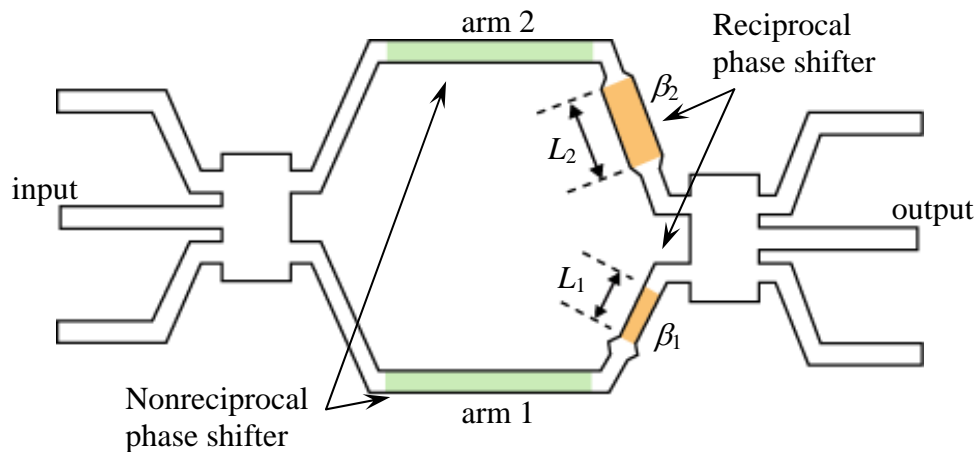


Fig. 4.3 Tailoring waveguide width and length to adjust a wavelength dependence of the reciprocal phase difference.

4.3 Calculation results

4.3.1 Wideband design of three types of isolator

Figure 4.4 shows three types of magneto-optical isolator employing nonreciprocal phase shift we have investigated. These isolators are composed of a magneto-optic garnet rib waveguide (type-1), a GaInAsP/InP rib waveguide (type-2), and a Si-wire waveguide (type-3), respectively. The latter two isolators have a magneto-optic garnet upper cladding layer that is bonded on the waveguide by use of a direct bonding technique [8-10]. The type-2 isolator is attractive for monolithic integration with a laser diode of compound semiconductor. The type-3 isolator is realized in ultracompact size as described in Chapter 3.

In the following design, a $\text{CeY}_2\text{Fe}_5\text{O}_{12}$ (Ce:YIG) grown on a (111)-oriented (Ca, Mg, Zr) doped GGG substrate (SGGG) is used as a magneto-optic garnet. We assume the 3 dB couplers work ideally to clarify the validity of the idea. The cross sectional image of the waveguide structures in the nonreciprocal phase shifter is shown in Fig. 4.5, where the latter two structures have side-cladding layer of air so that they are realized by a direct bonding. On the other hand, in the reciprocal phase shifter, the upper and side cladding layers are air for the type-2 structure and SiO_2 for the type-3 structure. The refractive indices and the Faraday rotation coefficient of the materials are expressed as shown in Table 4.1 approximating the wavelength dependence with a quadratic polynomial. The approximations are based on the listed references, except Si and SiO_2 obtained from ellipsometry measurement for a SOI wafer. The waveguide width, thickness, and rib height are set as shown in Table 4.2 so that the TM propagation is single-mode. The propagation constant is calculated by mode solving of full-vector FEM [16].

First, the θ_N is designed with the propagation length of nonreciprocal phase shifter so as to be $\pm\pi/2$ at $\lambda = 1.55 \mu\text{m}$. The nonreciprocal phase shift is calculated by perturbation theory as described in Chapter 2. The wavelength dependence of θ_N is determined by the nonreciprocal phase shift for the fixed propagation length L designed at $\lambda = 1.55 \mu\text{m}$.

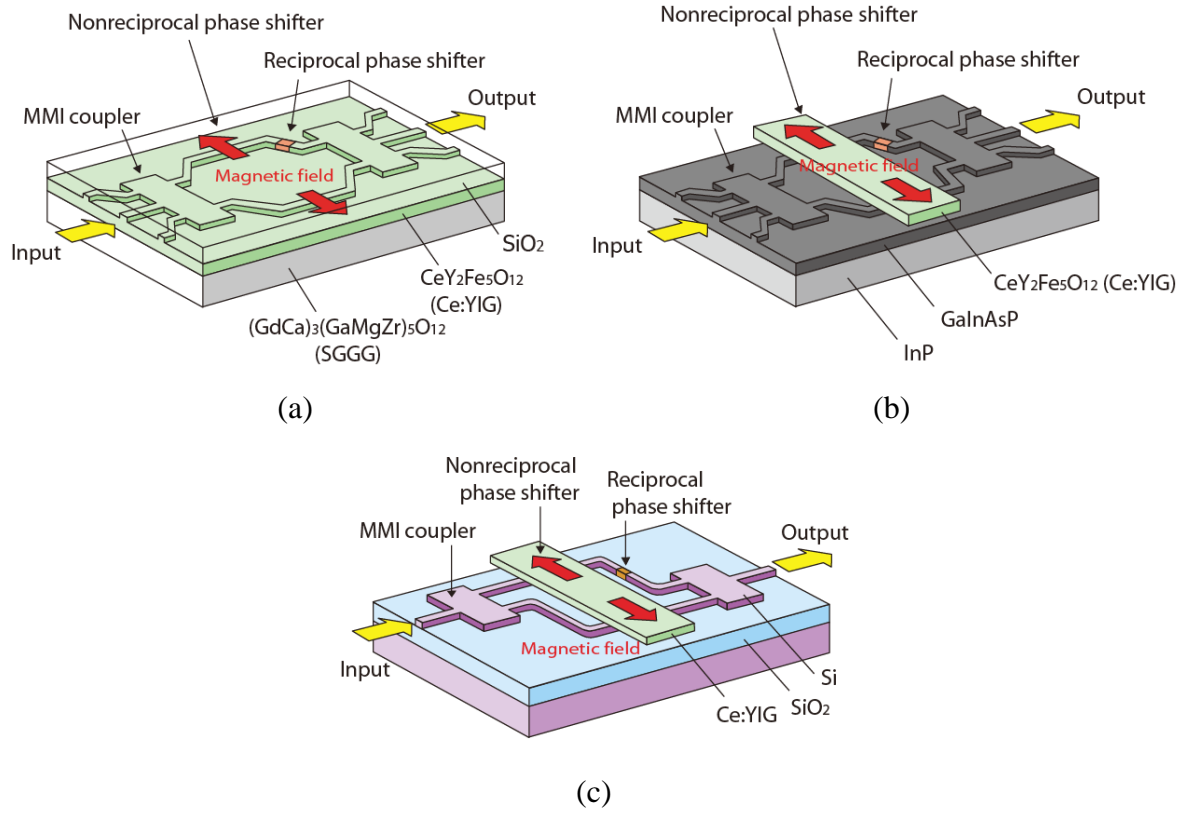


Fig. 4.4 Three types of magneto-optical isolator employing nonreciprocal phase shift.

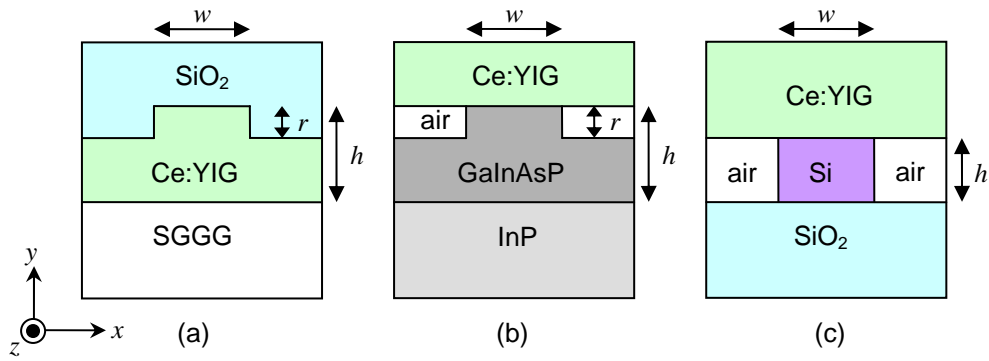


Fig. 4.5 Waveguide structures of the nonreciprocal phase shifter.

Table 4.1 Refractive indices approximated as a function of the wavelength λ (μm).

Material	Refractive index $n(\lambda)$	Ref.
Ce:YIG	$2.2122709 - 0.0079167 * \lambda$	[11-13]
SGGG	$1.9661938 - 0.0270747 * \lambda + 0.00656483 * \lambda^2$	[13,14]
GaInAsP ($\lambda_g = 1.42 \mu\text{m}$)	$5.81338353 - 2.72352246 * \lambda + 0.772876982 * \lambda^2$	[15]
InP	$3.66193927 - 0.516531590 * \lambda + 0.128646194 * \lambda^2$	[15]
Si	$3.8152773 - 0.349117169 * \lambda + 0.085683376 * \lambda^2$	-
SiO ₂	$1.44716 - 0.00787891 * \lambda + 0.00210296 * \lambda^2$	-
Faraday rotation of Ce:YIG	$-20000 + 10000 * \lambda$ (deg/cm)	[11-13]

Next, the width of one arm in the reciprocal phase shifter is modified. In the case of type-1 isolator, the modified width is set at $w_2 = 2.4 \mu\text{m}$ against the waveguide width $w_1 = 2.0 \mu\text{m}$. Then the L_1 and L_2 are adjusted so that the θ_R is $\sim 3\pi/2$ at $\lambda = 1.55 \mu\text{m}$ and the wavelength dependence of θ_R is similar to that of θ_N . The section lengths of the reciprocal phase shifter are designed at $L_1 = 10.0 \mu\text{m}$ and $L_2 = 10.575 \mu\text{m}$, and the wavelength dependences of θ_N and θ_R for type-1 isolator are calculated as shown in Fig. 4.6 (a). The total phase differences of the MZI in both propagation directions are calculated as shown in Fig. 4.6 (b). One can see that the total phase difference of the backward direction in the wideband design is very flat as the wavelength since the wavelength dependences of θ_N and θ_R are cancelled each other. Fig. 4.7 shows the forward and backward losses of the type-1 isolator calculated from the phase differences. The backward loss exhibits tremendous improvement in the wideband design. The wavelength range with the isolation ratio of $>30 \text{ dB}$ is over 200 nm at $\lambda = 1.45 - 1.65 \mu\text{m}$ in the wideband design while that is 30 nm at $\lambda = 1.535 - 1.565 \mu\text{m}$ in the conventional design. On the other hand, the forward loss of the wideband design gets worst compared with the conventional design as predicted from Fig. 4.2 (d). However, the deterioration is $<0.5 \text{ dB}$ in the calculated wavelength range, which is acceptably small against the dramatic improvement of the backward loss.

In the same way, wideband designs are investigated in the type-2 and type-3 isolators. In the case of type-2 isolator, the modified widths are $w_2 = 1.6 \mu\text{m}$ against $w_1 = 1.5 \mu\text{m}$ and the

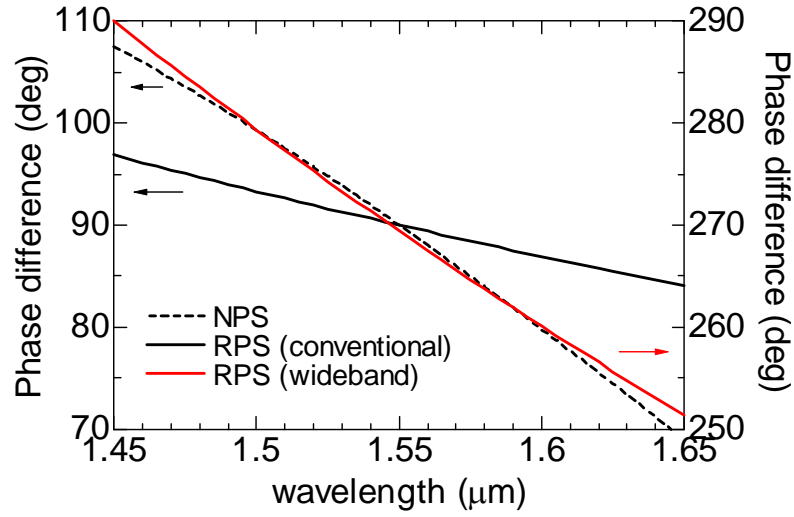
section lengths are designed at $L_1 = 6.0 \mu\text{m}$ and $L_2 = 6.279 \mu\text{m}$. The phase differences in the MZI are calculated as shown in Fig. 4.8. The forward and backward losses are obtained from them as shown in Fig. 4.9. The wavelength range with the isolation ratio of $>30 \text{ dB}$ is over 200 nm at $\lambda = 1.45 - 1.65 \mu\text{m}$ in the wideband design while that is 20 nm at $\lambda = 1.54 - 1.56 \mu\text{m}$ in the conventional design. The deterioration of the forward loss is $<1.0 \text{ dB}$ in the calculated wavelength range.

In the case of type-3 isolator, the modified widths are $w_2 = 0.7 \mu\text{m}$ against $w_1 = 0.6 \mu\text{m}$ and the section lengths are designed at $L_1 = 40.0 \mu\text{m}$ and $L_2 = 39.68 \mu\text{m}$. The phase differences in the MZI are calculated as shown in Fig. 4.10. The forward and backward losses are obtained from them as shown in Fig. 4.11. The wavelength range with the isolation ratio of $>30 \text{ dB}$ is $\sim 110 \text{ nm}$ at $\lambda = 1.485 - 1.595 \mu\text{m}$ in the wideband design while that is 20 nm at $\lambda = 1.54 - 1.56 \mu\text{m}$ in the conventional design. The deterioration of the forward loss is $<1.5 \text{ dB}$ in the calculated wavelength range. The type-3 isolator shows larger wavelength dependence of the reciprocal phase difference even in the wideband design. This is because Si has larger wavelength dependence than any other materials. In addition, the high-index-contrast waveguide is sensitive to the dimensional modification.

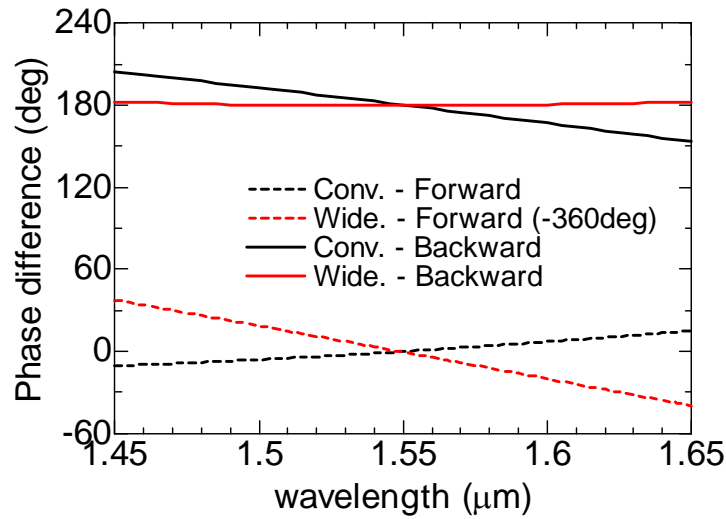
These designs are examples of the wideband design with a combination of modified waveguide width. The design concept is applicable to the isolator with any other material, structure, and dimension.

Table 4.2 Waveguide dimension of the wideband designs. (unit: μm)

	Type-1	Type-2	Type-3
Height (h)	0.48	0.36	0.22
Rib height (r)	0.08	0.16	0.22
Width (w_1)	2.0	1.5	0.6
Modified width (w_2)	2.4	1.6	0.7
Conventional design (L_{RPS})	0.196	0.121	0.212
Wideband design (L_1 / L_2)	10.0 / 10.575	6.0 / 6.279	40.0 / 39.68

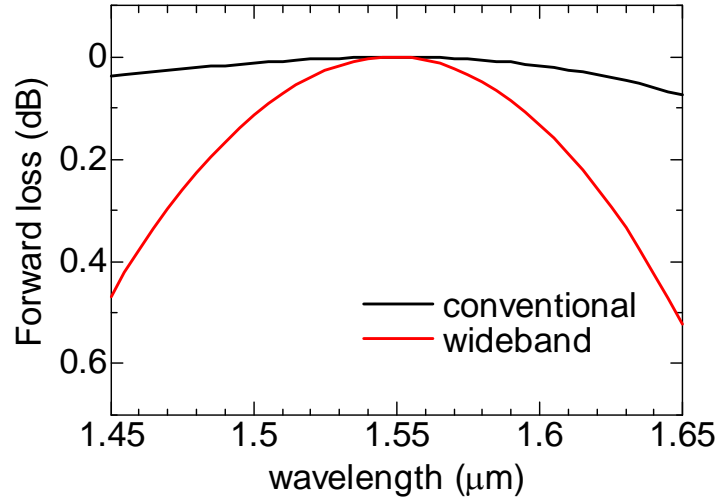


(a)

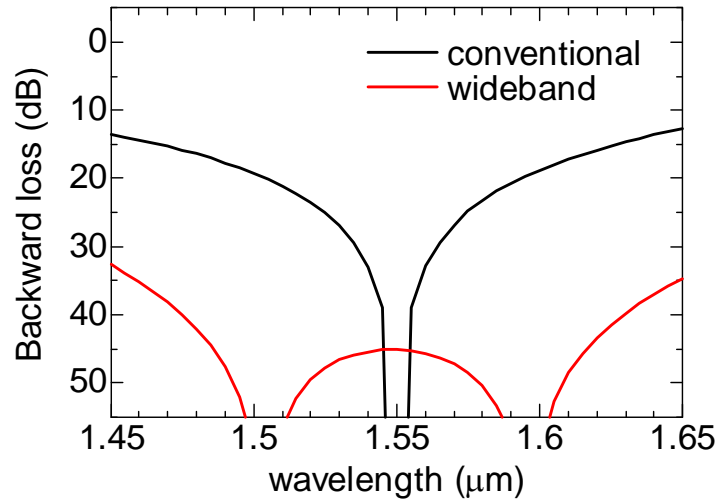


(b)

Fig. 4.6 (a) Phase differences in the nonreciprocal and reciprocal phase shifters, and (b) total phase differences of the MZI in both propagation directions for type-1 isolator

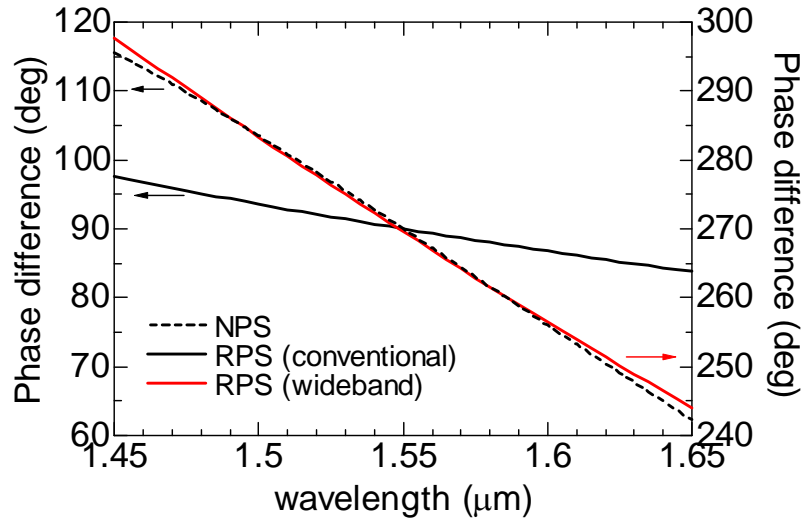


(a)

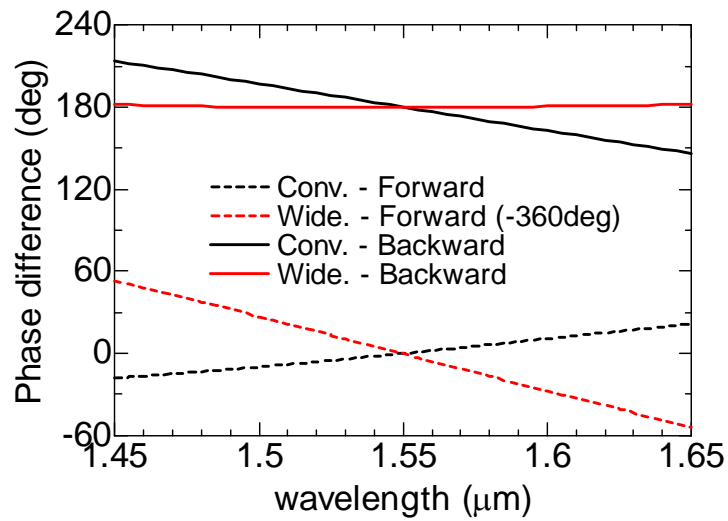


(b)

Fig. 4.7 Wavelength dependence of the (a) forward loss and (b) backward loss in conventional and wideband designs for type-1 isolator.

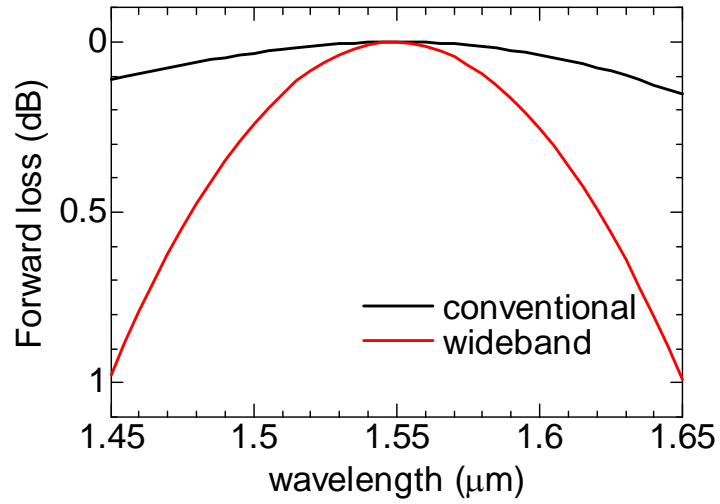


(a)

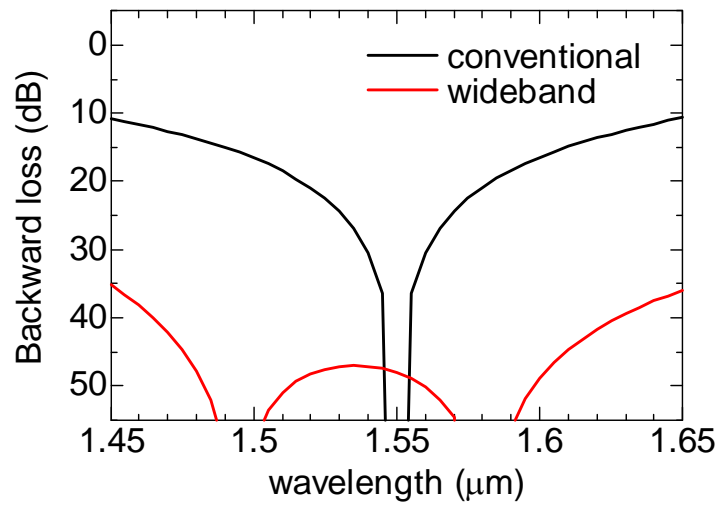


(b)

Fig. 4.8 (a) Phase differences in the nonreciprocal and reciprocal phase shifters, and (b) total phase differences of the MZI in both propagation directions for type-2 isolator

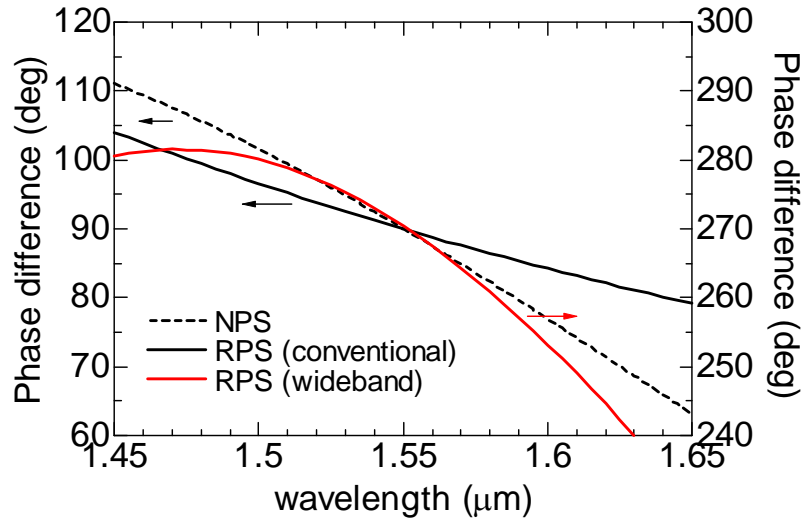


(a)

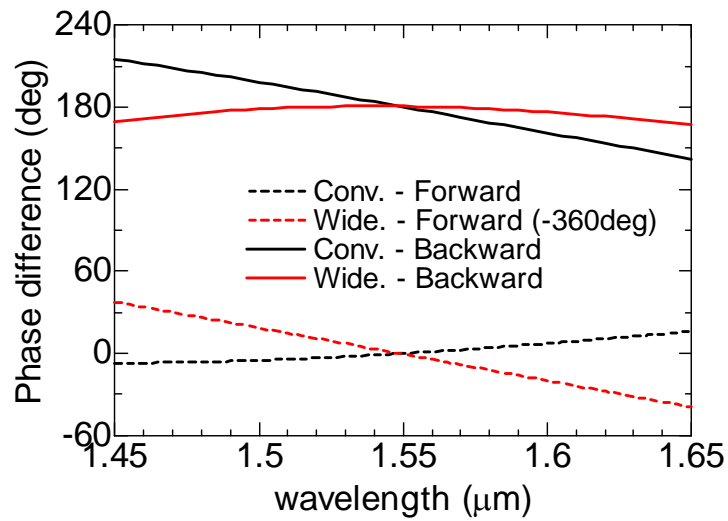


(b)

Fig. 4.9 Wavelength dependence of the (a) forward loss and (b) backward loss in conventional and wideband designs for type-2 isolator.

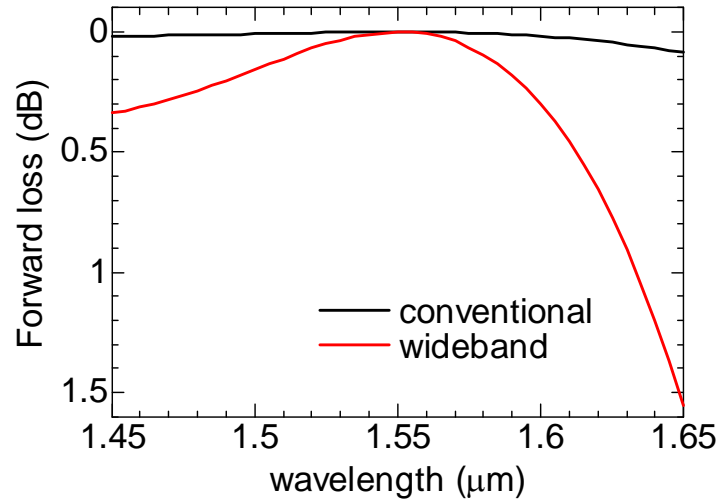


(a)

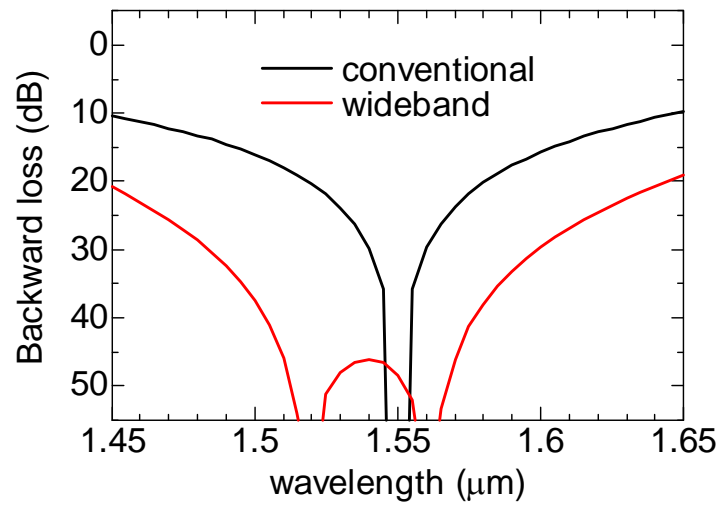


(b)

Fig. 4.10 (a) Phase differences in the nonreciprocal and reciprocal phase shifters, and (b) total phase differences of the MZI in both propagation directions for type-3 isolator



(a)



(b)

Fig. 4.11 Wavelength dependence of the (a) forward loss and (b) backward loss in conventional and wideband designs for type-3 isolator.

4.3.2 Fabrication tolerance

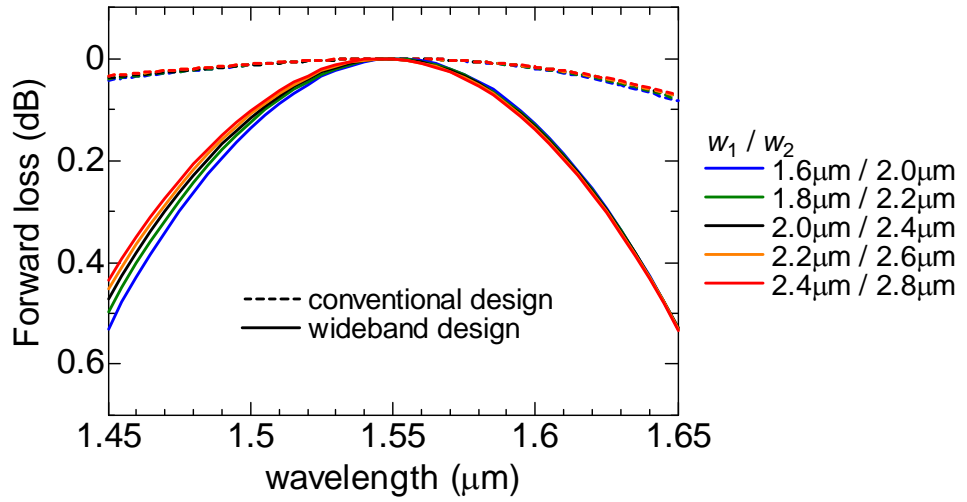
We examine the dependence of fabrication errors in the wideband design comparing with the case of the conventional design. We assume three fabrication errors in waveguide width, rib height, and optical path length for the type-1 isolator.

The waveguide width may have some errors caused in the fabrication process. Fig. 4.12 shows the wavelength dependence with errors in the waveguide widths w_1 and w_2 , where uniform errors are assumed along the whole waveguides. The θ_N is re-calculated for every w_1 . A combination of narrow widths makes the θ_R large as the difference in propagation constants β_1 and β_2 increase. Since the change of θ_R is larger than that of θ_N , the total phase difference in the backward direction slightly increases from the designed one for a combination of narrow widths, and vice versa. Slightly concave wavelength dependence of the backward direction as shown in Fig. 4.8 (b) determines the wavelength dependence of the backward loss. That is, the extinction peaks appear when the total phase difference corresponds to π .

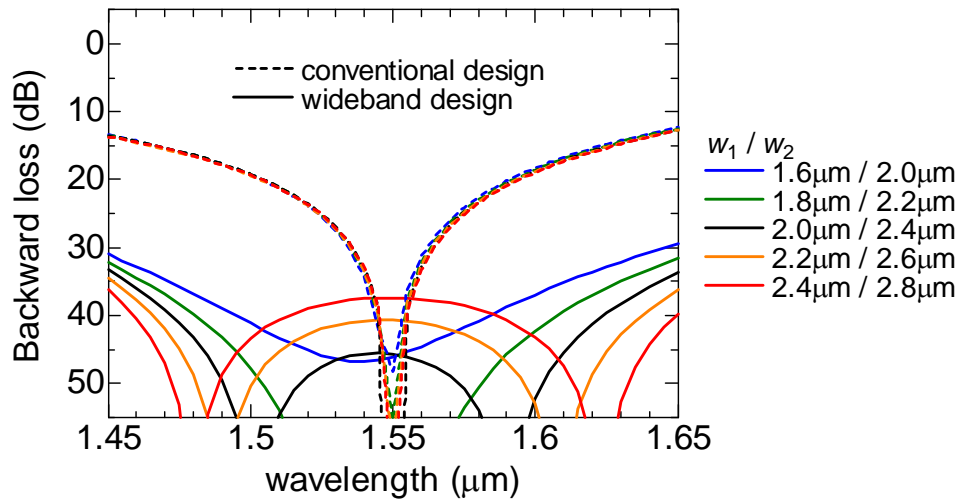
The rib height may also have some errors caused in the fabrication process. Fig. 4.13 shows the wavelength dependence with errors in the rib height of all waveguide of the isolator. The θ_N is also re-calculated for every rib height. In this case, both the propagation constants β_1 and β_2 increase for smaller rib height since the light field distributes less in the side cladding layer. These increments are larger in β_1 than β_2 , and the θ_R becomes small for smaller rib height. On the other hand, the θ_N hardly changes as the rib height. Therefore, the total phase difference in the backward direction slightly decreases from the designed one for a smaller rib height, and vice versa. The backward loss is determined by the slightly concave wavelength dependence of the total phase difference.

The optical path lengths of MZI arms are precisely determined by e-beam lithography. An error induced in both arms with the same amount can be neglected since it provides no phase difference between two arms. So, very small error in the length of one arm is considered. Fig. 4.14 shows the wavelength dependence with an error in the modified length L_2 of the reciprocal phase shifter in the wideband design and in the path length of one arm in the conventional design. The difference in optical path length between two arms is very important for MZI to provide the phase difference. Even in the conventional design, the wavelength

dependence shifts ~ 20 nm with the errors from -5.0 nm to $+5.0$ nm. This is a serious problem because the wavelength range with >30 dB isolation ratio is just ~ 30 nm. Even though the backward loss in the wideband design changes significantly, the isolation ratio remains high (>30 dB) in a wide wavelength range. One can see that the fabrication tolerance is improved in the wideband design compared with that in the conventional design.

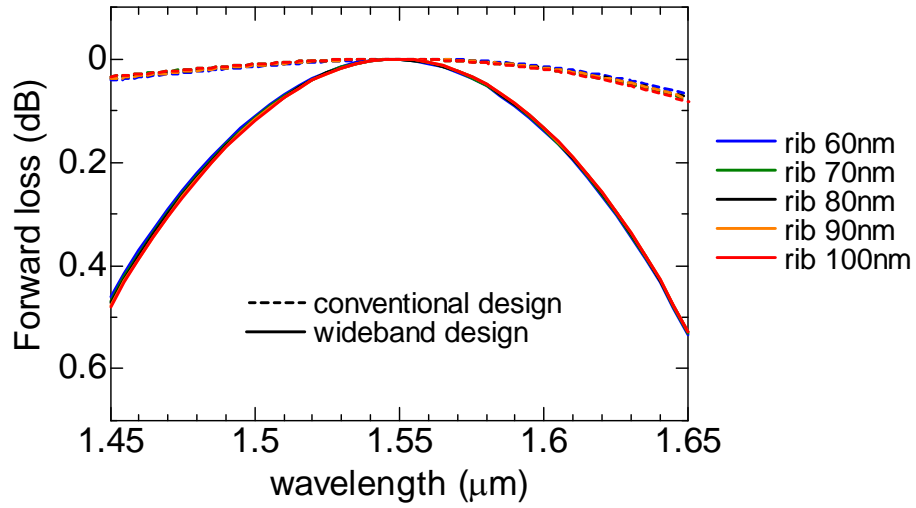


(a)

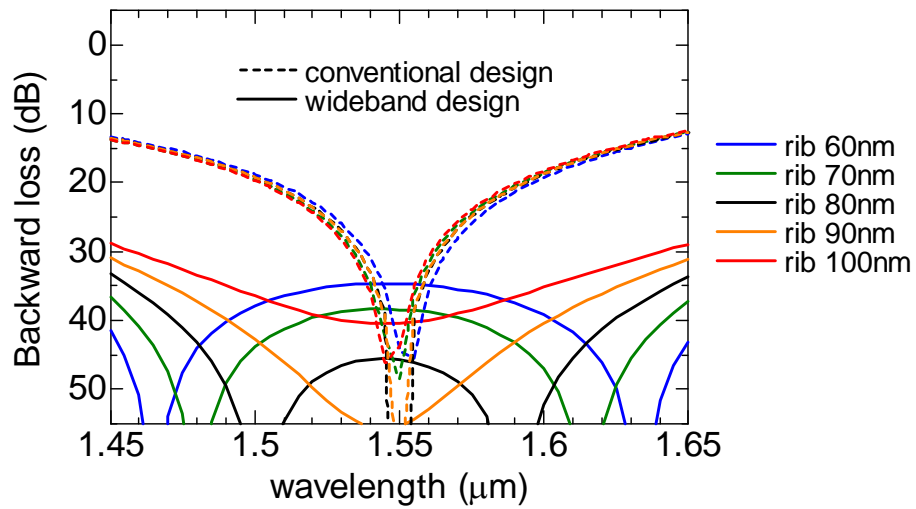


(b)

Fig. 4.12 Wavelength dependence of the type-1 isolator with errors in waveguide width, for (a) forward loss and (b) backward loss. The other waveguide parameters are fixed at the designs shown in Table 4.2.

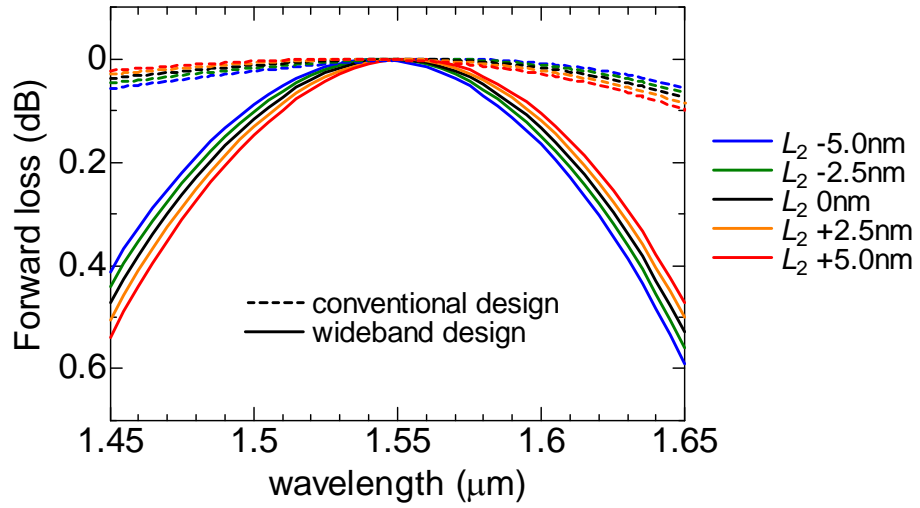


(a)

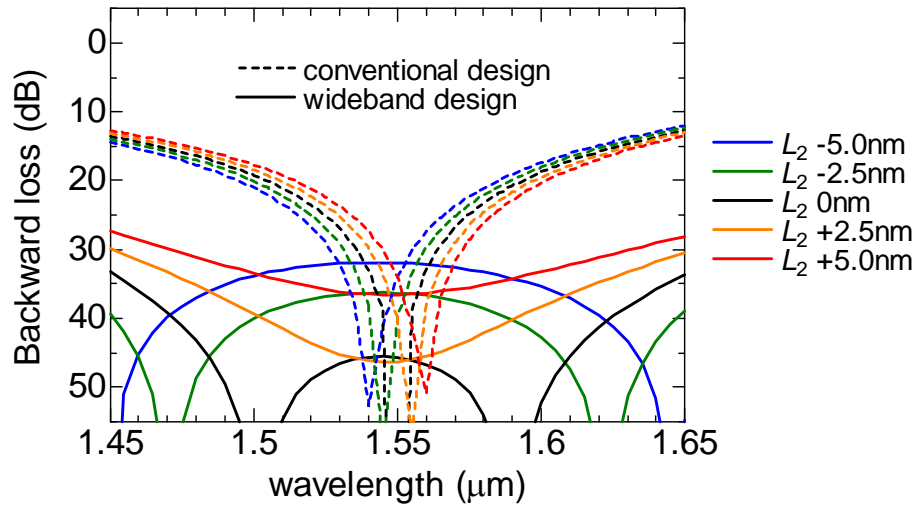


(b)

Fig. 4.13 Wavelength dependence of the type-1 isolator with errors in rib height, for (a) forward loss and (b) backward loss. The other waveguide parameters are fixed at the designs shown in Table 4.2.



(a)



(b)

Fig. 4.14 Wavelength dependence of the type-1 isolator with errors in length of one arm, for (a) forward loss and (b) backward loss. The other waveguide parameters are fixed at the designs shown in Table 4.2.

4.3.3 Ultra-wideband design

In this section, the author investigates further widening the operation bandwidth using the proposed concept. The wideband design is based on a flat wavelength dependence of total phase difference in the backward direction. However, it is not completely flat as θ_N and θ_R have specific wavelength dependences. Typically, θ_N and θ_R are a convex and concave function as the considering wavelength range, respectively, as can be seen in Fig. 4.6. In order to realize further wideband operation, the wavelength dependence of θ_R is to be elaborately adjusted to that of θ_N .

The waveguide parameters of reciprocal phase shifter affect its wavelength dependence as follows. Wider waveguide has larger propagation constant at the shorter wavelength due to highly optical confinement into the waveguide core. The wavelength dependence of the propagation constant is as shown in Fig. 4.15 (a). The difference between β_1 and β_2 is large at the shorter wavelength and is convex as shown in Fig. 4.15 (b). When the section lengths L_1 and L_2 are equal, the phase difference between two sections exhibits the convex wavelength dependence and its curve is multiplied by the length as shown in Fig. 4.15 (c). When the section length L_2 is increased for a fixed L_1 , w_1 , and w_2 , the wavelength dependence of the phase difference changes as shown in Fig. 4.15 (d). The reason is that the phase difference of the elongated section is affected only by β_2 , and has a concave wavelength dependence.

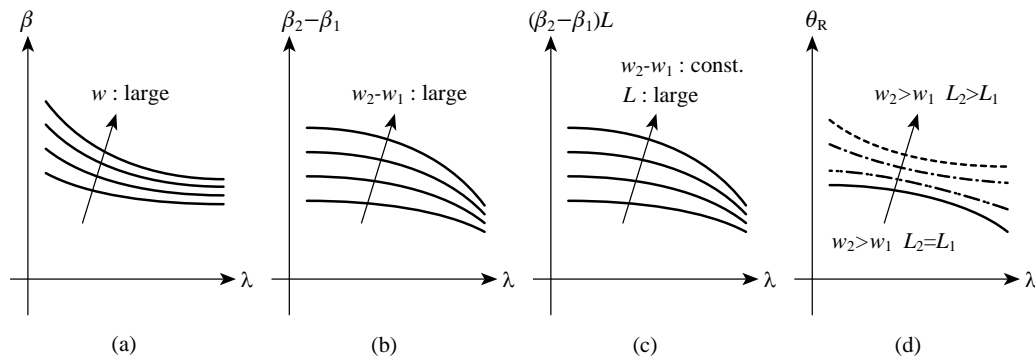


Fig. 4.15 Wavelength dependence of (a) propagation constant as a parameter of waveguide width, (b) the difference in propagation constant $\beta_2 - \beta_1$, (c) the phase difference provided by $(\beta_2 - \beta_1)L$ as a parameter of the section length, and (d) variation of reciprocal phase difference

$$\theta_R = \beta_2 L_2 - \beta_1 L_1 \text{ as a parameter of the difference in section length.}$$

Based on such a behavior, we design a magneto-optical isolator operating in an ultra-wideband range from 1.31 μm to 1.55 μm . Two extinction peaks where the backward phase difference corresponds to π are adjusted to 1.31 μm and 1.55 μm . The center wavelength is to be chosen properly to minimize the forward loss at the band edges and to provide sufficient backward loss in a desired wavelength range. In this design, we set the center wavelength at 1.43 μm .

A rib waveguide formed on a Ce:YIG film grown on a SGGG substrate and covered by SiO_2 upper layer is assumed. The waveguide and rib heights are 0.48 μm and 0.08 μm , respectively, that is the same as type-1 isolator treated thus far. We set the waveguide width w_1 at 2.0 μm and modify the width w_2 from 2.4 μm to 3.0 μm . Fig. 4.16 shows the reciprocal phase difference θ_R of $w_1=2.0$ μm and $w_2=2.4$ μm with a parameter of section lengths where L_2 is slightly modified from L_1 so that the $-\theta_N+\theta_R$ becomes $+\pi$ at $\lambda=1.55$ μm . Table 4.3 shows the optimized lengths L_1 and L_2 so as to have two extinction peaks at $\lambda=1.31$ μm and 1.55 μm . Fig. 4.17 shows the nonreciprocal and reciprocal phase differences for several combinations of waveguide width. In this case, the combination of the waveguide widths with larger difference shows similar wavelength dependence of θ_R to that of θ_N . This realizes higher backward loss in a wide wavelength range as shown in Fig. 4.18. In the ultra-wideband design with the waveguide widths of $w_1=2.0$ μm and $w_2=3.0$ μm , the forward loss of <1.0 dB and the backward loss of >26 dB is obtained at the wavelength range of 1.25 – 1.60 μm .

Table 4.3 Optimized waveguide parameters of reciprocal phase shifter.

w_1 (μm)	w_2 (μm)	L_1 (μm)	L_2 (μm)
2.0	2.4	1900	1898.453
2.0	2.6	880	879.178
2.0	2.8	510	509.548
2.0	3.0	360	359.714

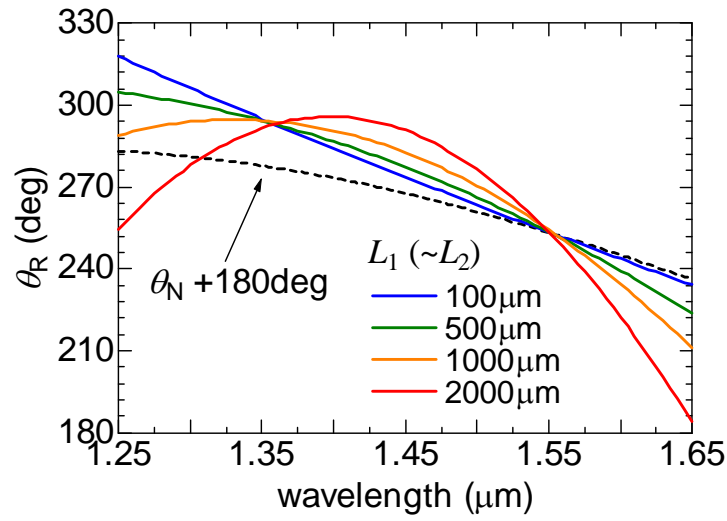


Fig. 4.16 Reciprocal phase difference for fixed waveguide width $w_1 = 2.0 \mu\text{m}$ and $w_2 = 2.4 \mu\text{m}$ with a parameter of section lengths where L_2 is slightly modified from L_1 so that the $-\theta_N + \theta_R$ becomes $+\pi$ at $\lambda = 1.55 \mu\text{m}$.

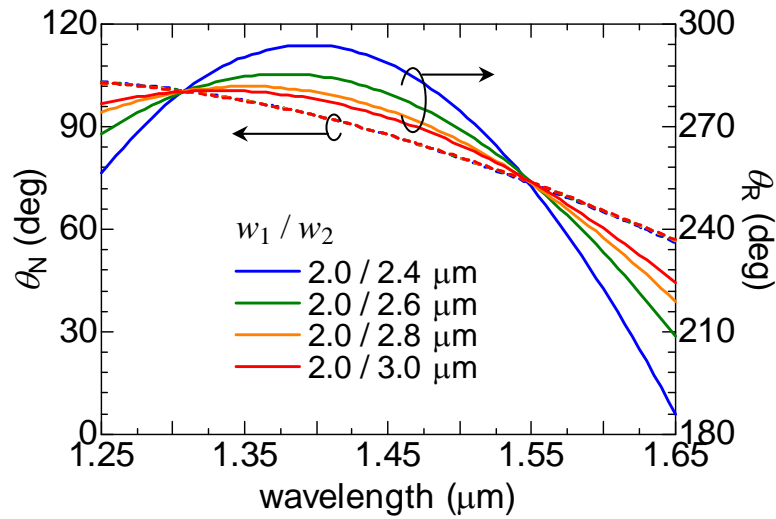


Fig. 4.17 Phase differences in the ultra-wideband design with several combinations of the waveguide width.

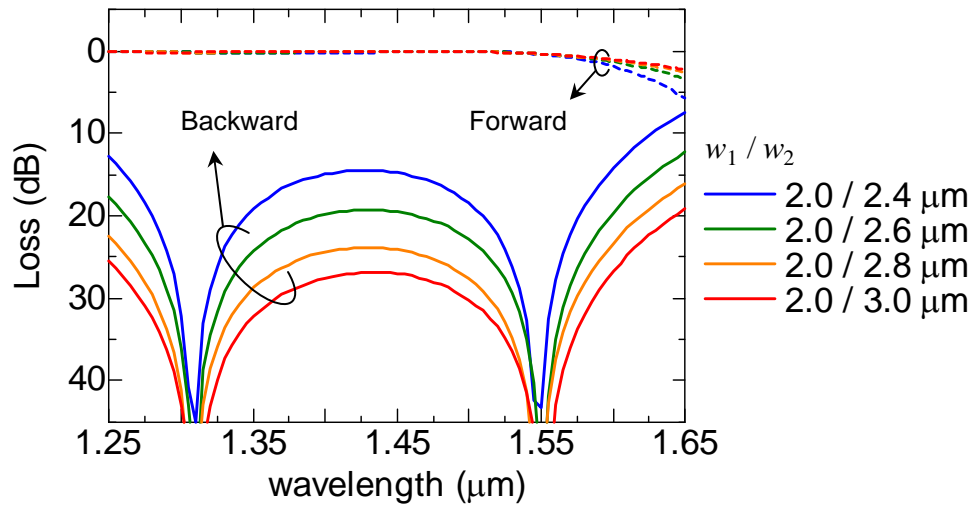


Fig. 4.18 Wavelength dependence of forward and backward losses in the ultra-wideband designs.

4.4 Fabrication of a wideband isolator

We fabricate a wideband isolator with the type-1 structure described above. A 0.48- μm -thick Ce:YIG film is grown on a (111)-oriented $(\text{GdCa})_3(\text{GaMgZr})_5\text{O}_{12}$ (SGGG) substrate by a radio frequency (RF) sputtering epitaxy with the substrate temperature at 670 °C. Argon containing oxygen at a volume ratio of 0.28% is used as the sputter gas. After the growth, the film is covered by ~300-nm-thick SiO_2 which protects the film surface during the following procedures. A post-annealing process at a temperature of 800 °C for 30 min is employed to reduce the propagation loss of the Ce:YIG film [12,13]. After coating 400-nm-thick electron-beam resist OE8R-1000 on the sample surface by a spin coater with 4000 rpm for 40 sec, it is baked at 180 °C for 30 min. ~30-nm-thick Al is coated on it to increase the conductivity of electron-beam. The waveguide patterns are exposed by e-beam lithography with accelerating voltage of 50 kV and are developed with a mixture of methyl isobutyl ketone and isopropanol (1:1) for 1 min. The patterns are transferred to a Ti mask formed by e-beam deposition, which is lifted off with acetone. After reactive ion etching in a CHF_3 plasma for SiO_2 etching, the rib waveguide is formed on Ce:YIG surface by Ar sputter etching with a 100-W RF power. The Ti mask is removed by a mixture of sodium hydroxide and hydrogen peroxide (1:1) at ~100 °C. Then SiO_2 is deposited on the whole surface of the

fabricated waveguide. Finally, the ends of the waveguide are obtained by cleaving at a notch formed by dicing-saw.

Here, we utilize a concept of ultra-wideband design to realize wider bandwidth. That is, the curve of the wavelength dependence is considered in the design although it is focused on the performance improvement in the wavelength around 1.55 μm . In this case, it is designed with the propagation constants β_1 , β_2 , and the nonreciprocal phase shift calculated by solving an eigenvalue equation of four layered structure approximated from the 2-D waveguide structure. The waveguide height is set at 0.48 μm to maximize the nonreciprocal phase shift and the rib height is set at 0.08 μm . The designed lengths of the modified waveguide widths $w_1 = 2.0 \mu\text{m}$ and $w_2 = 2.4 \mu\text{m}$ are $L_1 = 900 \mu\text{m}$ and $L_2 = 899.55 \mu\text{m}$, respectively. Tapered waveguides which connect the modified section are installed in both arms to avoid the imbalance between the two arms such as excess loss and phase shift associated with the taper. The designed forward and backward losses are indicated by red lines in Fig. 4.19. We also calculate these losses with the designed parameter by using a mode solver of FEM and the perturbation theory to obtain the nonreciprocal phase shift as shown in Fig. 4.20. There is a difference in the optimum design between the calculation methods especially when the section lengths are large.

A 0.5-mm-long and 24- μm -wide multi-mode interference (MMI) coupler is designed for the 3dB coupler. The two MZI arms are formed 300 μm away from each other, sufficient to apply an external magnetic field in anti-parallel directions, by 5-degree bending waveguides of 3.0-mm-radius. The total length of the waveguide is ~6.0 mm, which includes 0.75- μm -wide down-taper waveguides at input and output ends to increase the coupling efficiency into connecting fibers. In order to confirm the wideband operation, two magneto-optical isolators with the conventional and wideband designs are fabricated using these waveguide components on a sample.

Fig. 4.21 shows the photo image of the fabricated sample from the top view. Fig. 4.22 shows the SEM image of cross section of the fabricated waveguide facets which is the end of the 0.75- μm -wide down-taper waveguide. The rib height of the fabricated waveguide is observed to be 60 nm. The calculated operation spectra considering this error in rib height are

shown by the blue lines in Figs. 4.19 and 4.20. The extinction peaks shift to the longer wavelength.

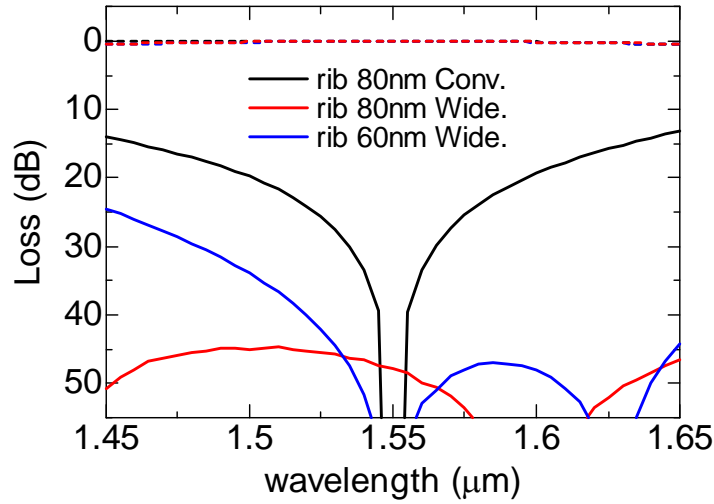


Fig. 4.19 Calculated operation spectra of magneto-optical isolator in the conventional and wideband designs by solving eigenvalue equation with approximated waveguide. Dashed and solid lines are forward and backward losses, respectively.

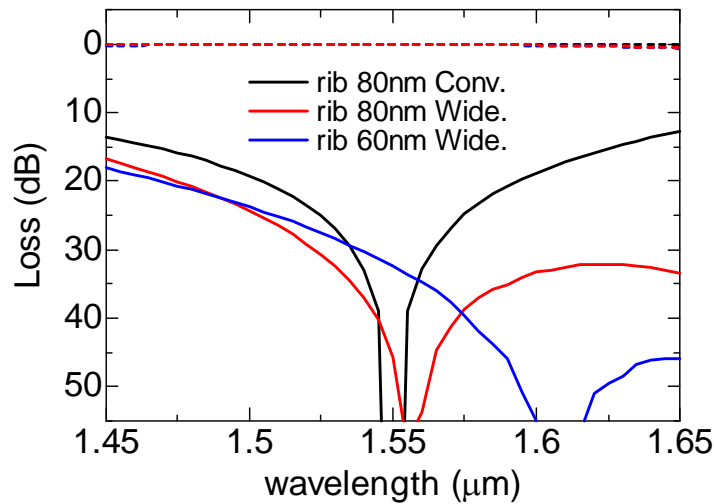


Fig. 4.20 Calculated operation spectra of magneto-optical isolator in the conventional and wideband designs by a mode solving of FEM and the perturbation theory. Dashed and solid lines are forward and backward losses, respectively.

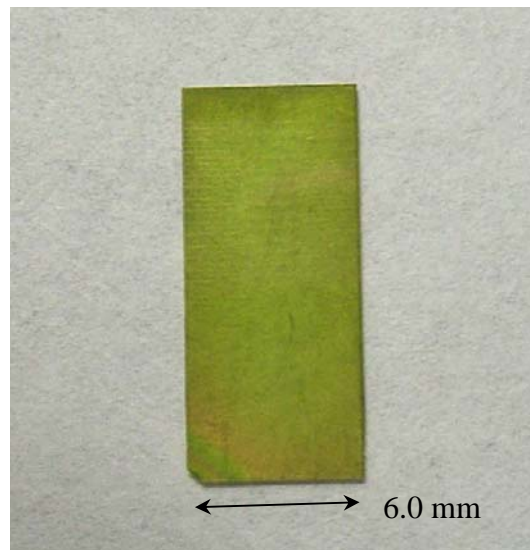


Fig. 4.21 Photo image of the fabricated sample on a Ce:YIG film.

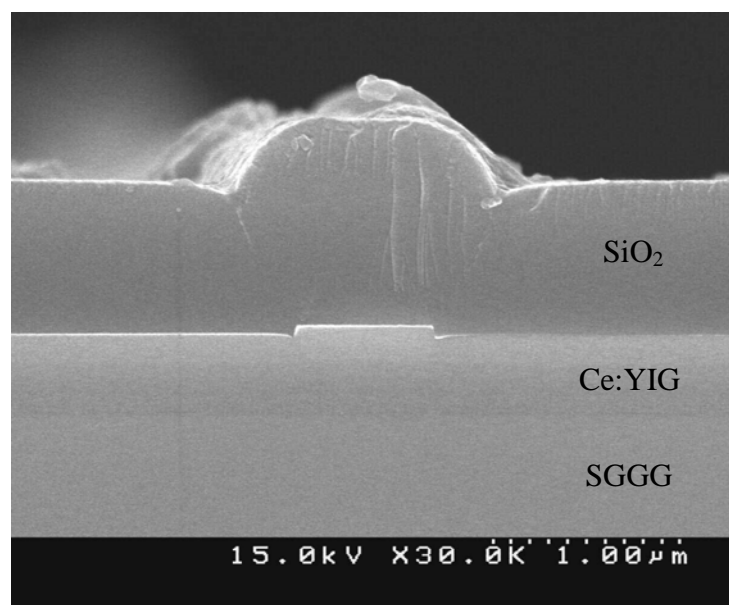


Fig. 4.22 SEM image of cross section of the fabricated waveguide on a Ce:YIG film.

4.5 Characterization

Optical measurement setup is shown in Fig. 4.23. Polarized light from an amplified spontaneous emission (ASE) diode having an optical gain in the wavelength range of $1.53 - 1.565 \mu\text{m}$ is launched into the waveguide facet with TM mode. First, near field pattern of the transmitted light is observed with infrared-camera. The light is propagating along clockwise (CW) direction. The sign of nonreciprocal phase difference is determined by a direction of the applied magnetic field. A permanent magnet with three poles is set on the waveguide to apply an external magnetic field in anti-parallel directions to obtain a nonreciprocal phase shift. Fig. 4.24 shows the observed near field patterns of the transmitted light which is interchanged between the center and side ports depending on the phase difference in the MZI arms. When the external magnetic field is applied to the MZI arms in parallel to the propagation direction, no nonreciprocal phase difference is induced between two arms. Inverse push-pull operations are observed in each design for respective poles of the permanent magnet. This behavior agrees with the operation principle as shown in Fig. 4.1.

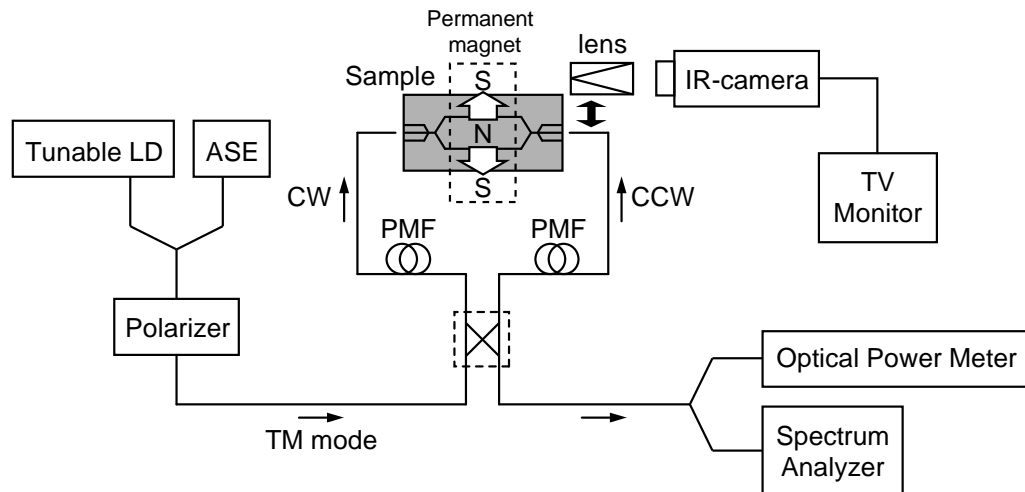


Fig. 4.23 Optical measurement setup for a magnet-optical isolator.

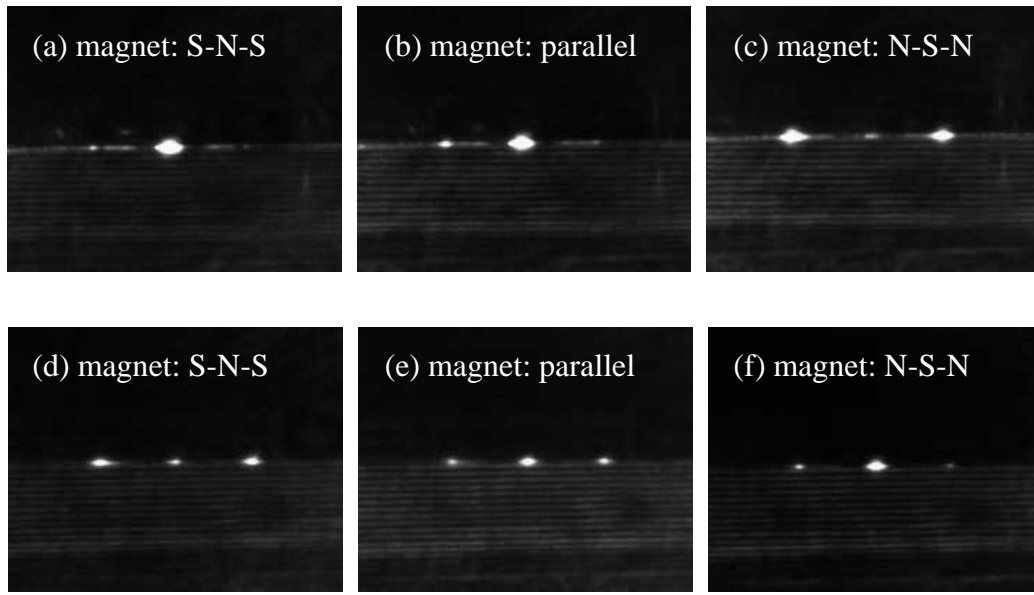
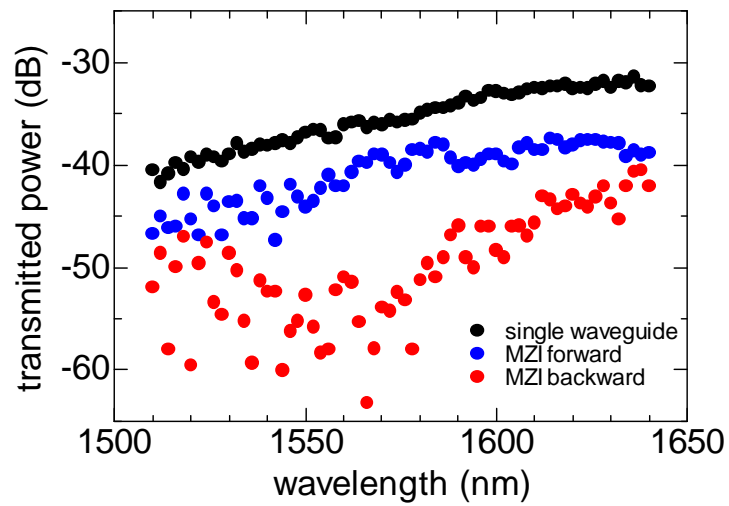


Fig. 4.24 Near field patterns of transmitted light with an ASE light source having an optical gain around $\lambda = 1.55 \mu\text{m}$. The isolators are fabricated with (a), (b), (c) conventional design and (d), (e), (f) wideband design on a sample. An external magnetic field is applied in parallel to the light propagation in (b) and (e).

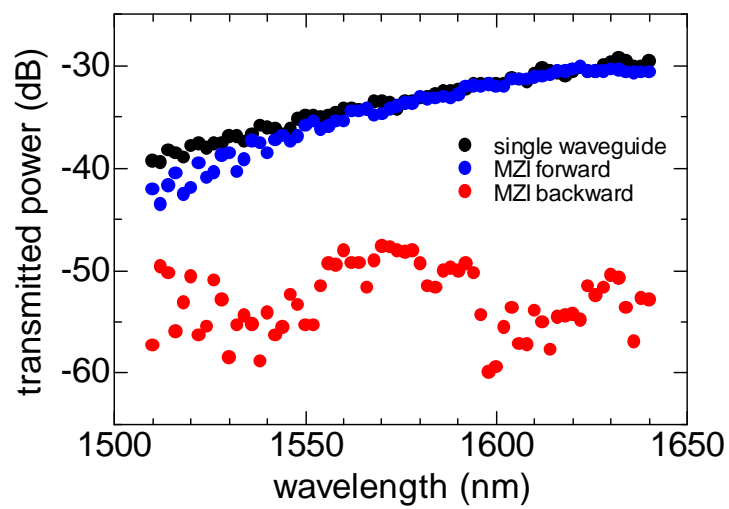
Next, fixing the permanent magnet, transmitted light from the center waveguide is coupled into another fiber. A tunable laser diode which has an operating wavelength range in $1.51 - 1.64 \mu\text{m}$ is used as the light source. Fig. 4.25 shows the transmitted power of the two isolators measured with an optical power monitor for light propagating in clockwise (CW) and counter-clockwise (CCW) directions. The forward loss corresponds to the case where larger power is transmitted to the center port, while the backward loss corresponds to the reversed direction with the fixed magnet. The propagation direction is reversed by interchanging the connection of the optical fiber. The transmission loss measured in a single waveguide fabricated beside the isolator on the sample is monotonically decreased from 40 dB at $\lambda = 1.51 \mu\text{m}$ to 31 dB at $\lambda = 1.64 \mu\text{m}$, which includes the waveguide propagation loss mainly dominated by the optical absorption of Ce:YIG and coupling loss of ~ 30 dB at two facets between fiber and waveguide. There is little difference in the transmitted power between the single waveguide and the forward propagation of isolator in wideband design,

which means that the excess loss of the fabricated MZI is small. Therefore, the insertion loss of the fabricated isolator except the coupling loss between fiber and waveguide is mainly dominated by the propagation loss of the waveguide and is estimated to be 6 dB at $\lambda = 1.55 \mu\text{m}$. The degradation of the forward loss in the conventional design is not due to the design but the accuracy of fabrication. That is, the coupling loss between the fiber and waveguide or the propagation loss of the waveguide is accidentally larger in the conventional design than that in the wideband design.

Figure 4.26 shows the transmission loss normalized with the transmittance of the single waveguide. The measured results agree with the calculated ones qualitatively though it is not as much as the calculation results. Generally, the extinction of a MZI is limited by the power imbalance as well as the deviation of phase difference between two arms. Also, the maximum sensitivity of the measurement setup is ~ 70 dB. The scattered data of the backward loss measured at the shorter wavelength region are due to the latter one. Therefore, the small extinction peak at $\lambda \sim 1.54 \mu\text{m}$ in Fig. 4.26 (b) may not correspond to the calculated peaks at $\lambda \sim 1.55 \mu\text{m}$ shown in Fig. 4.19. If so, the measured results agree rather well with the calculation results in Fig. 4.20. The difference in transmission loss between the forward and backward directions corresponds to the isolation ratio. Larger isolation ratio is obtained in a wider wavelength range in the wideband design. High isolation ratio of 15 – 25 dB is obtained in a wavelength range between $1.53 \mu\text{m}$ and $1.64 \mu\text{m}$ in the wideband isolator.

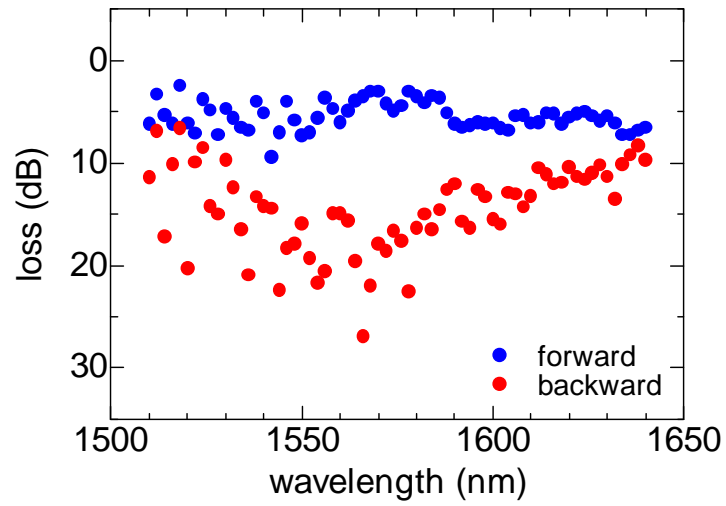


(a)

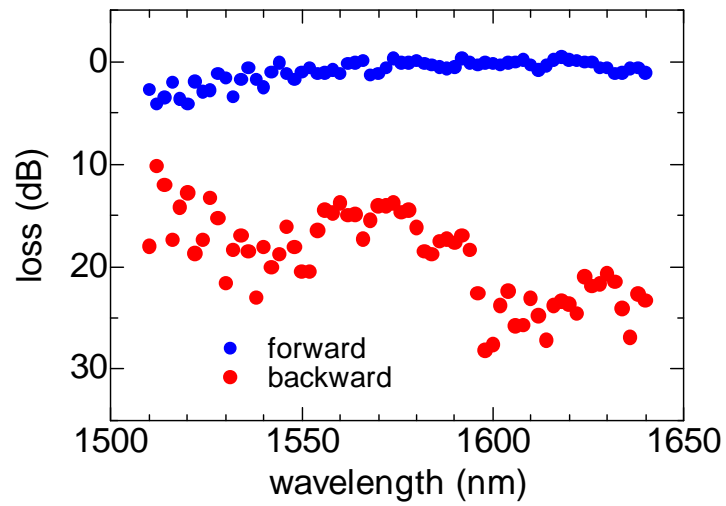


(b)

Fig. 4.25 Measured transmission of the fabricated isolator with (a) conventional design and (b) wideband design.



(a)



(b)

Fig. 4.26 Measured transmission of the fabricated isolator with (a) conventional design and (b) wideband design.

4.6 Discussion

In Section 4.5, a magneto-optical isolator with wideband design around $\lambda = 1.55 \mu\text{m}$ has been demonstrated on a Ce:YIG waveguide. It is difficult to control the nonreciprocal phase difference in the MZI composed of a magneto-optic waveguide because the external magnetic field is unfortunately applied to the bending waveguides which separate the two arms to be applied the magnetic fields in anti-parallel direction. In this measurement, we control the nonreciprocal phase difference by placing the permanent magnet with three poles properly. This problem is solved by using the magneto-optic material only in the nonreciprocal phase shifter such as type-2 or type-3 isolator.

We also design an ultra-wideband isolator operating in $1.31 \mu\text{m}$ and $1.55 \mu\text{m}$ on a Ce:YIG waveguide. However, it can not be demonstrated since the optical absorption loss of the Ce:YIG waveguide is large at the shorter wavelength. Fig. 4.27 shows the propagation loss of a Ce:YIG waveguide after post-annealing process measured by a cut-back method. The transmission losses through the several propagation lengths are measured with tunable laser sources having an operating wavelength range of $1.26 - 1.36 \mu\text{m}$ and $1.34 - 1.44 \mu\text{m}$ or an ASE source. The propagation loss is $\sim 1 \text{ dB/mm}$ at $\lambda = 1.55 \mu\text{m}$ but is $6 - 8 \text{ dB/mm}$ at $\lambda = 1.31 \mu\text{m}$ that is a serious problem for the magneto-optical isolator of the Ce:YIG waveguide. This can be circumvented by using the waveguide structure of type-2 or type-3 isolator. Since the Ce:YIG is used as an upper cladding layer, the absorption loss of a propagating light is greatly reduced. A magneto-optical isolator with the ultra-wideband design is to be demonstrated with such a waveguide structure.

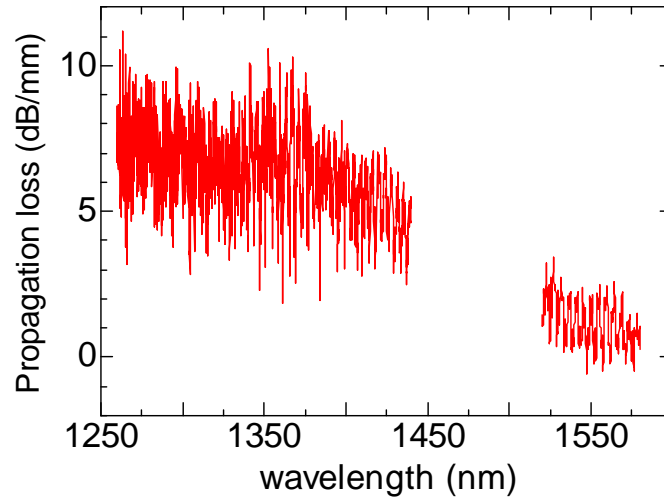


Fig. 4.27 Propagation loss of a Ce:YIG waveguide as a function of wavelength.

4.7 Summary

A wideband operation of a magneto-optical isolator employing nonreciprocal phase shift has been proposed and demonstrated. The wideband operation is realized by phase adjustment in the MZI to compensate the wavelength dependence of nonreciprocal phase shift for that of reciprocal one. First, we demonstrate a dramatic improvement of the backward loss with acceptably small deterioration of the forward loss by numerical calculations. This design concept is applicable to the isolator with any other material, structure, and dimension. Next, we fabricated a wideband isolator with Ce:YIG waveguide and demonstrate the wideband operation experimentally. High isolation ratio of 25 dB is successfully obtained at $\lambda = 1.60 \mu\text{m}$ owing to the wider operation spectrum.

Such wideband operation has never been reported in bulk isolators because it is difficult to control the wavelength dependence of the bulk materials. On the other hand, a waveguide structure has many controllable parameters as mention above.

References

- [1] K. Ando, T. Okoshi, and N. Koshizuka, "Waveguide magneto-optic isolator fabricated by laser annealing," *Appl. Phys. Lett.*, vol.53, pp.4-6 (1988).
- [2] T. Shintaku, "Integrated optical isolator based on efficient nonreciprocal radiation mode conversion," *Appl. Phys. Lett.*, vol.73, pp.1946-1948 (1998).
- [3] F. Auracher and H. H. Witte, "A new design for an integrated optical isolator," *Opt. Commun.*, vol.13, pp.435-438 (1975).
- [4] T. Mizumoto and Y. Naito, "Nonreciprocal propagation characteristics of YIG thin film," *IEEE Trans. on Microwave Theory and Technique*, vol.MTT-30, pp.922-925 (1982).
- [5] Y. Okamura, T. Negami, and S. Yamamoto, "Integrated optical isolator and circulator using nonreciprocal phase shifters: a proposal," *Appl. Opt.*, vol.23, pp.1886-1889 (1984).
- [6] N. Bahlmann, M. Lohmeyer, H. Dötsch, and P. Hertel, "Integrated magneto-optic Mach-Zehnder interferometer isolator for TE modes," *Electron. Lett.*, vol.34, pp.2122-2123 (1998).
- [7] J. Fujita, M. Levy, and R. M. Osgood, Jr., "Waveguide optical isolator based on Mach-Zehnder interferometer," *Appl. Phys. Lett.*, vol.76, pp.2158-2160 (2000).
- [8] H. Yokoi and T. Mizumoto, "Proposed configuration of integrated optical isolator employing wafer-direct bonding technique," *Electron. Lett.*, vol.33, pp.1787-1788 (1997).
- [9] H. Yokoi, T. Mizumoto, and Y. Shoji, "Optical nonreciprocal devices with a silicon guiding layer fabricated by wafer bonding," *Appl. Opt.*, vol.42, pp.6605-6612 (2003).
- [10] R. L. Espinola, T. Izuhara, M.-C. Tsai, and R. M. Osgood, Jr., "Magneto-optical nonreciprocal phase shift in garnet/silicon-on-insulator waveguides," *Opt. Lett.*, vol.29, pp.941-943 (2004).
- [11] M. Gomi, H. Furuyama, and M. Abe, "Strong magneto-optical enhancement in highly Ce-substituted iron garnet films prepared by sputtering," *J. Appl. Phys.*, vol.70, pp.7065-7067 (1991).
- [12] T. Shintaku and T. Uno, "Preparation of Ce-substituted yttrium iron garnet films for magneto-optic waveguide devices," *Jpn. J. Appl. Phys.* Vol.35, pp.4689-4691 (1996).
- [13] S. Narikawa, "Semi-leaky isolator using a direct bonding of $\text{LiNbO}_3/\text{Ce:YIG}$," (Master thesis of Tokyo Institute of Technology, Tokyo, 2003), Chap.4, p.34. (in Japanese.)
- [14] S. H. Wemple and W. J. Tabor, "Refractive index behavior of garnets," *J. Appl. Phys.*, vol.44,

pp.1395-1396 (1973).

[15] K. Iga, "Semiconductor laser," (Japan Society of Applied Physics, Tokyo, 1994), Chap.2,
pp.32-44. (in Japanese.)

[16] FemSIM software from RSoft Design Group, (<http://www.rsoftdesign.com/>)

Chapter 5:

Polarization-Independent Magneto-Optical Isolator Using TM-Mode Nonreciprocal Phase Shift

5.1 Introduction

In high-speed optical fiber communication systems, magneto-optical isolators are indispensable in protecting optical active devices from unwanted reflected lights. Especially in highly developed optical fiber amplification systems, polarization-independent optical isolators are strongly desired. At present, the polarization-independent isolators are widely used in commercial systems [1]. However, there is no waveguide isolator operating even for one polarization in commercial systems.

The waveguide isolator investigated in this study is employing nonreciprocal phase shift normally induced in TM mode with a thin-film magneto-optic waveguide. The essence of the nonreciprocal phase shift is based on the asymmetry of waveguide-layer structure with respect to the direction of the electromagnetic field of the guided mode. In order to obtain a nonreciprocal phase shift for a TE mode, a waveguide must be configured so as to have horizontal asymmetry; typically, this is an asymmetry structure that is more difficult to realize. Polarization-independent waveguide isolators that employ a nonreciprocal phase shift have been proposed by two researchers. Zhuromskyy *et al.* [2] used horizontal and vertical domain walls in the magneto-optic guiding layer, and Fujita *et al.* [3] used different side cladding layer in order to simultaneously induce nonreciprocal phase shifts for the TE and TM modes. Other configurations for a polarization-independent operation of a waveguide optical isolator based on Faraday rotation have also been proposed [4,5].

In this chapter, the author proposes a polarization-independent isolator using nonreciprocal phase shift only for the TM mode. This device is a Mach-Zehnder interferometer (MZI) with polarization converters and nonreciprocal phase shifters. The operation is realized not by a polarization-diversity scheme but by the phase differences between reciprocal TE and nonreciprocal TM modes. This configuration not only obviates the need for a nonreciprocal phase shift for both modes but also makes it possible to fabricate using an integrated structure, such as a semiconductor guiding layer, which we have investigated [6-8].

5.2 Principle of polarization-independent operation

Figure 5.1 shows a schematic configuration of the proposed optical isolator. The MZI has polarization converters (PC), nonreciprocal phase shifters (NPS), and an additional π phase shifter. All components are composed of planar waveguide structures; the nonreciprocal phase shifters utilize a magneto-optic material with an applied external field. Here, the polarization converters are assumed to give 100% polarization conversion between TE and TM modes, after which the lightwaves propagate in the nonreciprocal phase shifter of each arm, where each has a different polarization mode. The nonreciprocal phase shifters induce phase differences between the different modes as follows:

$$(\beta_{TE} - \beta_{TM+})L + \pi = 2m\pi \quad (5.1)$$

$$(\beta_{TE} - \beta_{TM-})L + \pi = (2n+1)\pi \quad (5.2)$$

where β_{TE} , β_{TM+} , and β_{TM-} denote the longitudinal propagation constants of the TE and the forward- and backward-traveling TM modes, respectively, and m and n are integers. Note that the second term of $+\pi$ in (5.1) and (5.2) is induced by a π phase shifter. As a result of the conditions in these two equations, the forward waves interfere constructively, and the backward waves interfere destructively in 3dB couplers. Since both input modes follow these relations, the MZI functions as a polarization-independent optical isolator.

Although the additional π phase shifter is not necessary for polarization-independent isolator operation, it makes backward loss keep high despite the inefficiency of the polarization converters. This property enables one to use a broader range of waveguide

polarization converters for this isolator application, which have been proposed and demonstrated [9-15] although it would be rather difficult to realize a truly $\sim 100\%$ mode conversion device. The performance of the isolator is summarized in Table 5.1 for four possible input combinations of forward/backward and TM/TE mode, where $m = n = 0$ are assumed for simplicity in (5.1) and (5.2). The polarization conversion efficiency is represented by η . Two rows in each case denote the waves that are divided into two arms of the interferometer, where the relative phase of each polarization component is indicated in brackets. The forward waves that are converted to the other mode from the input one as is desired, become in-phase and are transmitted to the output port. The unconverted components become anti-phase due to the additional π phase shift, and interfere destructively, which results in the insertion loss. The backward waves become antiphase whether any mode conversion is induced or not. That is, the design ensures that any backward traveling waves become antiphase despite an incomplete polarization conversion, which is favorable for the isolator performance.

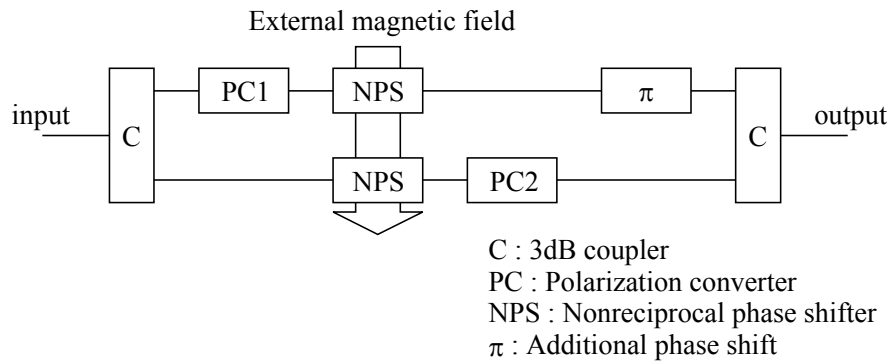


Fig. 5.1 Schematic diagram of the proposed polarization-independent optical isolator.

Table 5.1 Operation principle of polarization-independent optical isolator.

	3dB		PC1		NPS		PC2		π		3dB
TM	\rightarrow	TM [0]	\rightarrow	η TE [0] (1- η)TM [0]	\rightarrow	η TE [$\pi/2$] (1- η)TM [$-\pi/2$]	\rightarrow	η TE [$\pi/2$] (1- η)TM [$-\pi/2$]	\rightarrow	η TE [$3\pi/2$] (1- η)TM [$\pi/2$]	\rightarrow η TE
		TM [0]	\rightarrow	TM [0]	\rightarrow	TM [$-\pi/2$]	\rightarrow	η TE [$-\pi/2$] (1- η)TM [$-\pi/2$]	\rightarrow	η TE [$-\pi/2$] (1- η)TM [$-\pi/2$]	
TE	\rightarrow	TE [0]	\rightarrow	η TM [0] (1- η)TE [0]	\rightarrow	η TM [$-\pi/2$] (1- η)TE [$\pi/2$]	\rightarrow	η TM [$-\pi/2$] (1- η)TE [$\pi/2$]	\rightarrow	η TM [$\pi/2$] (1- η)TE [$3\pi/2$]	\rightarrow η TM
		TE [0]	\rightarrow	TE [0]	\rightarrow	TE [$\pi/2$]	\rightarrow	η TM [$\pi/2$] (1- η)TE [$\pi/2$]	\rightarrow	η TM [$\pi/2$] (1- η)TE [$\pi/2$]	
0	\leftarrow	η TE [$3\pi/2$] (1- η)TM [$3\pi/2$]	\leftarrow	TEM [$3\pi/2$]	\leftarrow	TM [π]	\leftarrow	TM [π]	\leftarrow	TM [0]	\leftarrow TM
		η TE [$\pi/2$] (1- η)TM [$\pi/2$]	\leftarrow	η TE [$\pi/2$] (1- η)TM [$\pi/2$]	\leftarrow	η TE [0] (1- η)TM [0]	\leftarrow	TM [0]	\leftarrow	TM [0]	
0	\leftarrow	η TM [$3\pi/2$] (1- η)TE [$3\pi/2$]	\leftarrow	TE [$3\pi/2$]	\leftarrow	TE [π]	\leftarrow	TE [π]	\leftarrow	TE [0]	\leftarrow TE
		η TM [$\pi/2$] (1- η)TE [$\pi/2$]	\leftarrow	η TM [$\pi/2$] (1- η)TE [$\pi/2$]	\leftarrow	η TM [0] (1- η)TE [0]	\leftarrow	TE [0]	\leftarrow	TE [0]	

5.3 Device structure

The author shows two examples of the device structure that realize the proposed isolator configuration as is shown in Fig. 5.1. For both devices, a magneto-optic garnet $\text{CeY}_2\text{Fe}_5\text{O}_{12}$ (Ce:YIG) that has a large Faraday rotation coefficient of -4500 deg/cm at 1.55 μm is grown on a (Ca, Mg, Zr) doped GGG substrate [16]. The type-1 isolator that is shown in Fig. 5.2 has a Ce:YIG guiding layer and a SiO_2 cover layer. The type-2 isolator, which is shown in Fig. 5.3, has a Si waveguide that is fabricated on a silicon-on-insulator (SOI) wafer and a Ce:YIG upper cladding layer, which is realized with a direct bonding technique [6-8]. An external magnetic field is transversely applied to the propagation direction and is parallel to the film plane to obtain a nonreciprocal phase shift only for TM mode.

The polarization converters have an asymmetric waveguide structure that realizes a passive polarization conversion. The isolators of type-1 and type-2 are assumed to have a periodic loaded waveguide [9] and an angled facet waveguide [10,11,15], respectively.

The additional reciprocal phase shift, which must be an odd multiple of π for both TE and TM modes, is realized by installing an optical path difference between two interferometer

arms. Another alternative is to employ 2×2 couplers for the MZI and to use its straight-through ports since they divide an input wave into antiphase waves.

In the following design, the operating wavelength is assumed to be $\sim 1.55 \mu\text{m}$.

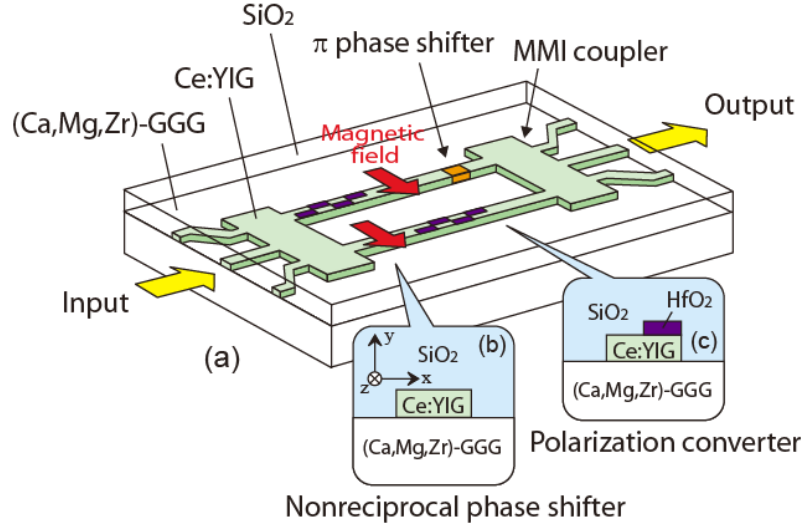


Fig. 5.2 Device structure of a polarization-independent isolator composed of a magneto-optic guiding layer (type-1).

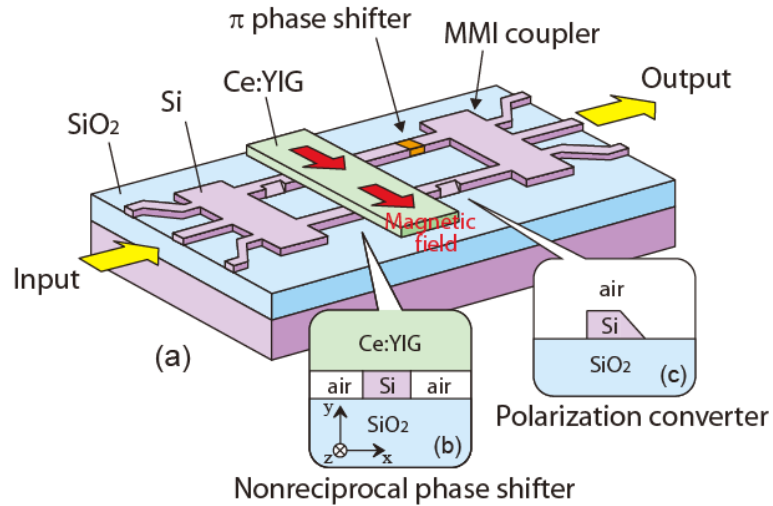


Fig. 5.3 Device structure of a polarization-independent isolator composed of a Si waveguide based on SOI structure (type-2).

5.4 Design of nonreciprocal phase shifter

The cross-sectional images of the nonreciprocal phase shifter are shown in Fig. 5.2 (b) and Fig. 5.3 (b). Here, the refractive indices of Ce:YIG, (Ca,Mg,Zr)-GGG, Si, SiO₂, and air are set at 2.20, 1.94, 3.48, 1.44, and 1.0 at a wavelength of 1.55 μm , respectively. The nonreciprocal phase shift $\Delta\beta$ ($= \beta_{\text{TM}+} - \beta_{\text{TM}-}$) is calculated based on the perturbation theory together with a mode solver of beam propagation method (BPM) [17] as described in Chapter 2. Fig. 5.4 shows the calculated nonreciprocal phase shift as a function of waveguide thickness. The waveguide widths are assumed to be 2.0 μm and 1.0 μm for type-1 and type-2 structures, respectively. The nonreciprocal phase shifts are maximized at small film thickness. A large nonreciprocal phase shift means a small propagation length L in (5.1) and (5.2). In the following discussion, the thickness of the waveguide core is fixed at 0.5 and 0.2 μm for the type-1 and type-2 isolators, respectively.

The nonreciprocal phase shifter is designed as a function of the waveguide width. Figure 5.5 (a) shows the width-dependent effective refractive indices of the TE and TM modes that are calculated by BPM for the type-1 isolator. The nonreciprocal propagation constants of the TM mode are estimated by adding and subtracting $\Delta\beta/2$ to the unperturbed propagation constant. Upon subtracting (5.2) from (5.1), the minimum propagation length L can be obtained by setting $m = n$. Figure 5.5 (b) shows the nonreciprocal phase shifts for the TM mode and the minimum required propagation lengths as a function of the waveguide width.

By using these parameters, the output powers of the MZI are calculated from the left-hand side of (5.1) and (5.2) (see the dashed and solid lines in Fig. 5.5 (c), where the 3 dB couplers and polarization converters are assumed to ideally function). When one term becomes 1 and the other becomes 0 at a particular waveguide width, (5.1) and (5.2) are satisfied, and the MZI functions as a polarization-independent isolator. For example, the type-1 isolator is designed for a guiding layer thickness of 0.5 μm at a width of 3.5, 2.6, 2.25 μm , and so on. On the other hand, at a width of 2.98, 2.38, and 2.14 μm , an optical isolator operation is obtained by reversing the direction of the external magnetic field.

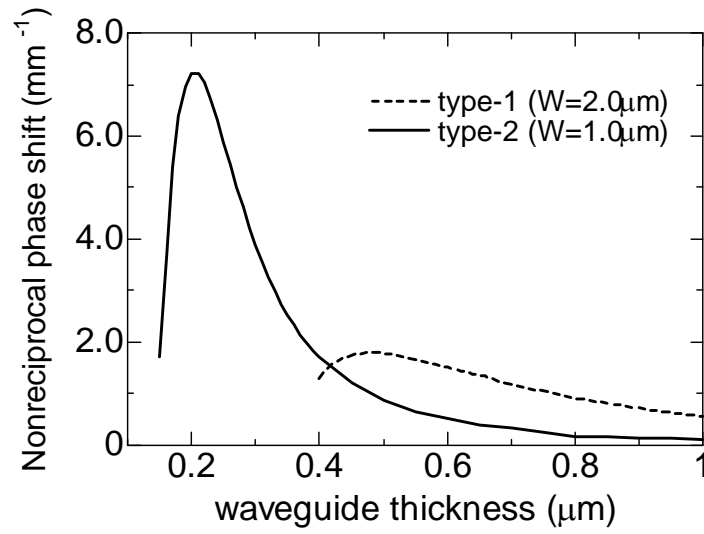


Fig. 5.4 Calculated nonreciprocal phase shift as a function of the waveguide thickness.

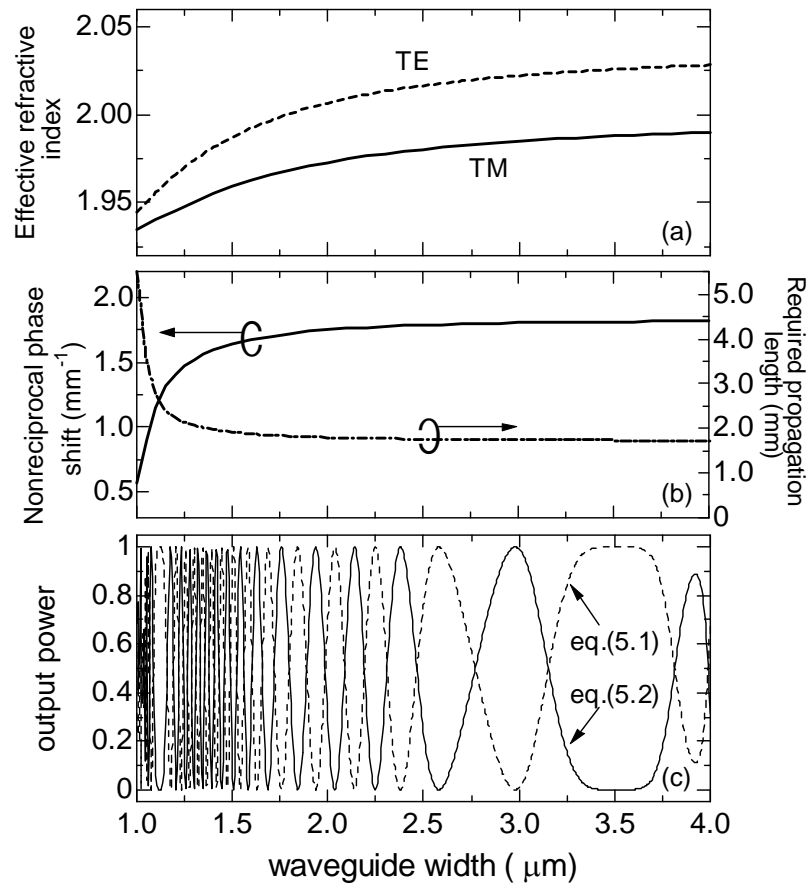


Fig. 5.5 (a) Calculated effective refractive indices, (b) nonreciprocal phase shift and required propagation length, and (c) output power of the MZI for type-1 isolator at a waveguide thickness of 0.5 μm .

In the same way, the type-2 isolator is designed as shown in Fig. 5.6 (a) – (c). For a guiding layer thickness of $0.2\ \mu\text{m}$, the designed widths are 2.05 , 1.6 , and $0.9\ \mu\text{m}$, or for the reverse propagation direction, they are at 2.4 , $1.5\ \mu\text{m}$, and so on. It should be noted that the fabrication tolerance for the width of the MZI is higher for wider waveguides in both material systems.

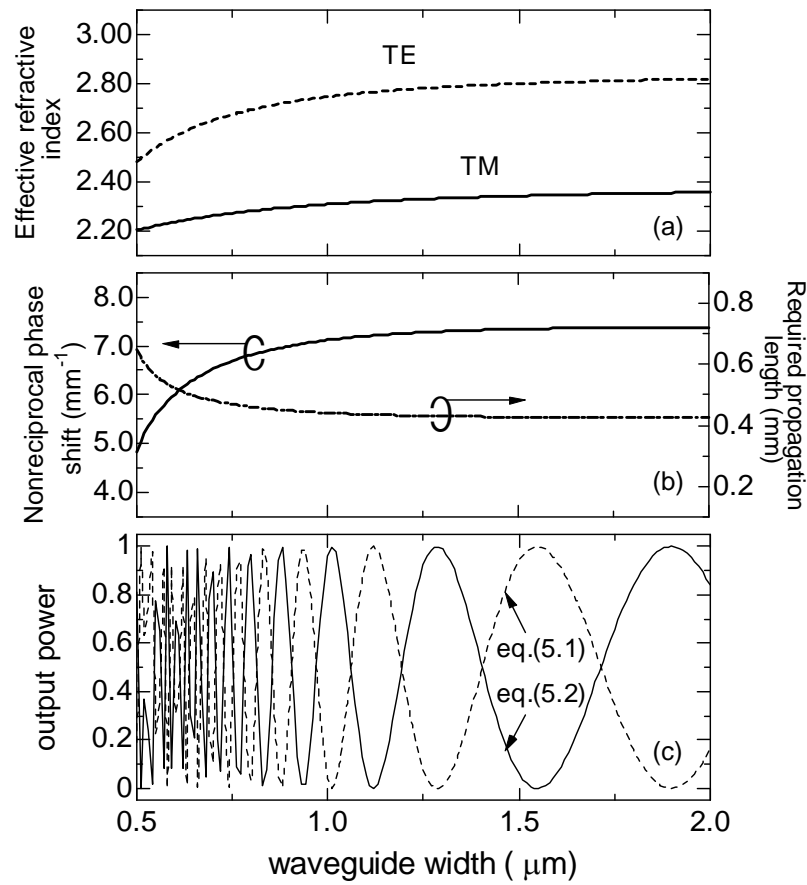


Fig. 5.6 (a) calculated effective refractive indices, (b) nonreciprocal phase shift and required propagation length, and (c) output power of the MZI for type-2 isolator at a waveguide thickness of $0.2\ \mu\text{m}$.

The operation spectrum of this device is determined by the difference in the wavelength dependences of the propagation constants for the two orthogonal modes $\beta_{TE}(\lambda)$ and $\beta_{TM}(\lambda)$; that is, the phase difference is based on $(\beta_{TE}(\lambda) - \beta_{TM}(\lambda))$. The nonreciprocal phase shifter is designed for fixed waveguide thickness. The designed waveguides have different wavelength dependences for $\beta_{TE}(\lambda)$ and $\beta_{TM}(\lambda)$.

Figure 5.7 shows the schematic image of the wavelength dependence of the calculated quantity $(\beta_{TE}(\lambda) - \beta_{TM}(\lambda))$. Here, we calculated the wavelength dependences of propagation constants considering the wavelength dispersion of the refractive indices using the same assumption in Section 4.3.1. For a fixed thickness, the widest operation bandwidth around the center wavelength (λ_C) is found at a specific width in case of Fig. 5.7 (b). Figure 5.8 shows the calculated wavelength dependence of the type-2 isolator for 0.25- μm -thick Si layer with several waveguide widths. In this case, (b) shows the widest operation bandwidth in a wavelength range from 1.53 to 1.565 μm (C-band). So, the waveguide width is optimized at 0.86 μm for 0.25- μm -thick Si layer.

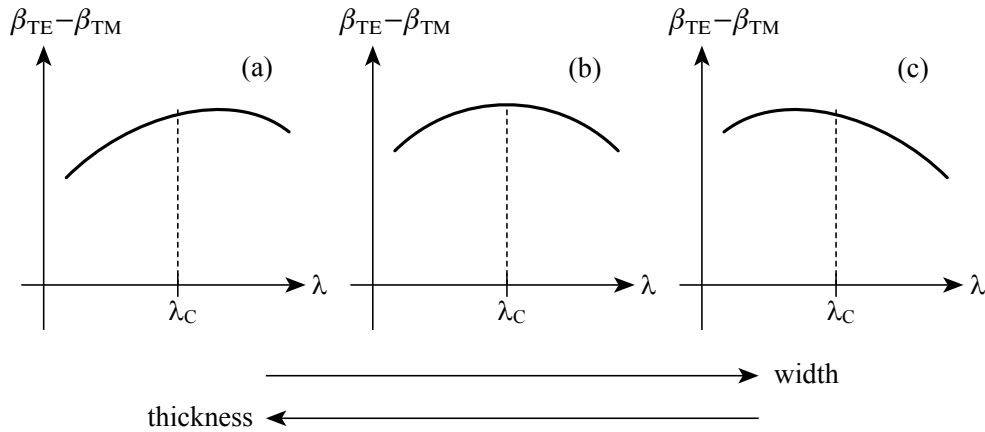


Fig. 5.7 Schematic wavelength dependence of the difference between β_{TE} and β_{TM} .

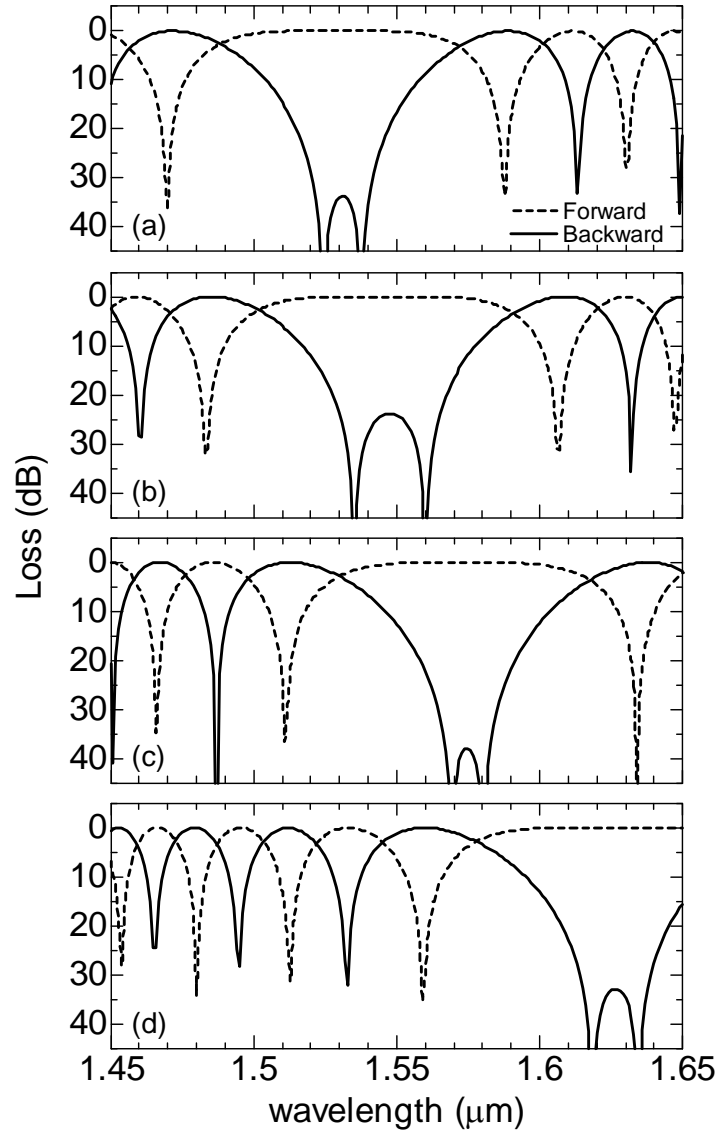


Fig. 5.8 Calculated wavelength dependence of the type-2 isolator. The height of Si waveguide is set at $0.25\mu\text{m}$. The widths and the lengths of nonreciprocal phase shifter are (a) $w = 0.80\mu\text{m}$ and $L = 551.6\mu\text{m}$, (b) $w = 0.86\mu\text{m}$ and $L = 543.9\mu\text{m}$, (c) $w = 1.0\mu\text{m}$ and $L = 538.1\mu\text{m}$, and (d) $w = 2.0\mu\text{m}$ and $L = 524.0\mu\text{m}$, respectively.

The combination of the guiding layer thickness and width at which the operation bandwidth becomes the largest in C-band is plotted in Figs. 5.9 and 5.10 for type-1 and type-2 isolators, respectively. The similar operational bandwidths, from 1.53 to 1.565 μm , are obtained for these parameter combinations. All designs are calculated for the TE and TM fundamental modes. However, higher order modes may be excited at the polarization converters when the waveguide width and/or height are large. The boundaries of a single-mode operation for the TE and TM modes are drawn by solid lines in the figures.

In actual fabrication, thickness can be controlled more precisely than width. The performance is less sensitive to width error for a wider waveguide, as shown in Figs. 5.5 (c) and 5.6 (c). Consequently, the thicknesses and widths of the preferred design that provides wide bandwidth and single-mode operation are 0.66 and 1.8 μm for a type-1 isolator and 0.26 and 0.72 μm for a type-2 isolator, respectively. The required propagation lengths are 2448.2 and 600.9 μm for type-1 and -2, respectively. Figures 5.11 and 5.12 show the calculated spectral response of these designs, where any propagation and coupling losses at 3 dB couplers are ignored. In addition, the wavelength dependences of the 3 dB couplers and the polarization converters are ignored because they are much less wavelength-sensitive than the phase shifters [15]. The isolation ratios and the insertion losses in the C-band wavelength range are >32 dB and <0.006 dB for the type-1 isolator and >21 dB and <0.034 dB for the type-2 isolator, respectively.

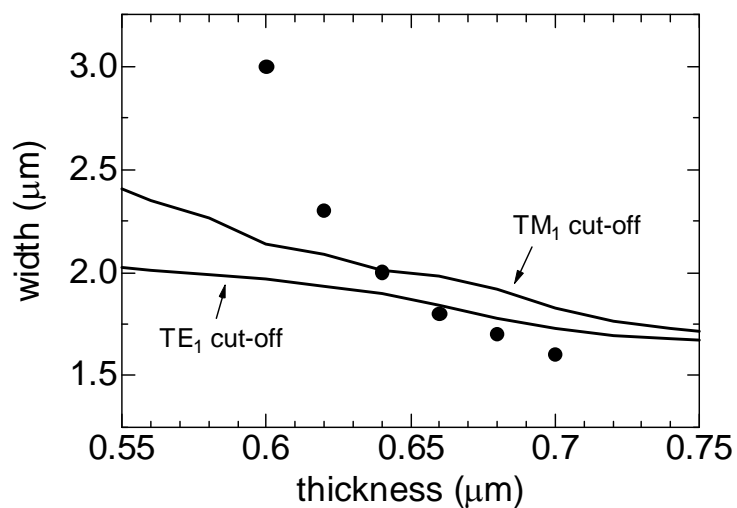


Fig. 5.9 Designed waveguide thicknesses and widths to obtain wide operation bandwidth in type-1 isolator.

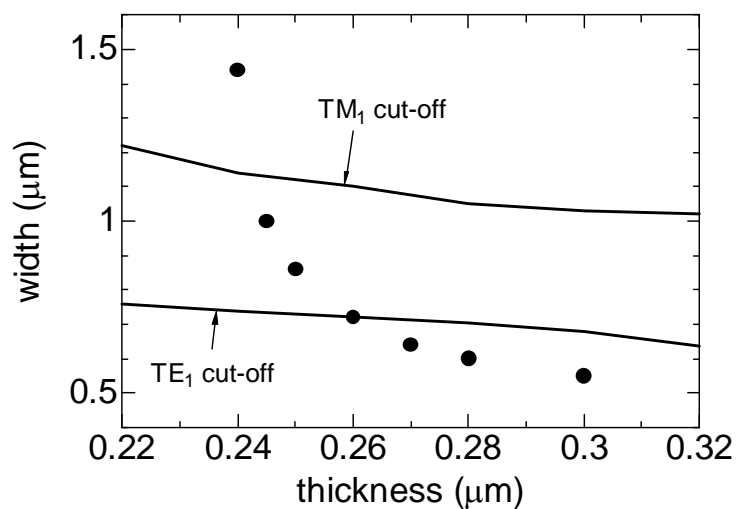


Fig. 5.10 Designed waveguide thicknesses and widths to obtain wide operation bandwidth in type-2 isolator.

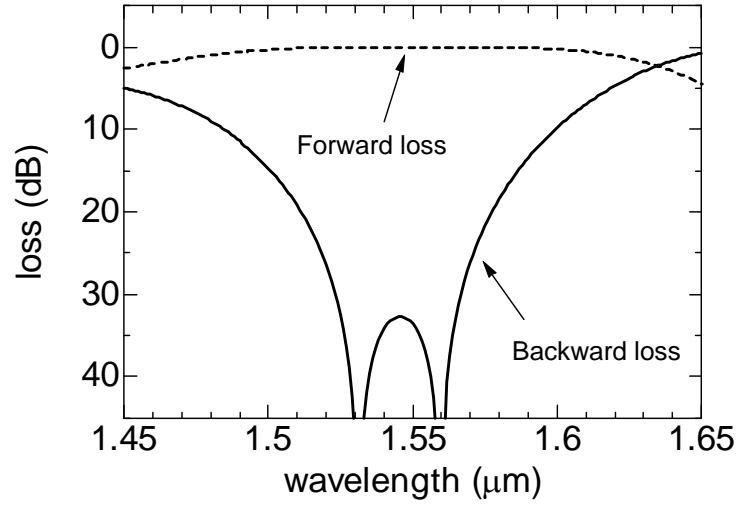


Fig. 5.11 Calculated spectral response of type-1 isolator, where the waveguide thickness is $0.66 \mu\text{m}$ and the width is $1.8 \mu\text{m}$.

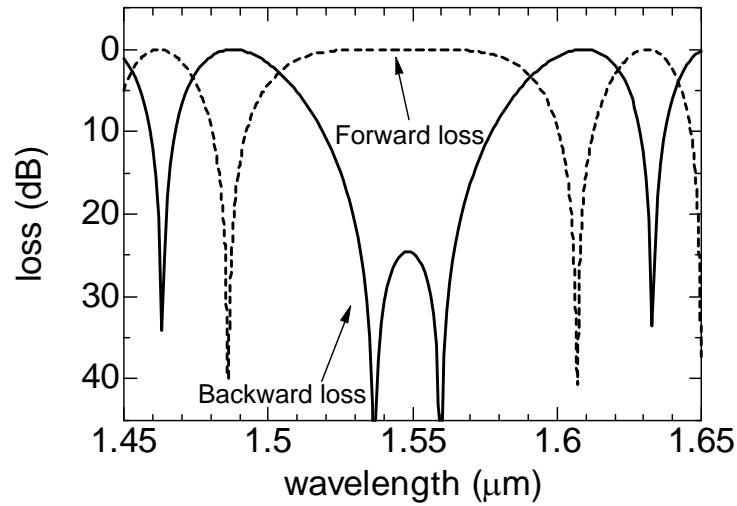


Fig. 5.12 Calculated spectral response of type-2 isolator, where the waveguide thickness is $0.26 \mu\text{m}$ and the width is $0.72 \mu\text{m}$.

5.5 Design of polarization converter

5.5.1 Principle of waveguide polarization converter

A polarization rotation in a planar waveguide is achieved by perturbing the asymmetry of waveguide structure so as to rotate the optical axis from the original position. The behavior is very similar to a light propagation in a birefringent material.

Generally, a lightwave propagating in a planar waveguide has two orthogonal eigenmodes, so-called slow and fast modes with specific longitudinal propagation constants β_0 and β_1 . We assume the x - and y -directions are the horizontal and vertical to the waveguide plane, respectively, and the light propagates along the z -direction. In full-vectorial consideration, the electromagnetic fields are expressed in terms of a superposition of two components as [9]

$$E_0 = A_0(\hat{x} \cos \phi - \hat{y} \sin \phi) \exp(-j\beta_0 z), \quad (5.3)$$

$$E_1 = A_1(\hat{x} \sin \phi + \hat{y} \cos \phi) \exp(-j\beta_1 z) \quad (5.4)$$

where A_0 and A_1 are the normalized amplitudes of the field and ϕ is the angle of optical axis. The polarization rotation can be explained in terms of the eigenmodes. We suppose that x -polarized wave is launched at the input $z = 0$ of a waveguide with the optical axis rotated $-\phi$. The wave is represented by a mixture of the two modes as shown in Fig. 5.13 (a). As they propagate independently with their respective propagation constants, interference occurs in each field component with respect to a half-beat length given by

$$L_\pi = \frac{\pi}{\beta_0 - \beta_1}. \quad (5.5)$$

Fig. 5.13 (b) shows the field states at $z = L_\pi$ where the phase difference between E_0 and E_1 is π . The total field is rotated by -2ϕ from the excited direction.

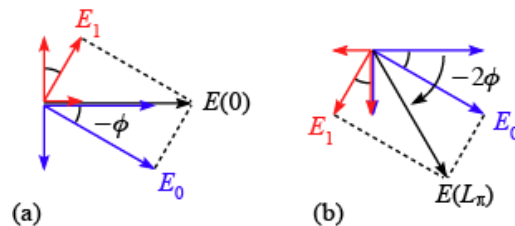


Fig. 5.13 Electric fields $E(z)$ as a superposition of two eigenmodes at (a) $z = 0$ and (b) $z = L_\pi$.

The angle of optical axis ϕ is estimated from the x - and y -amplitudes of the eigenmodes. However, the eigenmodes are calculated in 2-D field distributions for x - and y -components using a full-vectorial simulation. The optical axis cannot be solved directly. Here, a rotation parameter R is introduced [10]

$$R = \frac{\iint n^2(x, y) |E_x(x, y)|^2 dx dy}{\iint n^2(x, y) |E_y(x, y)|^2 dx dy} \quad (5.6)$$

where $n(x, y)$ is the refractive index distribution and $|E_x(x, y)|^2$, $|E_y(x, y)|^2$ are the electric field components of each eigenmode. The integrals are taken over the area of the computational window. When $R \gg 1$, the corresponding eigenstate is principally x -polarized; when $R = 1$, the optical axis is rotated by 45° with respect to x or y ; and when $R \ll 1$, the corresponding eigenstate is principally y -polarized. The rotation parameters for the two eigenmodes are denoted as R_0 and R_1 , respectively. Since the modes are orthogonal to each other, the angle of optical axis with respect to the x -axis is estimated by [15]

$$\phi = \cot^{-1} R_0 = \tan^{-1} R_1. \quad (5.7)$$

In symmetric planar waveguide systems extending primarily in the x -direction, the slow mode (E_0) has primarily x -component with a small y -component and the fast mode (E_1) has primarily y -component with a small x -component. Therefore, the angle of optical axis is $\sim 0^\circ$ and there is no polarization rotation for x - or y -polarized wave. On the other hand, in asymmetric waveguide systems, the optical axis is rotated from the x - or y -axis so that x - or y -polarized incident wave exhibits polarization rotation with respect to the half-beat length. In addition, if another asymmetric waveguide that has reversed optical axis are cascaded periodically with the half-beat length, the polarization rotation is accumulated as shown in Fig. 5.14. The polarization rotation is linearly accumulated by 2ϕ as each propagation length of L_π .

In this study, the proposed polarization-independent isolator requires 100% conversion between TE and TM modes, i.e., 90° polarization rotation. The cross-sectional images of the polarization converters are shown in Fig. 5.2 (c) and Fig. 5.3 (c). For type-1 isolator, asymmetric loaded waveguide is assumed. Since the rotation of optical axis is small in one section of mode converter, the reversed asymmetric structure is periodically cascaded to achieve the complete polarization conversion. For type-2 isolator, an angled-facet waveguide

structure is assumed. The optical axis can be designed to be rotated at 45° so that complete polarization conversion is achieved in one perturbed section which results in reduction of the insertion loss due to scattering at the junction of the reversed waveguides.

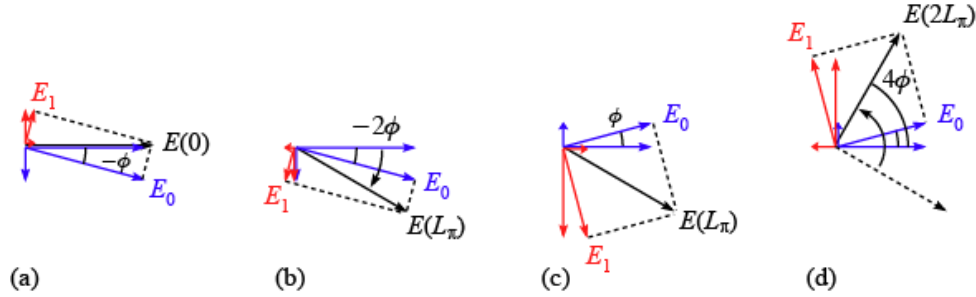


Fig. 5.14 Electric fields $E(z)$ as a superposition of two eigenmodes in cascaded asymmetric waveguides with reversed optical axes; at (a) $z=0$ and (b) $z=L_\pi$ in a waveguide with the optical axis $-\phi$; at (c) $z=L_\pi$ and (d) $z=2L_\pi$ in a waveguide with the optical axis ϕ .

5.5.2 Calculation results

First, polarization converters composed of the type-1 and type-2 structures are designed at a wavelength of $1.55 \mu\text{m}$ by using a full-vector FEM analysis [17]. It calculates the propagation constants of two eigenmodes as well as the electromagnetic fields in x - and y -components. In this section, the refractive indices of composed materials are set at the same as Section 5.4 and that of HfO_2 is set at 1.98 at a wavelength of $1.55 \mu\text{m}$.

For the type-1 isolator, the width and height of Ce:YIG channel waveguide are set at 3.0 and $0.6 \mu\text{m}$, respectively, which is compatible to the design of nonreciprocal phase shifter investigated in Section 5.4. The width of the loaded layer of HfO_2 is set at the half of the waveguide, i.e., $1.5 \mu\text{m}$. Fig. 5.15 shows the calculated half-beat length with a parameter of thickness of the loaded layer as a function of computational grid sizes of x and y . The accuracy of calculation increases at small grid sizes because the simulation results depend on the relative positions of the interface boundary with respect to the grid points near the interface, i.e., the simulation results in large grid sizes are not consistent. Ideally, an infinite small grid size as close to zero as possible should be used so that the simulated profile will be converged to the real profile. However, considering the limit of memory usage and the

computation time, only finite grid size can be used. One can estimate an ideal result by extrapolating the grid size to zero in Fig. 5.15. Also, a nonuniform grid which defines elaborate index profiles near the interface increases the accuracy of simulation result. Figure 5.16 shows the calculated half-beat length as a function of thickness of the loaded layer with a nonuniform computation grid. The calculated half-beat lengths are 27.2 μm , 32.1 μm , and 36.5 μm , and the calculated angles of optical axis are 0.127° , 0.150° , and 0.170° , for the thickness of loaded layer of 0.1 μm , 0.2 μm , and 0.3 μm , respectively. The angles of optical axis seem to be too small for the asymmetries of assumed structure. We find that the estimation of the angle of optical axis using (5.7) from (5.6) is invalid for an asymmetric structure with weak perturbation because the angles obtained from each rotation parameter is not coincident each other, i.e., $\cot^{-1}(R_0) \neq \tan^{-1}(R_1)$. A complete polarization conversion is theoretically achieved by cascading a number of the reversed asymmetric structures so that the total polarization rotation becomes 90° . In this case, the propagation length required for the complete conversion is estimated to be about 9.5 mm which is too long compared with the calculation result by using a full-vector BPM investigated later.

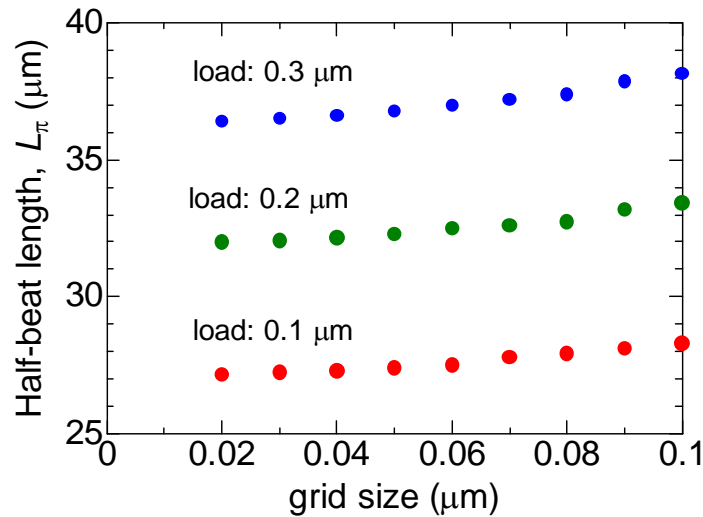


Fig. 5.15 Half-beat length as a function of computational grid sizes in type-1 structure of $w=$ 3.0 μm and $h=$ 0.6 μm .

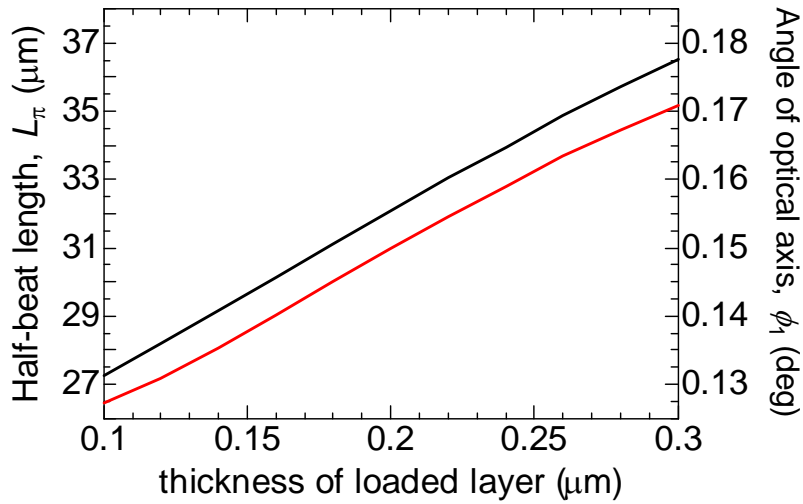


Fig. 5.16 Half-beat length as a function of thickness of the loaded layer calculated with a nonuniform grid. The grid sizes of $\Delta x = 0.1 \mu\text{m}$, $\Delta y = 0.05 \mu\text{m}$ in bulk region and $\Delta x = 0.01 \mu\text{m}$, $\Delta y = 0.005 \mu\text{m}$ near the boundary are connected with moderately varied grids.

For type-2 isolator, the waveguide has an angled facet in one sidewall. The angle is simply set at the 54.736° coincided with a (111) plane of Si crystal in a (100)-oriented SOI wafer. The sidewall is completely etched to SiO_2 under-cladding layer. Width at the bottom of angled facet is defined as the section width of the polarization converter. The height of Si waveguide is set at 0.30 or $0.40 \mu\text{m}$. The rotation parameter is then designed to be $R = 1$ by varying the section width. Figures 5.17 and 5.18 show the calculated propagation constants normalized by the wavenumber k , i.e., the effective refractive indices of two eigenmodes, and the rotation parameters. The calculation accuracy increase for small grid sizes. Since a nonuniform grid is not useful for the angled facet waveguide, uniform grid of $\Delta x = \Delta y = 0.01 \mu\text{m}$ is used in this case. The designed section widths are 0.38 and $0.51 \mu\text{m}$, and the half-beat lengths are 1.87 and $3.35 \mu\text{m}$, for the waveguide height of 0.30 and $0.40 \mu\text{m}$, respectively. Figure 5.19 shows the calculated x - and y -components of electric field distribution in two eigenmodes for the case that the section width and height are 0.51 and $0.40 \mu\text{m}$, respectively. E_x and E_y correspond to the first and second terms in (5.3) and (5.4). The field distributions have different discontinuities at the interface that means the orthogonality of two modes.

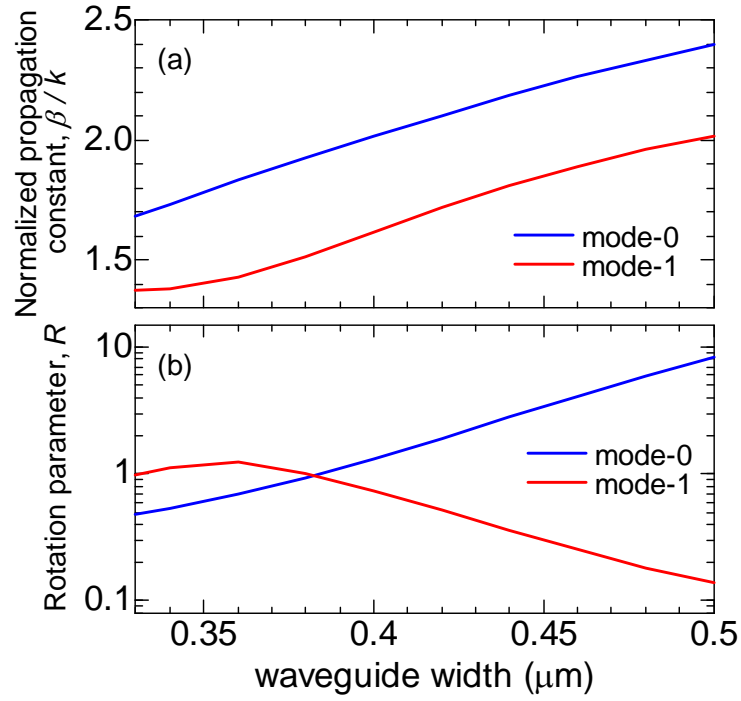


Fig.5.17 (a) Normalized propagation constants and (b) rotation parameters of two eigenmodes as a function of section width for type-2 structure at $h = 0.30 \mu\text{m}$.

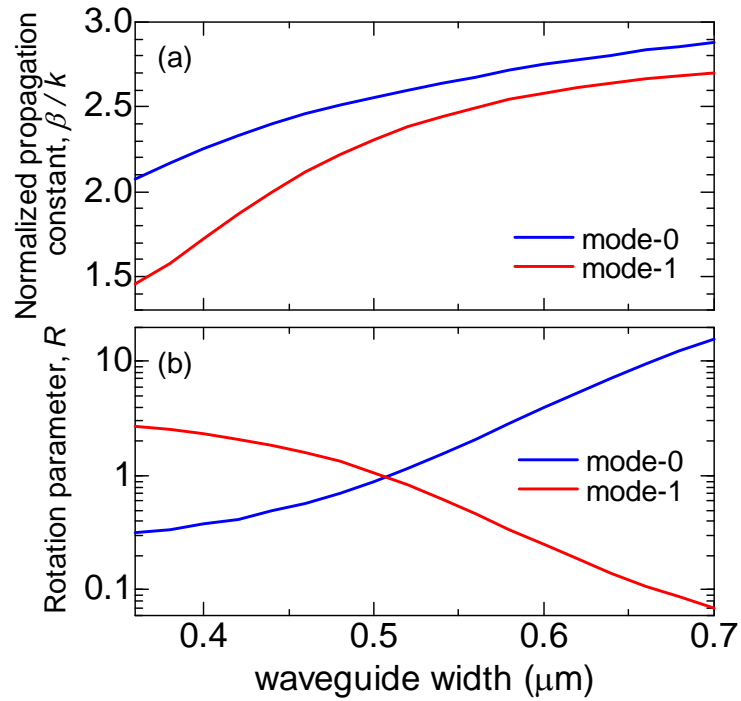


Fig.5.18 (a) Normalized propagation constants and (b) rotation parameters of two eigenmodes as a function of section width for type-2 structure at $h = 0.40 \mu\text{m}$.

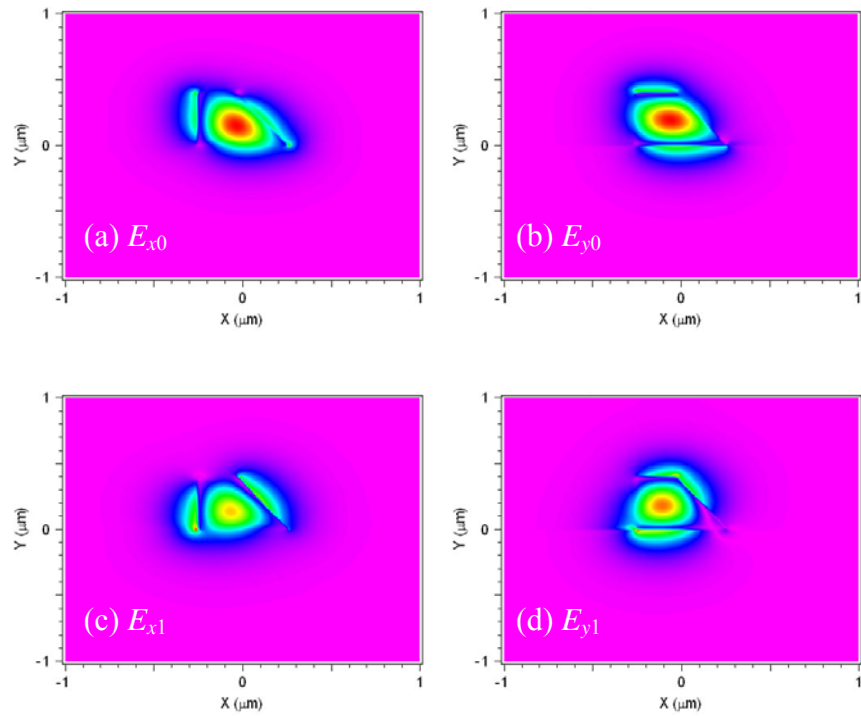


Fig. 5.19 x - and y -components of electric field distribution in two eigenmodes for type-2 structure at $w=0.51\text{ }\mu\text{m}$ and $h=0.40\text{ }\mu\text{m}$.

Next, the polarization rotation is analyzed by using a full-vector 3-D finite difference (FD) BPM [17,18]. For type-1 structure, the scattering loss at the junction of reversed waveguide sections is inevitable. A light propagation in periodically loaded asymmetric waveguides is calculated as shown in Fig. 5.20. The dimension of waveguide structure is the same as investigated above. The monitored power of excited and converted lights is associated with the x - and y -components of electric field. Therefore, the results can be considered as the polarization conversions from TE (-like) to TM (-like) modes as long as the fields distribute like fundamental modes. The converted power is maximized when the section lengths are set at 27.2, 31.7, and 35.0 μm for 0.1-, 0.2-, and 0.3- μm -thick loaded layers, respectively. The results are similar to the half-beat lengths designed by FEM. However, the power is not fully converted to the other mode while that of excited mode almost disappears at some propagation length. This is due to the scattering loss at the junction of reversed asymmetric waveguide sections. Although a large perturbation by a thick loaded layer enables the polarization conversion in shorter propagation length and less number of section, the

converted power decreases due to the large scattering loss at each junction. In addition, for a thick loaded layer, there is large difference in the propagation length between minimizing the excited power and maximizing the converted power. Consequently, a preferable design of the polarization converter of type-1 structure is 39 number of periodically asymmetric waveguide composed of a 0.1- μm -thick loaded layer and a 27.2- μm -long half-beat length, where the polarization conversion of $\sim 70\%$ is obtained at the propagation length of 1060.8 μm .

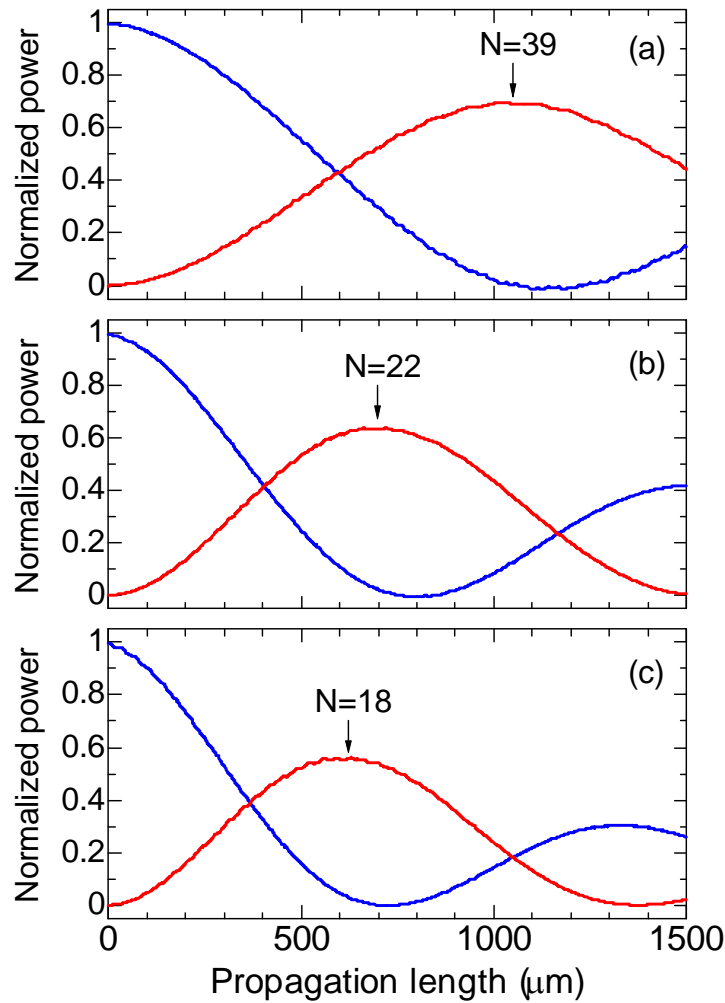


Fig. 5.20 A light propagation in periodically loaded asymmetric waveguides calculated by 3-D full-vector BPM with the grid sizes of $\Delta x = 0.1$ and $\Delta y = 0.03$ μm . The converted powers (red lines) are maximized at the half-beat lengths of (a) 27.2 μm for 0.1- μm -thick loaded layer, (b) 31.7 μm , for 0.2- μm -thick loaded layer and (c) 35.0 μm for 0.3- μm -thick loaded layer, respectively. N denotes the number of cascaded asymmetric waveguide sections.

For type-2 structure, our full-vector 3-D BPM tends to be unstable due to the highly hybrid nature of the vectorial modes given by high-index contrast interface and the angled facets. At the interface between Si and air, the abrupt index change may cause the FD BPM to be unstable in some cases. This instability is associated with an algorithm called the alternating direction implicit (ADI) method used for solving 3-D systems. To improve the stability, a procedure described in Ref. [11] is adopted that the grid points near the interface are artificially averaged by the indices of the nearby surrounding grid points such that a smoothly changed, linearly averaged, index profile at the interface replaces the real step-index boundary with a large index contrast. Fig. 5.21 shows the refractive index profile represented by step-index boundary with the grid size of $0.002 \mu\text{m}$, and the modified index profile represented by the smoothed boundary averaged by those of the surrounding grids within 20 points along x and y directions including itself, (i.e., 41×41 points) and converted to the grid size of $0.01 \mu\text{m}$.

Even though the smoothing procedure makes the simulation stable, the simulated index profile deviates from the original physical structure. Fig. 5.22 shows the calculated half-beat length as a function of number of surrounding points N , where $(2N+1) \times (2N+1)$ points are used for smoothing procedure. Here, the scheme parameter [18] is set at 0.55 to make the simulation stable while it slightly attenuates the power along the propagation length. The result shows different tendencies for the number of smoothing between $N < 10$ and $N > 10$. Since no simulation result is obtained at $N < 5$ due to the instability, the results of $N > 10$ are more reliable than those of $N < 10$. Therefore the ideal half-beat length can be estimated to be $L_\pi = 2.2 \mu\text{m}$ by extending the asymptotic curve to $N = 0$ and ignoring the results of $N < 10$ in Fig. 5.22. This is different from the result $L_\pi = 1.87 \mu\text{m}$ calculated by full-vector FEM. In this BPM simulation, the x -component of one eigenmode is excited at the asymmetric waveguide. However, the x -component of the other eigenmode should be excited at the same time to assume the x -polarized launched light. Actually, it takes a propagation length of several microns to obtain stable propagation in the simulation. Even when the smoothing procedure is adopted, the 3-D BPM may not be suitable for such a problem with abrupt change in polarization state along the propagation direction, while it can solve a problem of weak

perturbation such as type-1 structure.

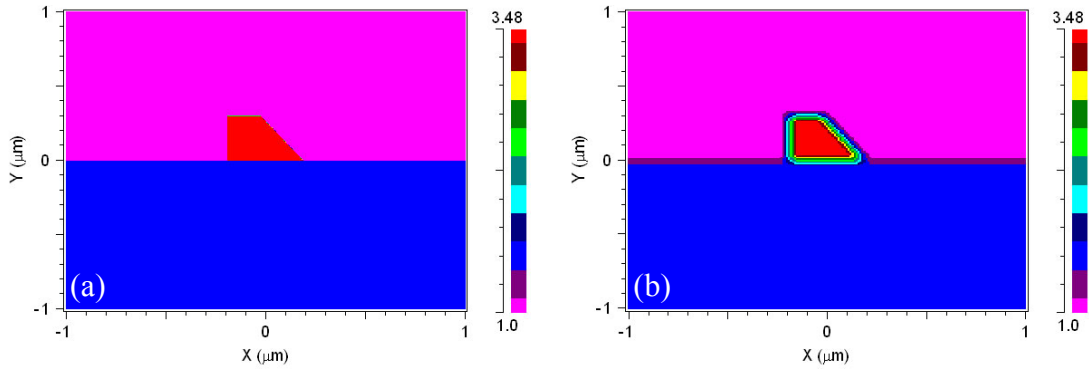


Fig. 5.21 Color scales of (a) refractive index profile represented by step-index boundary with the grid size of $0.002 \mu\text{m}$, and (b) the modified index profile represented by smoothed boundary averaged by those of the surrounding grids within 20 points.

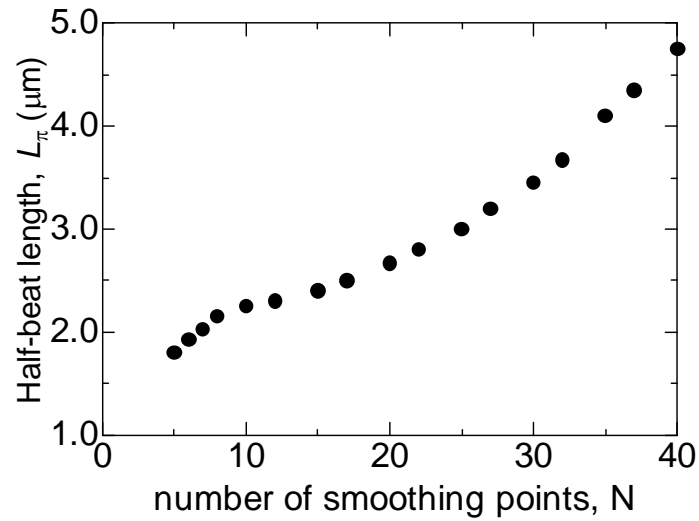


Fig. 5.22 Half-beat length calculated with a smoothed index profile as a function of number of smoothing grid points N .

5.6 Discussion

In order to realize the polarization-independent isolator, one has to demonstrate and confirm the operation of each component; nonreciprocal phase shifter, polarization converter, and 3-dB coupler.

In our design, the dimension of the waveguide in the nonreciprocal phase shifter must be strictly controlled to satisfy the condition. The different operation between TE and TM modes can be confirmed by using a measurement setup as shown in Fig. 5.23 [19]. TE and TM modes are simultaneously and equally excited from a $\sim 45^\circ$ -rotated fiber to a magneto-optic waveguide. An external magnetic field is transversely applied to the propagation direction and is parallel to the film plane to obtain a nonreciprocal phase shift only for the TM mode. Both modes propagate in the magneto-optic waveguide and have a different phase at the end of the waveguide due to the different propagation constants. After launched to the free space, the modes have an identical propagation constant in air and construct a circularly, ellipsoidally, or lineally polarized state depending on the phase difference between TE and TM modes in the waveguide. Using a free-space polarizer, the polarization state is analyzed by the power intensity at the photo detector. Then the direction of external magnetic field is reversed, the polarization state changes due to the nonreciprocal phase shift only for the TM mode. By measuring the magnet-optic waveguides formed with different width or propagation length, the difference in phase shift between TE and TM modes, including the nonreciprocal phase shift for TM mode, can be analyzed as a function of the waveguide parameter.

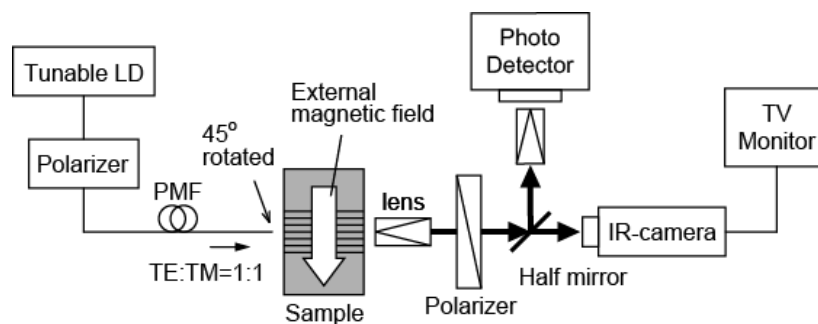


Fig. 5.23 Setup for a measurement in nonreciprocal operation between TE and TM modes.

The polarization converter for type-1 structure is realized by depositing and selectively etching a loaded layer on the waveguide. The angled facet asymmetric waveguide for type-2 structure is fabricated by a combination of dry and wet etching processes. An asymmetric waveguide with very narrow slot can be formed in one dry etching process utilizing a phenomenon called “RIE lag” where the etching depth is controlled by the slot width [12]. Also, several deep slots etched at 45° into a waveguide structure largely rotate the optical axis and provide high birefringence that enables complete polarization conversion with the propagation length of several microns [13].

The 3-dB coupler must operate for both TE and TM modes as well. A Y-branch coupler is less sensitive to the polarization but it needs longer propagation length for low-loss coupling. A directional coupler becomes sensitive if there is a large difference in the field distribution between the two modes. A multi-mode interference (MMI) coupler becomes sensitive to the polarization if there is a large birefringence in the multimode section.

5.7 Summary

A polarization-independent magneto-optical waveguide isolator using TM mode nonreciprocal phase shift is proposed. The operation is not realized by a polarization diversity scheme, but rather by the phase difference between the reciprocal TE mode and nonreciprocal TM mode. Since the nonreciprocal phase shift is used only for the TM mode, it can be easily realized with integrated structures. The author shows the proposed principle of operation and the design rules that are needed for wide operational bandwidth and single-mode operation. Two different isolator designs that assume two specific material systems are demonstrated.

Polarization converters for the use of the isolator are investigated. Some asymmetric waveguide systems are compatible to the isolator configuration and they realize a passive and reciprocal polarization conversion. Two polarization converters with specific structures are designed by full-vectorial simulations of FEM and 3-D BPM.

References

- [1] Products catalog of TDK Corporation (<http://www.tdk.co.jp/>)
- [2] O. Zhuromskyy, M. Lohmeyer, N. Bahlmann, H. Dötsch, P. Hertel, and A. F. Popkov, "Analysis of polarization independent Mach-Zehnder-type integrated optical isolator," *J. Lightwave Technol.*, vol.17, pp.1200-1205 (1999).
- [3] J. Fujita, M. Levy, R. M. Osgood, Jr., L. Wilkens, and H. Dötsch, "Polarization-independent waveguide optical isolator based on nonreciprocal phase shift," *IEEE Photon. Technol. Lett.*, vol.12, pp.1510-1512 (2000).
- [4] N. Sugimoto, T. Shintaku, A. Tate, H. Terui, M. Shimokozono, E. Kubota, M. Ishii, and Y. Inoue, "Waveguide polarization-independent optical circulator," *IEEE Photon. Technol. Lett.*, vol.11, pp.355-357 (1999).
- [5] T. R. Zaman, X. Guo, and R. J. Ram, "Proposal for a polarization-independent integrated optical circulator," *IEEE Photon. Technol. Lett.*, vol.18, pp.1359-1368 (2006).
- [6] H. Yokoi and T. Mizumoto, "Proposed configuration of integrated optical isolator employing wafer-direct bonding technique," *Electron. Lett.*, vol.33, pp.1787-1788 (1997).
- [7] H. Yokoi, T. Mizumoto, and Y. Shoji, "Optical nonreciprocal devices with a silicon guiding layer fabricated by wafer bonding," *Appl. Opt.*, vol.42, pp.6605-6612 (2003).
- [8] R. L. Espinola, T. Izuhara, M.-C. Tsai, and R. M. Osgood, Jr., "Magneto-optical nonreciprocal phase shift in garnet/silicon-on-insulator waveguides," *Opt. Lett.*, vol.29, pp.941-943 (2004).
- [9] W. Huang and Z. M. Mao, "Polarization rotation in periodic loaded rib waveguides," *J. Lightwave Technol.*, vol.10, pp.1825-1831 (1992).
- [10] V. P. Tzolov and M. Fontaine, "A passive polarization converter free of longitudinally-periodic structure," *Opt. Commun.*, vol.127, pp.7-13 (1996).
- [11] J. Z. Huang, R. Scarmozzino, G. Nagy, M. J. Steel and R. M. Osgood, Jr., "Realization of a compact and single-mode optical passive polarization converter," *IEEE Photon. Technol Lett.*, vol.12, pp.317-319 (2000).
- [12] B. M. Holmes and D. C. Hutchings, "Realization of novel low-loss monolithically integrated passive waveguide mode converters," *IEEE Photon. Technol. Lett.*, vol.18, pp.43-45 (2006).
- [13] M. V. Kotlyar, L. Bolla, M. Midrio, L. O'Faolain, and T. F. Krauss, "Compact polarization

- converter in InP-based material,” *Opt. Express*, vol.13, pp.5040-5045 (2005).
- [14] A. M. Radojevic, R. M. Osgood, Jr., M. Levy, A. Kumar, and H. Bakhru, “Zeroth-order half-wave plates of LiNbO₃ for integrated optic application at 1.55 μm ,” *IEEE Photon. Technol. Lett.*, vol.12, pp.1653-1655 (2000).
- [15] H. Deng, D. O. Yevick, C. Brooks, and P. E. Jessop, “Design rules for slanted-angle polarization rotators,” *J. Lightwave Technol.*, vol.23, pp.432-445 (2005).
- [16] M. Gomi, H. Furuyama, and M. Abe, “Strong magneto-optical enhancement in highly Ce-substituted iron garnet films prepared by sputtering,” *J. Appl. Phys.*, vol.70, pp.7065-7067 (1991).
- [17] BeamPROP/FemSIM software from RSoft Design Group, (<http://www.rsoftdesign.com/>)
- [18] W. P. Huang and C. L. Xu, “Simulation of three-dimensional optical waveguides by a full-vector beam propagation method,” *IEEE J. Quantum. Electron.*, vol.29, pp.2639-2648 (1993).
- [19] Y. Okamura, H. Inuzuka, T. Kikuchi, and S. Yamamoto, “Nonreciprocal propagation in magnetooptic YIG rib waveguides,” *J. Lightwave Technol.*, vol.LT-4, pp.711-714 (1986).

Chapter 6:

Conclusions

Magneto-optical isolators are indispensable in high-speed optical fiber communication systems and are used to protect optical active devices from unwanted reflected lights. However, the absence of practical waveguide isolator is a bottleneck for reducing the cost of light source modules and realizing integrated optical circuits. Several types of waveguide isolator are investigated and developed by some researchers. The author studies the waveguide magneto-optical isolator employing nonreciprocal phase shift. Integration, miniaturization, wideband operation, and polarization-independent operation must be accomplished for waveguide isolators to become a reality and replace bulk isolators. The results obtained throughout this study are summarized as follows:

In Chapter 2, the nonreciprocal phase shift is theoretically and numerically analyzed. Using 1-D and 2-D waveguide models, the nonreciprocal phase shift is calculated by directly solving the eigenvalue equation and by perturbation theory using beam propagation method (BPM) as well as finite element method (FEM). For narrower waveguide, 2-D model should be used for taking the effect of the lateral optical confinement into account. In the comparison among the several mode solving methods, reliable calculation results are obtained by using full-vector simulations than semi-vector ones. Then magneto-optical isolators based on a Mach-Zehnder interferometer (MZI) employing nonreciprocal phase shift are designed for specific material systems.

In Chapter 3, a magneto-optical isolator with Si waveguide is demonstrated. First, Si waveguide is fabricated on a silicon-on-insulator (SOI) wafer and characterized. Second, a surface activated direct bonding with oxygen plasma treatment is investigated. A direct bonding between Si and $\text{CeY}_2\text{Fe}_5\text{O}_{12}$ (Ce:YIG) is successfully achieved with oxygen plasma of 100-W radio frequency power for 30-s followed by annealing at 200 – 250 °C with a

pressure of ~ 5 MPa. Then, a magneto-optical isolator composed of a $0.3\text{-}\mu\text{m}$ -thick Si rib waveguide with low-loss propagation characteristics is characterized in terms of the nonreciprocal operation by reversing the propagation direction. The maximum isolation of 21 dB is obtained at a wavelength of 1559 nm. The insertion loss of 8 dB and the temperature dependence of the isolator are also examined.

In Chapter 4, a wideband design of a magneto-optical isolator employing nonreciprocal phase shift is proposed and its performance is demonstrated. The wideband operation is realized by phase adjustment in the MZI to compensate the wavelength dependence of nonreciprocal phase shift for that of reciprocal one. First, the author demonstrated a dramatic improvement of the backward loss with acceptably little deterioration of the forward loss by numerical calculations. This design concept is applicable to the isolator with any other material, structure, and dimension. Next, the author fabricated a wideband isolator with Ce:YIG waveguide to demonstrate the wideband operation experimentally. Compared with the conventional design, higher isolation ratio up to 25 dB is successfully obtained at around $\lambda = 1.60\text{ }\mu\text{m}$.

In Chapter 5, a polarization-independent magneto-optical waveguide isolator using TM mode nonreciprocal phase shift is proposed. The operation is not realized by polarization diversity, but rather by the phase difference between the reciprocal TE mode and nonreciprocal TM mode. Since the nonreciprocal phase shift is used only for the TM mode, it can be easily realized with integrated device structures. The author shows the proposed principle of operation and the design rules that are needed for wide operational bandwidth and single-mode operation. Two isolator designs that assume different material systems are demonstrated. In addition, polarization converters for the use of the isolator are investigated. Some asymmetric waveguide structures compatible to the isolator configuration are investigated to realize a passive and reciprocal polarization conversion. Two polarization converters with different structures are designed by full-vectorial simulations of FEM and 3-D BPM.

The author believes that the achievement shown in this thesis contributes largely to push the waveguide isolator into a reality. Further studies to be done are as follows:

1) Magneto-optical isolator with Si waveguide

In order to integrate the magneto-optical isolator with Si photonic circuit, it is important to miniaturize the isolator with low-loss Si-wire waveguides. Next, the condition of direct bonding should be optimized with respect to a thermal durability testing in the temperature range of practical applications. Also, the bonding interface must be investigated about the interlayer and the influence on the nonreciprocal phase shift.

2) Wideband operation of a magneto-optical isolator

The principle of the wideband operation is applicable to the magneto-optical isolator based on Mach-Zehnder interferometer with any structures such as GaInAsP/InP and Si/SiO₂ based waveguides. Even though an ultra-wideband operation is not achieved in a fabricated isolator with Ce:YIG waveguide due to a large absorption at shorter wavelength region, it is to be demonstrated by using semiconductor waveguides.

3) Polarization-independent magneto-optical isolator

In order to realize the polarization-independent isolator, one has to demonstrate and confirm the operation of each component; nonreciprocal phase shifter, polarization converter, and 3-dB coupler. After that, a polarization-independent isolator compatibly designed with these components will be demonstrated.

Acknowledgements

The author would like to express the most gratitude to Professor Tetsuya Mizumoto of Tokyo Institute of Technology for his teaching, encouragement, and fruitful discussions throughout his whole study.

The author would like to appreciate Professor Kohroh Kobayashi, Professor Fumio Koyama, Professor Shigehisa Arai, Associate Professor Nobuhiko Nishiyama of Tokyo Institute of Technology, and Dr. Koji Ando of National Institute of Advanced Industrial Science and Technology for their useful discussions and advices on this study.

A part of this study is supported by Research Fellowship of the Japan Society for the Promotion of Science for Young Scientists.

The author would like to express sincere gratitude to Associate Professor Hideki Yokoi of Shibaura Institute of Technology for his helpful guidance, discussion, and advice.

The author would like to appreciate Professor Richard M. Osgood, Jr., Mr. I-Wei Hsieh, and Mr. Mitsuhide Takekoshi of Columbia University for their fruitful discussions and continuous supports since he has visited the university.

The author would like to acknowledge Associate Professor Katsumi Nakatsuhara (Kanagawa Institute of Technology), Dr. Seok-Hwan Jeong (Fujitsu), Dr. Jeong-Su Yang (Yonsei University), and Dr. Takeo Maruyama (Tokyo Institute of Technology) for their helpful comments and discussions on meetings and conferences.

The author would like to thank senior and present members in the doctoral course; Dr. Naoto Kitahara (Tokyo Polytechnic University), Dr. Itsuro Morita (KDDI), Dr. Shingo Kawai (NTT), Dr. Koichi Maru (Hitachi Cable), Mr. Akira Naka (NTT), Mr. Shin-ichi Wakabayashi (Panasonic), Mr. Kazumasa Sakurai, Dr. Jae-kuk Seo (BOSCH), Mr. Minoru Taya, Mr. Shinichi Sakamoto, Mr. San-Hun Kim, and Mr. Ryohei Takei for their advices and inspiring discussions.

The author wishes to thank all the members of Mizumoto Laboratory; Mr. Takashi Sakai, Mr. Satoshi Narikawa, Mr. Jalil Mohammad Abdul, Mr. Ryotaro Takaki, Mr. Hiroaki Iwasaki, Mr. Masahiro Kobayashi, Mr. Takayuki Ishii, Mr. Masaki Ono, Mr. Tomohiro Morita, Mr. Atsushi Saito, Mr. Hideki Saito, Ms. Etsu Shin, Mr. Nguyen Anh Hong, Mr. Kazuhiko Tamura, Mr. Yoichi Akano, Mr. Nobumasa Tanaka, Ms. Nguyen Thi Ngoc Nhi, Mr. Yoshihiro Yazaki, Mr. Masashi Hashimoto, Mr. Ryohei Kouga, Mr. Kenji Abe, Mr. Masaki Yoshimura, Mr. Koji Kubota, Ms. Yukie Inoue, Mr. Tetsuya Hagiwara, Mr. Tomohiro Takanashi and Mr. Etsuji Hayakawa for their valuable cooperation in experiment and pleasant days in the laboratory.

Finally, the author deeply thanks his family and his lover, Manami for their understandings, supports, and encouragements.

Publication list

Journal Papers

- [1] Y. Shoji, H. Yokoi, and T. Mizumoto, "Enhancement of magneto optic effect in optical isolator with GaInAsP guiding layer by selective oxidation of AlInAs," Jpn. J. Appl. Phys., vol.43, pp.590-593 (2004).
- [2] Y. Shoji and T. Mizumoto, "Wideband design of nonreciprocal phase shift magneto-optical isolators using phase adjustment in Mach-Zehnder interferometers," Appl. Opt., vol.45, pp.7144-7150 (2006).
- [3] Y. Shoji and T. Mizumoto, "Ultra-wideband design of waveguide magneto-optical isolator operating in 1.31 μ m and 1.55 μ m band," Opt. Express, vol.15, pp.639-645 (2007).
- [4] Y. Shoji and T. Mizumoto, "Wideband operation of Mach-Zehnder interferometric magneto-optical isolator using phase adjustment," Opt. Express, vol.15, pp.13446-13450 (2007).
- [5] Y. Shoji, I-W. Hsieh, R. M. Osgood, Jr., and T. Mizumoto, "Polarization-independent magneto-optical isolator using TM-mode nonreciprocal phase shift," J. Lightwave Technol., vol.25, pp.3108-3113 (2007).
- [6] Y. Shoji, H. Yokoi, I-W. Hsieh, R. M. Osgood, Jr., and T. Mizumoto, "Magneto-optical isolator with silicon waveguides fabricated by direct bonding," Appl. Phys. Lett., vol.92, p.071117 (2008).
- [7] H. Yokoi, T. Mizumoto, and Y. Shoji, "Optical nonreciprocal devices with a silicon guiding layer fabricated by wafer bonding," Appl. Opt., vol.42, pp.6605-6612 (2003).
- [8] H. Yokoi, Y. Shoji, and T. Mizumoto "Calculation of nonreciprocal phase shift in magneto-optic waveguide with silicon guiding," Jpn. J. Appl. Phys., vol.43, pp.5871-5874 (2004).
- [9] H. Yokoi, Y. Shoji, E. Shin, and T. Mizumoto, "Interferometric optical isolator employing a nonreciprocal phase shift operated in a unidirectional magnetic field," Appl. Opt., vol.43, pp.4745-4752 (2004).
- [10] J-S. Yang, Y. Shoji, H. Yokoi, M. Ono, and T. Mizumoto, "Investigation of nonreciprocal characteristics and design of interferometric optical isolator with multimode interference coupler operating with a unidirectional magnetic field," Jpn. J. Appl. Phys., vol.43, pp.7045-7049 (2004).

- [11] H. Yokoi, Y. Shoji, T. Suzuki, N. Nishimura, and T. Mizumoto, "Coupling characteristics of three-guide tapered coupler for optical isolator with Si guiding layer," *Jpn. J. Appl. Phys.*, vol.45, pp.6323-6325 (2006).
- [12] Y. Yazaki, Y. Shoji, and T. Mizumoto, "Demonstration of interferometric waveguide isolator with a unidirectional magnetic field," *Jpn. J. Appl. Phys.*, vol.46, pp.5460-5464 (2007).

International Conferences

- [13] Y. Shoji, H. Yokoi, and T. Mizumoto, "Enhancement of magneto-optic effect in magneto-optic waveguide with low refractive index undercladding layer," 2003 International Conference on Solid State Devices and Materials (SSDM 2003), A-5-5, Tokyo, Japan, September 16-18 (2003).
- [14] Y. Shoji, H. Yokoi, and T. Mizumoto, "Ultracompact optical isolator with a silicon high index contrast waveguide," Conference on Lasers and Electro Optics / International Quantum Electronics Conference (CLEO/IQEC 2004), CThT7, San Francisco, California, May 16-21 (2004).
- [15] Y. Shoji, H. Yokoi, and T. Mizumoto, "Fabrication of ultracompact optical isolator with Si-phonic wire waveguides," International Quantum Electronics Conference 2005 and The Pacific Rim Conference on Lasers and Electro Optics 2005 (IQEC/CLEO-PR 2005), CTuK1-2, Tokyo, Japan, July 11-15 (2005).
- [16] Y. Shoji, H. Yokoi, and T. Mizumoto, "Mach-Zehnder interferometer with Si wire waveguides for ultracompact optical isolator," The 11th Microoptics Conference (MOC'05), D1, Tokyo, Japan, October 30- November 2 (2005).
- [17] Y. Shoji and T. Mizumoto, "Novel design of nonreciprocal phase shift optical isolators for wideband operation," The 11th OptoElectronics and Communication Conference (OECC 2006), 5B4-5, Kaohsiung, Taiwan, July 3-7 (2006).
- [18] Y. Shoji and T. Mizumoto, "Novel polarization-independent waveguide optical isolator employing nonreciprocal phase shift," The 12th Microoptics Conference (MOC'06), D-5, Seoul, Korea, September 10-14 (2006).
- [19] Y. Shoji and T. Mizumoto, "Wideband operation of magneto-optical isolator with phase adjusted

- Mach-Zehnder interferometer,” The 19th Annual Meeting of the IEEE Laser & Electro-Optics Society (LEOS 2006), ThV2, Montreal, Canada, October 29- November 2 (2006).
- [20] Y. Shoji and T. Mizumoto, “Ultra-wideband design of a magneto-optical isolator operating in 1.31 μ m and 1.55 μ m,” The 20th Annual Meeting of the IEEE Laser & Electro-Optics Society (LEOS 2007), TuC4, Lake Buena Vista, Florida, October 21-25 (2007).
- [21] Y. Shoji, H. Yokoi, I-W. Hsieh, R. M. Osgood, Jr., and T. Mizumoto, “Magneto-optical isolator with SOI waveguide,” The Optical Fiber Conference and Exposition and The National Fiber Optic Engineers Conference (OFC/NFOEC 2008), OTuC8, San Diego, California, February 24-28 (2008).
- [22] H. Yokoi, Y. Shoji, and T. Mizumoto, “Selective oxidation and successive wet etching for freestanding structure of magneto-optical waveguide,” IEEE/LEOS International Conference on Optical MEMS, TuP12, pp.75-76, Waikoloa, Hawaii, August (2003).
- [23] T. Sakai, Y. Shoji, H. Yokoi, and T. Mizumoto, “Enhancement of magneto-optic effect in optical isolator with semiconductor guiding layer by selective oxidation of AlInAs,” The 8th Optoelectronics and Communication Conference (OECC 2003), Shanghai, China, 15E4-3, vol.1, pp.179-180, October 13-16 (2003).
- [24] H. Yokoi, Y. Shoji, and T. Mizumoto, “Optical isolator with Si guiding layer fabricated by wafer bonding,” The 9th Microoptics Conference (MOC’03), H37, Tokyo, Japan, October 29-31 (2003).
- [25] H. Yokoi, Y. Shoji, E. Shin, and T. Mizumoto, “Interferometric optical isolator with distinct layer structures employing nonreciprocal phase shift,” 7th International Symposium on Contemporary Photonics Technology (CPT2004), P-11, pp.87-88, Tokyo, Japan, January 14-16 (2004).
- [26] H. Yokoi, Y. Shoji, E. Shin, and T. Mizumoto, “Demonstration of optical isolator employing nonreciprocal phase shift operated under unidirectional magnetic field,” 9th OptoElectronics and Communications Conference / 3rd International Conference on Optical Internet (OECC/COIN 2004), 13P-126, Kanagawa, Japan, July 12-16 (2004).
- [27] H. Yokoi, Y. Shoji, and T. Mizumoto, “Feasibility of optical isolator with Si guiding layer employing nonreciprocal phase shift,” The 10th Microoptics Conference (MOC’04), L-17, p.94, Jena, Germany, September (2004).
- [28] M. Taya, Y. Shoji, and T. Mizumoto, “TE-cut polarizer based on silicon wire waveguide,” The

- 11th Microoptics Conference (MOC'05), H10, pp.136-137, Tokyo, Japan, October 30-November 2 (2005).
- [29] T. Mizumoto, K. Sakurai, Y. Shoji, and H. Saito, “(Invited) Waveguide optical isolator integratable to photonic devices,” Integrated Photonics Research and Applications Topical meeting (IPRA 2006), ITuG1, Uncasville, Connecticut, April 24-26 (2006).
- [30] T. Mizumoto, H. Saito, and Y. Shoji, “Semi-leaky optical isolator fabricated by surface activation wafer bonding,” The 11th Optoelectronics and Communications Conference (OECC 2006), 5B4-1, Kaohsiung, Taiwan, July 3-7 (2006).
- [31] T. Mizumoto, K. Sakurai, Y. Shoji, and H. Saito, “(Invited) Integration of optical isolators and semiconductor lasers by wafer bonding,” Asia Pacific Optical Communications (APOC 2006), 6352-90, Gwangju, Korea, September 7 (2006).
- [32] Y. Yazaki, Y. Shoji, and T. Mizumoto, “Demonstration of interferometric waveguide optical isolator with a unidirectional magnetic field,” The 12th Microoptics Conference (MOC'06), C-5, pp.66-67, Seoul, Korea, September 10-14 (2006).
- [33] T. Mizumoto and Y. Shoji, “(Invited) Integrated waveguide optical isolators: principle and history,” 2008 Conference on Lasers and Electro-Optics (CLEO 2008), San Jose, California, May 4-9 (2008). (to be presented.)

Technical Reports

- [34] Y. Shoji, H. Yokoi, and T. Mizumoto, “Enhancement of magneto-optic effect in optical isolator with semiconductor guiding layer by selective oxidation of AlInAs (非相反移相効果増大のためのAlInAs選択酸化による低屈折率クラッド層の形成),” Technical Report of IEICE, EMD2003-41, Aug. (2003). (in Japanese.)
- [35] Y. Shoji and T. Mizumoto, “Broad-band operation of asymmetric Mach-Zehnder interferometer optical isolator using nonreciprocal phase shift (非対称マッハツェンダー干渉計を用いた非相反移相型光アイソレータの広帯域化)” Technical Report of IEICE, PN2005-66, Jan. (2006). (in Japanese.)
- [36] Y. Shoji and T. Mizumoto, “Proposal of polarization-independent optical isolator using TM

nonreciprocal phase shift and waveguide mode converter (TMモード非相反移相効果と導波路型モード変換器を用いた偏波無依存型光アイソレータの提案)” Technical Report of IEICE, OPE2006-12, May (2006). (in Japanese.)

- [37] H. Yokoi, Y. Shoji, and T. Mizumoto, “Optical nonreciprocal devices with Si guiding layer (Si導波層を有する光非相反素子),” Technical Report of IEICE, OPE2003-273, Feb. (2004). (in Japanese.)
- [38] H. Yokoi, Y. Shoji, E. Shin, and T. Mizumoto, “Demonstration of interferometric optical isolator operated in unidirectional external magnetic field (一方向外部磁界で動作する干渉計光アイソレータの動作実証),” Technical Report of IEICE, OCS2004-103, Nov. (2004). (in Japanese.)

Domestic Conferences

- [39] Y. Shoji, H. Yokoi, and T. Mizumoto, “Selective oxidation of AlInAs for enhancement of magneto-optic effect in optical isolator (AlInAs選択酸化を用いた低屈折率クラッド層の形成による非相反移相効果の増大),” Extended Abstracts (The 64th Autumn Meeting, 2003); The Japan Society of Applied Physics, 30a-YH-8, Fukuoka, Japan, Aug. 30 (2003). (in Japanese.)
- [40] H. Yokoi, Y. Shoji, E. Shin, and T. Mizumoto, “Optical isolator employing nonreciprocal phase shift operated under unidirectional magnetic field (一方向外部磁界で動作する非相反移相形光アイソレータ),” Proc. of 2004 IEICE General Conference, C-3-107, Tokyo, Mar. (2004). (in Japanese.)
- [41] Y. Shoji, H. Yokoi, and T. Mizumoto, “Mach-Zehnder interferometer for an ultracompact optical isolator with Si waveguides by use of surface activated direct bonding (Si細線導波路を用いた超小型光アイソレータのためのマッハ・ツェンダー干渉計の製作と表面活性化処理接合の検討),” Proc. of 2005 IEICE Society Conference, CS-8-9, Hokkaido, Sept. (2005). (in Japanese.)
- [42] Y. Shoji and T. Mizumoto, “Proposal of polarization independent optical isolator employing TM nonreciprocal phase shift (TMモード非相反移相効果を用いた偏波無依存型光アイソレータの提案),” Extended Abstracts (The 53rd Spring Meeting, 2006); The Japan Society of Applied Physics and Related Societies, 25p-W-1, Tokyo, Mar. (2006). (in Japanese.)

- [43] Y. Shoji and T. Mizumoto, “Wideband operation of Mach-Zehnder interferometric optical isolator using phase adjustment (位相調整によるマッハツェンダー干渉型光アイソレータの広帯域化),” Extended Abstracts (The 67th Autumn Meeting, 2006); The Japan Society of Applied Physics, 29a-ZX-4, Shiga, Aug. (2006). (in Japanese.)
- [44] Y. Shoji and T. Mizumoto, “Demonstration of wideband operation of nonreciprocal phase shift optical isolator (非相反移相型光アイソレータの広帯域化の動作実証),” Proc. of 2006 IEICE Society Conference, C-3-85, Ishikawa, Sept. (2006). (in Japanese.)
- [45] Y. Shoji and T. Mizumoto, “Design of an ultra-wideband optical isolator operating in 1.31–1.55 μ m band (1.31–1.55 μ m帯で動作する超広帯域型光アイソレータの設計),” Extended Abstracts (The 68th Autumn Meeting, 2007); The Japan Society of Applied Physics, 4p-P3-23, Hokkaido, Sept. (2007). (in Japanese.)
- [46] Y. Shoji and T. Mizumoto, “Ultra-wideband design of nonreciprocal phase shift waveguide isolator (非相反移相型光アイソレータの超広帯域設計),” Proc. of 2007 IEICE Society Conference, C-3-70, Tottori, Sept. (2007). (in Japanese.)

Patents

- [47] 水本 哲弥, 庄司 雄哉 “導波路型広帯域光アイソレータ,” 特願 2006-011234 (2006 年 1 月 19 日出願); 国際特許出願番号PCT/JP2006/320521 (2006 年 10 月 10 日出願)
- [48] 水本 哲弥, 庄司 雄哉 “偏波無依存光アイソレータ,” 特願 2006-075854 (2006 年 3 月 20 日出願); 国際特許出願番号PCT/JP2007/056114 (2007 年 3 月 16 日出願)